Design of a medium-range hybrid business jet

a project presented to
The Faculty of the Department of Aerospace Engineering
San José State University

in partial fulfilment of the requirements for the degree
Master of Science in Aerospace Engineering

by

Karpagam Suryanarayanan

May 2021

Dr. Nikos J. Mourtos
Faculty advisor

© 2021
Karpagam Suryanarayanan
ALL RIGHTS RESERVED

ABSTRACT

Design of a medium-range hybrid business jet

Karpagam Suryanarayanan

Air transportation has increased rapidly in the last few decades. This continual growth impacted both the finances and environment in a major way. While aviation fuel prices continuously increase, as a result of increasing demand for air travel and depletion of fossil fuel resources, the environmental impact includes concerns related to air pollution and global warming. These factors have led the aircraft manufacturers to explore alternate forms of aircraft propulsion, especially hybrid and electric propulsion technologies.

The current battery capabilities support general aviation aircraft with minimal payload capacity and a modest range. With rapidly evolving battery technology, it might be possible to design a larger aircraft with increased payload capacity and range in the future. This project explores the possibility of a medium range (7000 km), eleven-seater hybrid-electric business jet. The report presents the conceptual and preliminary design methodology for hybrid aircraft which includes weight and performance sizing, fuselage design, wing and high-lift system design, empennage design, landing gear design, weight and balance, stability and control analysis, drag polar estimation, environmental impact and final specifications. The results indicate that such an aircraft may indeed be feasible in 2030, promising a greener form of air transportation with a take-off weight comparable to conventional business jets.

ACKNOWLEDGEMENTS

I would like to express my sincere gratitude to my family and teachers for supporting me throughout my graduate study. I would like to thank Dr. Mourtos for his patience, enthusiasm, insightful comments, invaluable guidance and encouragement that enabled me to get an in-depth knowledge in the field of aircraft design and successfully complete the project work. I would also like to express my deepest gratitude to my family for encouraging me to pursue my dream of becoming an aerospace engineer and supporting me in all my endeavours. I am greatly indebted to my husband for his endless support and guidance throughout my graduate study.

Table of Contents

NOMENCLATURE

Symbol	Definition	Units (SI)
a	Regression Constant (Empty weight fraction)	-----
a	Regression Constant (Skin friction coefficient)	-----
A	Regression Constant (Empty weight fraction)	-----
A	Regression constant (Fuselage sizing)	-----
AR	Aspect Ratio	-----
b	Regression Constant (Skin friction coefficient)	-----
B	Regression Constant (Empty weight fraction)	-----
b	Span	m
c	Regression Constant (Empty weight fraction)	-----
c	Regression Constant (Business jet - performance sizing)	-----
c	Regression Constant (Fuselage sizing)	-----
C	Constant (Weight sensitivity)	-----
C_f	Flap chord	m
C_r	Root chord	m
C_t	Tip chord	m
C_L	Coefficient of Lift	-----
$c_{L_{max}}$	Maximum coefficient of lift	-----
$\bar{c}$	Mean Aerodynamic Chord	m
C_D	Coefficient of Drag	-----
C_{D_o}	Zero-lift drag	-----
C_j	Specific fuel consumption	lb/hr/lb or hr^{-1}
C_{l_α}	Lift-curve slope	deg^{-1} or rad^{-1}
$C_{l_{\alpha_f}}$	Flapped section lift coefficient	deg^{-1} or rad^{-1}

$C_{L_{\alpha_h}}$	Lift-curve slope (Horizontal tail)	deg^{-1} or rad^{-1}
$C_{L_{\alpha_v}}$	Lift-curve slope (Vertical tail)	deg^{-1} or rad^{-1}
$C_{L_{\alpha_W}}$	Lift-curve slope (Wing)	deg^{-1} or rad^{-1}
$C_{L_{\alpha_W}}$	Lift-curve slope (Wing-fuselage)	deg^{-1} or rad^{-1}
C_{n_β}	Yawing moment coefficient due to sideslip	deg^{-1} or rad^{-1}
$C_{n_{\beta_{wf}}}$	Yawing moment coefficient (Wing-fuselage)	deg^{-1} or rad^{-1}
$C_{n_{\beta_v}}$	Yawing moment coefficient (Vertical tail)	deg^{-1} or rad^{-1}
$C_{n_{\delta_r}}$	Rudder control effectiveness	deg^{-1} or rad^{-1}
$C_{m_{\delta_e}}$	Pitching moment coefficient due to elevator	deg^{-1} or rad^{-1}
d	Regression Constant (Business jet - performance sizing)	-----
D	Weight constant	kg
d_f	Diameter of the fuselage	m
f	Equivalent parasite area	m^2
F	Breguet's partial	kg
e	Oswald efficiency factor	-----
E*	Specific energy density of the battery	Wh/kg
g	Acceleration due to gravity	m/s^2
K	Correction factor	-----
K_{us}	Variable sweep constant	-----
k_{wf}	Wing-fuselage interference factor	-----
k_α	Feedback gain (Longitudinal stability)	-----
k_β	Feedback gain (Directional stability)	-----
k_Λ	Constant (High lift device)	-----
k_n	Wing – fuselage interference factor	-----
k_{RI}	Reynolds number correction factor	-----

K_A	Aspect ratio correction factor	-----
k_λ	Taper ratio correction factor	-----
k_h	Horizontal tail location correction factor	-----
h_f	Height of the fuselage	m
l_c	Cabin length	m
l_f	Length of the fuselage	m
l_{fc}	Length of the fuselage-cone	m
l_m	Distance between CG and main gear	m
L_N	Fuselage nose length	m
l_n	Distance between CG and Nose gear	m
L/D	Lift-to-drag ratio	-----
M	Mach number	-----
N	Number of engines	-----
$N_{t_{crit}}$	Engine-out yawing moment	kg m
N_D	Drag induced yawing moment	kg m
n_s	Number of struts	-----
P_n	Static load on nose wheel	kg
P_m	Static load on main wheel	kg
q, q′	Dynamic pressure	N/m^2
$\bar{q}$	Cruise dynamic pressure	N/m^2
$\overline{q_{mc}}$	Dynamic pressure at minimum control speed	N/m^2
R	Range	km
RC	Rate of climb	m/min
S	Surface area	m^2
S_{FL}	Landing field length	m

S_{TOFL}	Take-off field length	m
S_{wet}	Wetted surface area	m^2
T	Thrust	N
T_{To_e}	Thrust from single engine	N
T/W	Thrust-to-weight ratio	-----
t/c	Thickness to chord ratio	-----
V	Cruise Speed	m/s
V_A	Approach speed	m/s
V*	Volume specific energy	Wh/L
V_{lof}	Lift-off speed	m/s
$\bar{v}$	Tail volume coefficient	-----
V_s	Stall speed	m/s
W	Weight (Weight-sizing)	kg
$W_{battery}$	Battery weight	kg
W_c	Crew weight	kg
W_{ef}	external width	m
W_E	Empty weight	kg
W_F	Fuel weight	kg
W_{if}	Internal width	m
W_{OE}	Operating Empty weight	kg
W_{PL}	Payload weight	kg
W_{tfo}	Trapped fuel and oil weight	kg
W_{TO}	Take-off Weight	kg
W/S	Wing loading	Kg/m^2
$\bar{x}$	Location of Mean aerodynamic chord (X axis)	m

X_{CG}	CG location along longitudinal axis	m
X_h	Horizontal tail arm	m
X_v	Vertical tail arm	m
$\bar{X}_{ac}$	Aerodynamic center (fraction of MAC)	-----
$\bar{X}_{cg}$	Center of gravity (fraction of MAC)	-----
$\Delta\bar{X}ac_f$	Shift in Aerodynamic center (Fraction of MAC)	-----
$\bar{y}$	Location of Mean aerodynamic chord (Y axis)	m
Y_t	Engine location (From the fuselage centerline)	m
Z_{CG}	CG location along directional axis	m
Subscripts		
$()_A$	Aircraft (Stability and control analysis)	-----
$()_{airfoil}$	Airfoil	-----
$()_{battery}$	Battery	-----
$()_C$	Crew (Wight sizing) / Cabin (fuselage design)	-----
$()_{Cruise}$, $()_{cr}$	Cruise	-----
$()_{fuel}$, $()_F$	Fuel	-----
$()_f$	Fuselage (Fuselage design)/ Flap (Wing design)	-----
$()_{fc}$	Tail cone	-----
$()_{FL}$	Field Length	-----
$()_E$	Empty	-----
$()_h$	Horizontal tail	-----
$()_L$	Land	-----
$()_{lof}$	Lift-off	-----
$()_{PL}$	Payload	-----
$()_{max}$	Maximum	-----

$()_n$	Nose	-----
$( )_{reqd}$	Required	-----
$()_{root}$	Airfoil (root section)	-----
$( )_s$	Stall	-----
$( )_{Sea-level}$	Sea level	-----
$()_t$	Tail (Fuselage design)/ Twist (Wing design)	-----
$()_{total}$	Total	-----
$()_{tfo}$	Trapped fuel and oil	-----
$()_{tip}$	Airfoil (Tip section)	-----
$()_{TO}$	Take-off	-----
$()_v$	Vertical tail	-----
$( )_{wet}$	Wetted surface	-----
$()_{wf}$	Flap surface (Wind design)	-----
$()_{wf}$	Wing-fuselage (Stability and control analysis)	-----
$()_W$	Wing	-----
$( )_0$	Engine start and warm up	-----
$( )_1$	Taxi	-----
$( )_2$	Take-off , Climb	-----
$( )_3$	Cruise - start	-----
$( )_4$	Cruise - end , Loiter - Start	-----
$( )_5$	Loiter - end , Descent - start	-----
$( )_6$	Land	-----
$( )_7$	Taxi	-----
$( )_8$	Shutdown	-----
$()_{1/4}$	Quarter chord (Sweep)	-----

Acronyms		
AC	Aerodynamic center	-----
AEO	All Engine operative	-----
CG	Centre of gravity	-----
CGR	Climb Gradient	-----
FAR	Federal Aviation Regulation	-----
F.S	Fuselage station	-----
OEI	One Engine Inoperative	-----
mff	Mission fuel fraction	-----
MRHBJT	Medium-range Hybrid Business Jet	-----
SFC	Specific Fuel Consumption	lb/hr/lb or hr^{-1}
SUGAR	Subsonic Ultra Green Aircraft	-----
TOFL	Take-off Field Length	-----
TOP	Take-off parameter	
USD	U.S. Dollar	-----
Greek symbol		
ε	Upwash angle	deg. or rad
$\bar{\varepsilon}$	Upwash and downwash angle	
η	Efficiency	-----
η_v	Vertical tail Efficiency	-----
η_h	Horizontal tail efficiency	-----
ρ	Density	-----
σ	Density ratio	-----
Δ	Incremental	-----
λ	Taper ratio (Wing and tail)	-----

λ_f	Fineness ratio (Fuselage)	-----
θ_{fc}	Tail-cone angle	deg.
θ_{lof}	Lift-off angle	deg.
α	Angle of attack	deg.
α_i	Incidence angle	deg.
α_t	Twist angle	deg.
Λ	Sweep angle	deg.
$\lceil$	Dihedral angle	deg.
$\alpha_{\dot{\delta}_f}$	Flap effectiveness	-----
δ	Deflection	deg.
Ψ	Lateral tip-over angle	deg.
τ	Flap effectiveness parameter	-----
δ_r	Rudder deflection	deg.
Chemical formula		
CO_2	Carbon dioxide	-----
Li	Lithium	-----
O	Oxygen	-----
S	Sulphur	-----
Zn	Zinc	-----

LIST OF FIGURES

LIST OF TABLES

1. Mission specification and comparative study

1.1 Introduction

Air travel has immensely increased over the past few decades. As a result, there is an increasing usage of fuel, which is aggravating the carbon dioxide (CO_2) emission rate and the depletion of the Ozone layer. The historical trend of the carbon-dioxide emission in Figure 1.1 shows a dramatic increase in CO_2 emissions over the last few decades. The data shows a 17% increase from 2010 to 2019 (Global Carbon-dioxide emissions, 2020). The international aviation sector contributes about 2% of the global CO_2 emissions (Knapp & Said, 2018). Furthermore, due to the increasing demand, fuel prices have climbed rapidly. The financial and environmental considerations stimulate the aircraft manufacturers to explore alternate forms of propulsion with high energy efficiency, low cost, and greener air transport. The demand for a means of green air transport to diminish the increasing carbon footprint has placed great emphasis on the development of an electric/ battery-powered aircraft.

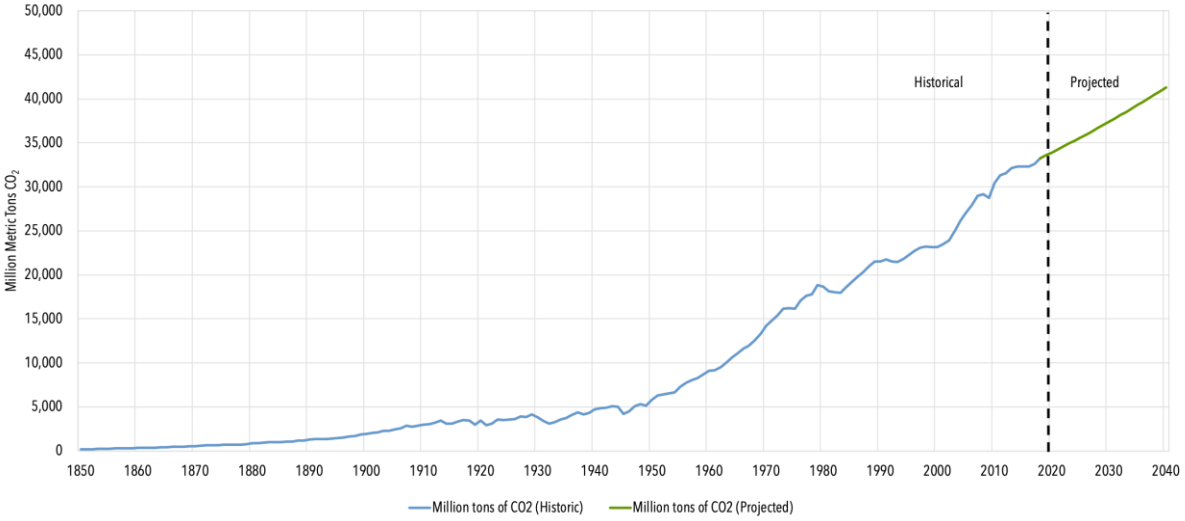

Figure 1.1 Carbon-dioxide emission trend (Global Carbon-dioxide emissions, 2020)

The main advantages of the hybrid or electric propulsion over conventional fuel propulsion are the reduced fuel burn and emission of pollutants. The key challenges associated with this are the battery technology, aircraft weight, structural and aerodynamic considerations.

The specific energy density of the hydrocarbon fuel is very much higher compared to the existing batteries. The low specific energy density of the batteries demands more volume for storage, thereby increasing the take-off weight of the aircraft. While the battery technology is evolving, the current state-of-the-art is only sufficient to power small general aviation aircraft with a minimal payload capacity and a moderate range. For a long or medium-range, a hybrid propulsion system is necessary. This project aims to explore the possibility of designing a medium-range hybrid business jet with fuel-battery propulsion.

1.2 Literature review

1.2.1 Battery technology

In ground transportation, hybrid and electric vehicles are predominant as the current battery capabilities are delivering performance comparable to that of the conventional fuel models (Hepperle, 2012). Similarly, there are many electric light-weight aircraft for short-range available in the market. On the other hand, a completely electric model for a medium or long-range and on a large scale with the present-day battery technology is still in the developing stage, as the main challenges are the energy requirement, battery mass and the specific energy density. The energy required for propulsion is stored onboard.

The energy per mass E* (specific energy density) determines the net amount of battery and the weight required for propulsion. The energy per mass of the battery is lesser than the aviation fuel and kerosene, as shown in Figure 1.2 (Hepperle, 2012). The higher the specific energy density, the lower will be the overall weight of the system. Further, the energy per volume is also critical, as the space available in aircraft limits the net internal volume for battery storage. If the energy per mass is too small, the aircraft would require large wings, and fuselage to accommodate the extra weight from the batteries, which complicates the structural and aerodynamic design of the vehicle. Furthermore, the drag due to the increased surface area of exposure would influence the overall efficiency of the aircraft. Also, the batteries require

casings with temperature control system (Hepperle, 2012) to regulate the temperature in the battery to avoid over-heating of the system. The battery offers an efficiency of 70% comparing to the 40% efficiency of the classical combustion system (Hepperle, 2012). The main concern with the battery system is its mass, which is higher than the conventional fuel system due to its specific energy density.

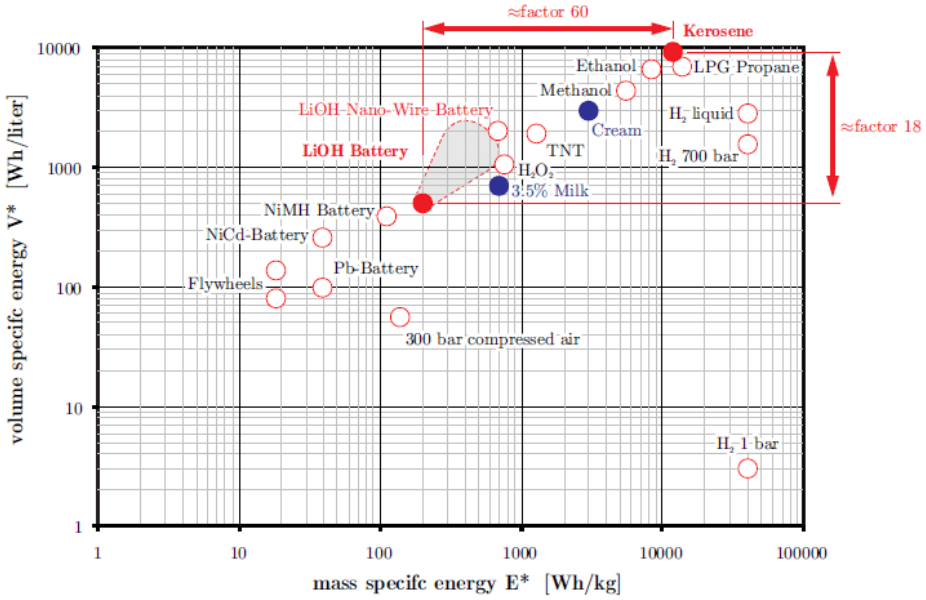

Figure 1.2 Mass specific energy and volume specific energy of different storage systems (Hepperle, 2012)

Lithium-ion batteries are used to a great extent in electric-powered aircraft, as they are very efficient. The main disadvantage is its low specific energy density, which requires high volume for storage. The in-development lithium-based batteries such as Lithium-Sulphur (Li-S) and Lithium-Oxygen (Li-O_2) are the areas of high interest as they are anticipated to provide high specific energy densities of 1750 Wh/kg, as shown in figure 1.3. The Li-O_2 batteries with the highest energy storage capacity are ideal for the medium-range application, as the net battery weight is reduced, thereby reducing the overall weight of the vehicle. The main disadvantages of the Li-O_2 battery are the stability of the cell components and the discharge rate.

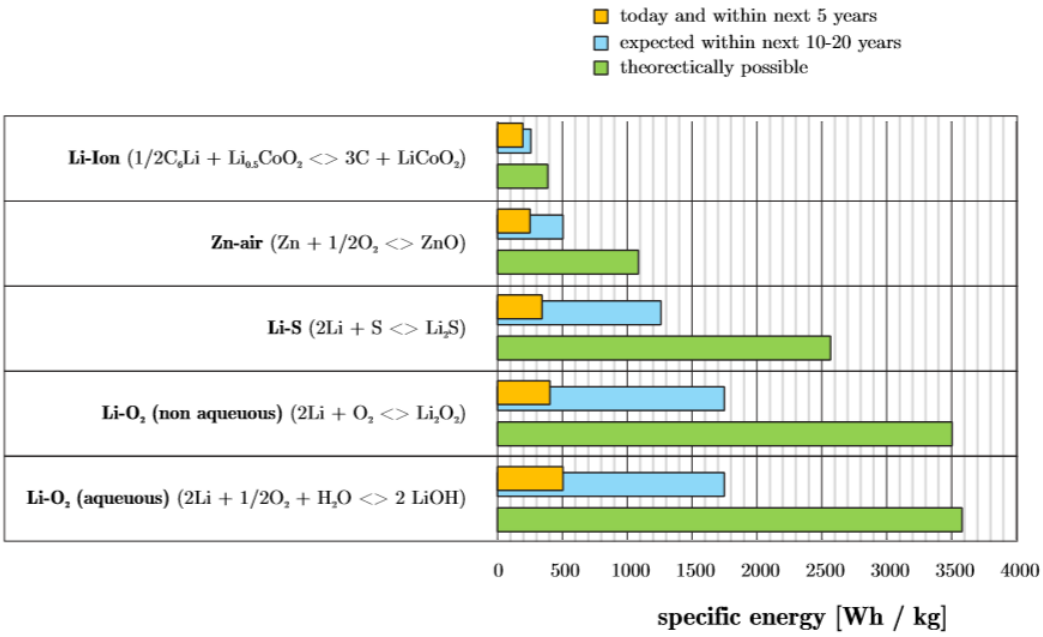

Figure 1.3 Current and future battery technology (Hepperle, 2012)

1.2.2 Propulsion system

The propulsion design is coupled with the battery technology. The most widely used propulsion system for commercial transport is the gas-turbine engine. The propulsion system design for a hybrid/electric aircraft is classified into the parallel-hybrid electric propulsion system, series-hybrid system, series-parallel partial hybrid system, all-electric propulsion system, turbo-electric and partially turbo-electric system (Bowman, Marien, & Felder, 2018). In parallel-hybrid architectures, a battery-powered motor and a fuel-powered turbine are mounted on the same turbofan shaft, which allows the fan to be driven by two energy resources independently. In a series hybrid propulsion system, the power in the gas turbine shaft is converted to the electric power, which is distributed to drive motor and charge batteries. The series-parallel partial hybrid system has features from series and parallel hybrid system. The turbo-electric system uses the electricity on-board generated by the fuel-powered turbine (Bowman, Marien, & Felder, 2018).

The electric motors provide continuous power operation in the cruise condition. The current electric motor technology has the capacity to deliver power like that of a turboshaft and

turbofan engines at the cruise power (Hepperle, 2012), but the specific power of the electric motors are 2- 4 KW/kg which is very much lesser than the conventional turbofan engine's specific power of 10 KW/kg in the cruise condition. The electric aircraft tend to weigh heavier than fuel-powered aircraft, which demands a strong need for high specific power, light-weight electric motors, so that overall efficiency of the aircraft could be improved.

1.2.3 Subsonic Ultra Green Aircraft Research

In the year 2008, Boeing commenced research and exploration of Subsonic Ultra Green Aircraft (SUGAR). Four models of SUGAR were studied: Refined SUGAR, which is a conventional configuration with 2030-2035 technology; SUGAR high which is high span strut-braced wing configuration; SUGAR Volt, an electric aircraft with different architectures (battery only, fuel-cell, and battery electric gas turbine hybrid); and SUGAR Ray, a hybrid wing body configuration with similar technology in SUGAR high (Bradley, 2011). SUGAR Volt is a hybrid-electric aircraft designed for 154 passenger capacity with a high aspect ratio of 19.5 with a long, truss braced wing, powered by two hybrid hfan turbofan engines. The battery pods for the SUGAR Volt are wing mounted. The hfan engine has a parallel-hybrid propulsion system that facilitates all-electric, all-fuel, and combined modes of operation depending on the mission requirements. The h-fan features a conventional fan and nacelle arrangement for the lowest possible noise (Bradley, 2011). The wind tunnel testing of the SUGAR Volt indicated that the model was able to reach a Mach of 0.8 (Bradley, 2015). The aerodynamic and structural considerations are the main challenges involved in designing a high aspect ratio model and the SUGAR Volt technology is expected to reach the market in the 2030-2035 timeframe.

1.2.4 Zunum Aero – Hybrid aircraft for regional travel

Zunum Aero has developed a hybrid architecture with a low maintenance powertrain to transform regional travel. The aircraft expects to provide an operating cost of 40 – 80% lower than those of current regional aircraft (Knapp & Said, 2018). The aircraft features wing-integrated battery packs, and has a quick climb rate of 487 m/min and top cruise speed of 152 m/s. The propulsor has quiet fans with integrated fault-tolerant electric motors and controllers. The aircraft can cover a range of 1126 km (700 miles) and the aircraft weighs 5200 kg. It has a payload capacity of 1133 kg and the usable amount of fuel is 362 kg. It is designed for 12 passengers in the economy class or 9 passengers in the premium class. Their wings are structurally optimized to leverage free stream for cooling, and they are low in cost and weight (Zunum Aero's Hybrid Electric Aircraft n.d.). The configuration layout of the aircraft is shown in Figure 1.4.

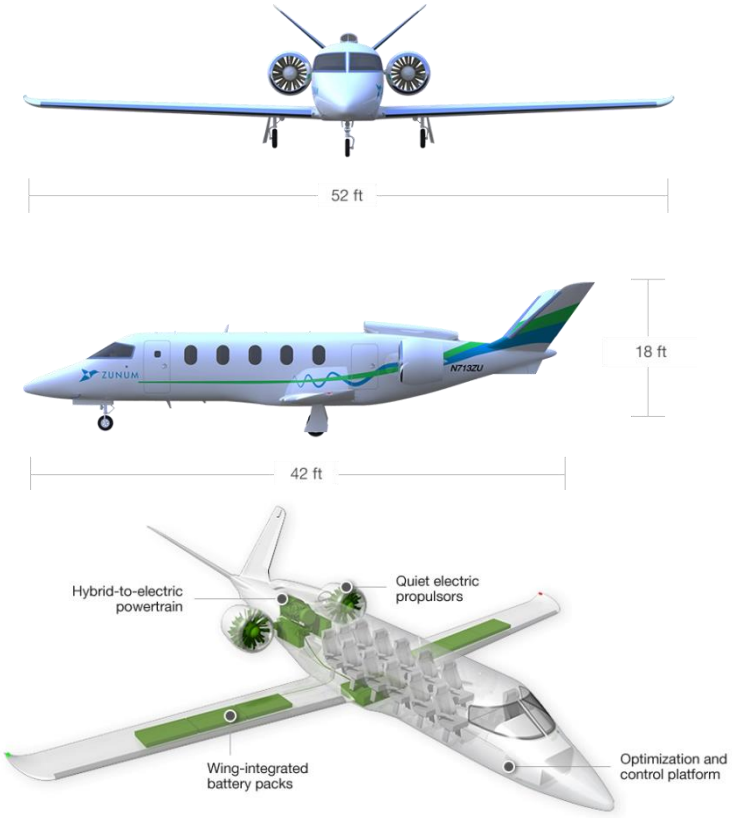

Figure 1.4 Zunum Aero's regional hybrid aircraft (Zunum Aero's Hybrid Electric Aircraft n.d.)

1.3 Mission specification

The hybrid electric jet is powered by JET A-1 fuel in the fuel powered segment and Lithium-Oxygen battery ($Li\text{-}O_2$) which would have a specific energy density of 1750 Wh/kg in the battery powered segment. The following comprise the mission requirement for the hybrid electric medium range business jet:

- Payload: 11 passengers at 79.5 kg each and 17 kg of baggage each
- Number of crew members: 2 pilots, 1 cabin attendant
- Total range (R): 7000 km
- Range (Fuel powered) (R_{fuel}): 3500 km
- Range (Battery powered) ($R_{battery}$): 3500 km
- Cruise speed (V): 222 m/s
- Cruise Mach number (M) = 0.75
- Cruise altitude: 12192 m
- Take-off field length: 1828 m at 1524 m (5000 ft altitude)
- Landing field length: 1600 m at 1524 m (5000 ft altitude)
- Noise requirement: $\leq$ 89 EPNdB

The mission of the hybrid-electric business jet depends on fuel for take-off, climb, loiter, descent, and land segments. The mission profile for the medium-range hybrid business jet is shown in the figure below:

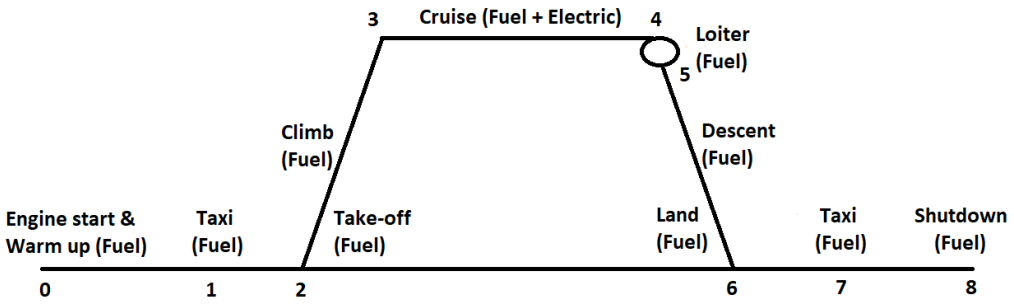

Figure 1.5 Mission profile for the medium-range hybrid business jet

1.4 Methodology

The hybrid-electric aircraft will be designed with a different method that accounts for performance from both the fuel and the battery powered segments so that the aircraft can function optimally in any mode of operation. The design methodology for the hybrid aircraft differs from the conventional (fuel-based) design approach by the fact that the battery sizing, performance, and the battery's influence on the overall take-off weight are considered while designing the aircraft. In addition to this, the propulsion system will be chosen such that it can operate on both the fuel and electrical energy independently. The weight and range sensitivities will be used for parametric optimization of the aircraft so as to meet the necessary mission requirements. The choice of parameters will affect the design of primary components such as the wing, fuselage, empennage, and landing gear. The high-lift device for the take-off and the landing will be designed using the required lift increment computed from the performance sizing of the aircraft. The locations for storing the batteries and the fuel will be analysed. If the volume in the wing and fuselage is not sufficient for storing, the aircraft will be resized to allow sufficient space for storing the batteries and fuel. Furthermore, the weight and balance analysis, stability, and control of the aircraft, drag polar analysis and the cost analysis will be performed. The horizontal and vertical stabilizers will be designed to meet the necessary stability requirement. Also, the lift-to-drag (L/D) ratio from the drag polar analysis will be computed. If the L/D ratio obtained does not match with the initially assumed L/D for weight and performance sizing, the primary components will be resized. The preliminary sizing of the aircraft will be carried out combining the methodology from Airplane design by Roskam (Roskam, 2018) and Electric Flight - Potential and Limitations by Hepperle (Hepperle,2012).

1.5 Market Analysis

Between 2010 to 2019, a consistent upsurge has been observed in the electrification of the aircraft system (Market Forecast, 2020). Aerospace industries are currently working towards the electrification and hybridization of the aircraft system to combat the climate change and the greenhouse gas emission reduction. The aircraft electrification market is estimated to be 3.4 billion USD in 2022 and projected to reach 8.6 billion USD by 2030 with a compound annual growth rate of 12.2% (Aircraft Electrification market, 2020). The expected growth rate of the electrification shows a very high demand for the hybrid/electric jets. The market trends, advancement in the propulsion system and the evolving battery technology show a promising future for the medium-range hybrid business jets in the coming years.

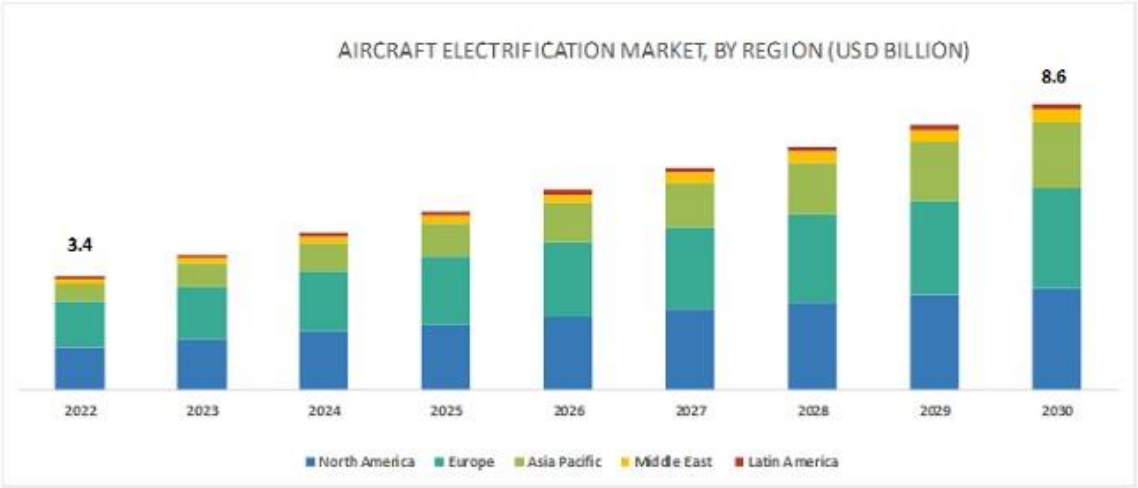

Figure 1.6 Aircraft Electrification market by region (Aircraft Electrification market, 2020)

1.6 Comparative study of airplanes with similar mission performance

A comparative study of aircraft gives a baseline for designing the hybrid business jet. The characteristics of a hybrid business jet will be different from the conventional jets but, the hybrid aircraft for a medium and long range are currently in the development stage, and so the conventional aircraft that uses fuel for propulsion are considered for the comparative study.

Table 1.1 Comparative study of business jet with similar range and payload capacity

S. No	1	2	3	4
Aircraft manufacturer	Dassault aviation			Bombardier
Model of the aircraft	Falcon 900 LX	Falcon 2000 S	Falcon 2000 LXS	Challenger 650
Crew	2	2	2	2
Capacity	12	10	10	10
Length (m)	20.21	20.23	20.23	20.9
Height (m)	7.55	7.06	7.06	6.3
Wingspan (m)	21.38	21.38	21.38	19.6
Cabin volume (cu.m)	35.80	29.00	29.00	-
Wing Area (m^2)	49	-	-	45.4
Max. zero fuel weight (kg)	14000	13472	13472	14515
Max. fuel (kg)	9482	6622	7557	9072
Max. landing weight (kg)	20185	17827	17827	17327
Max. take-off weight (kg)	22225	18598	19414	21863
Cabin height(m)	1.88	1.88	1.88	1.83
Cabin width(m)	2.34	2.34	2.34	2.41
Cabin length(m)	10.11	7.98	7.98	7.8
Engine manufacturer	Honeywell	Pratt &Whitney	Pratt &Whitney	General Electric
No. of engines	3	2	2	2
Model	TFE731-60	PW308C	PW308C	BR710A2
Thrust (kN)	22.24	31.14	31.14	41.01
Max speed (Mach)	0.84	0.862	0.862	0.85
Range (km)	8800	6205	7410	7408
Take-off distance (m)	-	1318	1425	1720
Landing distance(m)	736	706	689	846
Approach speed (knots)	111	107	105	-
Max. operating speed (kph)	685	685	685	-
Max. operating altitude (m)	15545	14325	14325	12497
Take-off W/S (kg/m^2)	453.57	-	-	481.56

The payload capacity, range, cruise altitude for the hybrid aircraft are similar to the ones tabulated in Table 1.1 (Falcon -900 LX, Falcon- 2000S, Falcon – 2000LXS, and Bombardier challenger 650 specifications, n.d.). The primary difference is that the hybrid aircraft uses fuel and electricity for propulsion in the cruise segment. The characteristics of aircraft tabulated above, have similar configuration with subtle difference in terms of its performance aspect and the engine classification. The Falcon 900 LX is a tri-jet aircraft, while the other aircraft are bi-jets. The aircraft considered for the comparative study uses fuel for propulsion. The aircraft presented above feature a low wing, single-aisle cabin, retractable landing gears, and operate at a high Mach number of 0.8 and above. Furthermore, they are designed for a medium-high range operation.

1.7 Conclusion

While there are a plethora of challenges laying ahead in designing a hybrid business jet for a range of 7500 km, there are a few factors such as the evolving battery technology and the promising market for aircraft electrification that provide a strong motivation to overcome the hurdles. A preliminary approach to design the hybrid aircraft to meet the critical mission requirements in terms of range and payload capacity are presented in the upcoming chapters.

2. Weight sizing and Weight sensitivities

2.1 Introduction

Weight sizing is the most important aspect of aircraft design which provides the weight that the aircraft must be designed to, so that it can perform the intended mission. In the class I weight sizing, the initial estimate of the weight fractions are computed using empirical relations. The design take-off weight at the beginning of the mission comprises six components:

- Crew weight (W_C)
- Payload weight (W_{PL})
- Fuel weight (W_F)
- Trapped fuel and oil weight (W_{tfo})
- Battery weight ($W_{battery}$)
- Operating Empty weight (W_{OE})

In addition to the estimation of mission weight, the weight and range sensitivities are presented in this chapter.

2.2 Mission Weight estimation

The take-off weight for a conventional fuel-powered aircraft is the summation of the operating empty weight, fuel weight, and the payload weight (Roskam, *Airplane Design: Part I*, 2018). In the case of a hybrid aircraft, the take-off weight of the aircraft also accounts for the battery weight:

$$W_{TO} = W_{PL} + W_F + W_{battery} + W_{OE} \tag{2.1}$$

where:

$$W_{OE} = W_C + W_{tfo} + W_E \tag{2.2}$$

The empty weight W_E consists of the manufacturer's empty weight and the fixed equipment weight (Roskam, *Airplane Design: Part I*, 2018).

2.2.1 Payload and crew weight

The payload for the hybrid business consists of the passengers and the baggage. The aircraft is designed for 11 passengers. The crew consists of two cockpit crew and one cabin crew. The allowable baggage weight of 17 kg per person and the weight per passenger of 79.5 kg are assumed based on the data available in (Roskam, *Airplane Design: Part I*, 2018). The total weight of the payload and crew is 1351 kg.

2.2.2 Empty weight fraction

The empty weight consists of the structural weight, engine weight, nacelle weight, fixed equipment weight, and other miscellaneous weights. The allowable value of empty weight for the assumed take-off weight is found using the following equation (Roskam, *Airplane Design: Part I*, 2018):

$$W_E = inv.log_{10}\{(log_{10}W_{TO} - A)/B\} \tag{2.3}$$

The regression constants A and B has been determined by converting the following exponential equation from the reference (Raymer, 2012) to the logarithmic form:

$$\frac{W_E}{W_{TO}} = a\, {W_{TO}}^{C} Kus \tag{2.4}$$

The constants a and c are dependent on the type of the aircraft and K_{us} changes based on the wing sweep. For the jet transport aircraft, the constants a = 1.02, c = -0.06; variable sweep constant K_{us} = 1.00 for a fixed sweep wing (Raymer, 2012). Furthermore, the empty weight fraction is multiplied by a factor 0.95 to account for the decrease in empty weight by replacing aluminium material with advanced composite material. The conversion of the exponential equation to the logarithmic form and the calculation of regression constants A and B are described in Appendix A. The values of the regression constants: A = 0.0145 and B = 1.0638.

2.2.3 Battery weight fraction

The aircraft is designed to be powered by fuel for 3500 km (50% of the total range of the aircraft) and by the battery for the remaining 50%. The battery weight fraction with respect to the take-off weight is predicted using the relation (Hepperle, 2012):

$$R_{Battery} = E^{*}\eta_{total}\frac{1}{g}\frac{L}{D}\frac{W_{battery}}{W_{TO}} \quad (2.5)$$

The above equation indicates a high dependency on the specific energy density of the battery, total efficiency (η_{total}), and the lift-to-drag ratio. The mass of the aircraft does not change during the battery powered segment unlike the fuel powered segment, where the total mass of the aircraft decreases when the fuel is burnt. The overall efficiency of the battery powered system is more than 70% which much higher than the combustion system's efficiency close to 40% (Hepperle, 2012). The battery system and battery technology are evolving, which is expected to outweigh the disadvantages in terms of weight. The literature review on the battery technology shows that the specific energy density E* of the lithium-oxygen battery is expected to reach 1750 Wh/kg in the next 10-15 years. Furthermore, the lift to drag ratio plays a vital role in battery design. The battery weight ratio shows an inverse proportionality with respect to the L/D. A high lift-to-drag ratio is preferred for reducing the battery weight. The current $(L/D)_{max}$ range is 17 -20 for the commercial subsonic jet (Filippone,2000). The primary factors associated with designing aircraft with high lift to drag ratio are the structural and aerodynamic considerations as a high L/D ratio demand a long wing. The medium-range hybrid business jet is designed with futuristic technology. The field of structures, material, and battery technology are advancing and so it is reasonable to choose the lithium oxygen battery with E* = 1750 Wh/kg, an $(L/D)_{max}$ of 22 and a total efficiency of 90% for the medium-range hybrid business jet. The battery weight ratio is calculated as follows:

R = 3500 km = 3500000 m; g = 9.81 m/s^2 ; $(L/D)_{max}$ = 22 ; η_{total} = 90 %

E^{*} = 1750 Wh/kg = (1750*3600) m^2/s^2

Substituting the values given above,

Battery weight ratio $\frac{W_{battery}}{W_{TO}} = (350000 * 9.81)/(1750 * 3600 * 22 * 0.9)$ = 0.2753

2.2.4 Fuel weight fraction

The segments such as the warm-up, taxi, take-off, climb, descent, and landing depend on the fuel for propulsion. Furthermore, the mission require an additional loiter time of 45 minutes, which also depends on fuel. The amount of fuel required for a mission depends on the mission requirement, the aerodynamics of the aircraft, and the fuel consumption (Raymer, 2012). The fuel weight is computed using fuel-fraction method, in which the fuel fraction for each segment i.e., the begin weight and the end weight at each phase, specified in the mission profile is calculated. The fuel fraction is computed using the following expressions:

$$\frac{W_F}{W_{TO}} = (1 - mff) \tag{2.6}$$

$$mff = \left(\frac{W1}{W0}\right)\left(\frac{W2}{W1}\right)\left(\frac{W3}{W2}\right)\left(\frac{W4}{W3}\right)\left(\frac{W5}{W4}\right)\left(\frac{W6}{W5}\right)\left(\frac{W7}{W6}\right)\left(\frac{W8}{W7}\right) \tag{2.7}$$

The fuel fraction for all the segments except the loiter and cruise is obtained from the fuel fraction data for each segment for the business jet category (Roskam, *Airplane Design: Part I*, 2018). The fuel fraction value for different segments is shown in the table below:

Table 2.1 Mission fuel fraction (Roskam, *Airplane Design: Part I*, 2018)

Segment	**Fuel fraction**
Engine start and warmup (W_1/W_0)	0.99
Taxi (W_2/W_1)	0.99
Take-off (W_3/W_2)	0.995
Climb (W_4/W_3)	0.98
Descent (W_7/W_6)	0.99
Land, Taxi, and shutdown (W_8/W_7)	0.992

The cruise segment mission fraction is determined using Breguet's range equation (Roskam, *Airplane Design: Part I*, 2018):

$$R_{fuel} = \frac{V}{C_{j_{cruise}}} \left(\frac{L}{D}\right)_{cruise} ln\left(\frac{W_5}{W_4}\right) \quad (2.8)$$

The range is dependent on the specific fuel consumption (C_j) and the lift-to-drag ratio (L/D). The aircraft can travel farther than the expected range, depending on the performance of the engine. The lift-to-drag ratio for the cruise segment is 86.6% maximum lift-to-drag ratio (Raymer,2012). Similarly, the weight fraction for the loiter segment is estimated using Breguet's endurance equation for a loiter time of 45 minutes (Roskam, *Airplane Design: Part I*, 2018):

$$E = \frac{1}{C_{j_{loiter}}} \left(\frac{L}{D}\right)_{max} ln\left(\frac{W_6}{W_5}\right) \quad (2.9)$$

The fuel fraction for the cruise and loiter segments depends on the performance of the engine. The parameter C_j is the specific fuel consumption, provides the performance engine. It varies with altitude. An engine with low SFC is the most preferred for any mission. In the preliminary stage of design, the specific consumption is chosen based on the reference data (Raymer,2012) as 0.5 and 0.4 for the cruise and loiter segments, respectively. The fuel fraction for the cruise and loiter segments are as follows:

- Cruise segment

  $R_{fuel} = 3500\ km$; V = 222 m/s ; $C_{j_{cruise}}$ = 0.5 hr^{-1}

  $\left(\frac{L}{D}\right)_{cruise} = 0.866\ (22) = 19.05$

  $\left(\frac{W_5}{W_4}\right) = exp\ (-((3500 * 1000 * 0.5)\ /3600)\ /\ (222 * 22 * 0.866))$

  Fuel fraction for cruise segment $\left(\frac{W_5}{W_4}\right) = 0.8914$

- Loiter segment

  $E = 45\ min$; $C_{j_{loiter}}$ = 0.4 hr^{-1}

$$\left(\frac{L}{D}\right)_{max} = 22$$

$$\left(\frac{W_6}{W_5}\right) = exp\,(-(45^* 0.4) / (22 * 60))$$

Fuel fraction for the loiter segment $\left(\frac{W_6}{W_5}\right) = 0.9865$

The mission fuel fraction is computed by substituting the fuel fraction values for each segment in the equation 2.7:

$mff = (0.990)(0.99)(0.995)(0.98)(0.8914)(0.9865)(0.99)(0.992) = 0.8253$

The fuel weight fraction is obtained using the equation 2.6 for a mission fuel fraction of 0.8253:

Fuel weight fraction $\frac{W_F}{W_{TO}} = (1 - 0.8253) = 0.1787$

2.2.5 Calculation of take-off weight

The component weight and weight fractions obtained from section 2.2.1 through section 2.2.4 are used to estimate the take-off weight. The flowchart of the weight sizing is presented in the figure below.

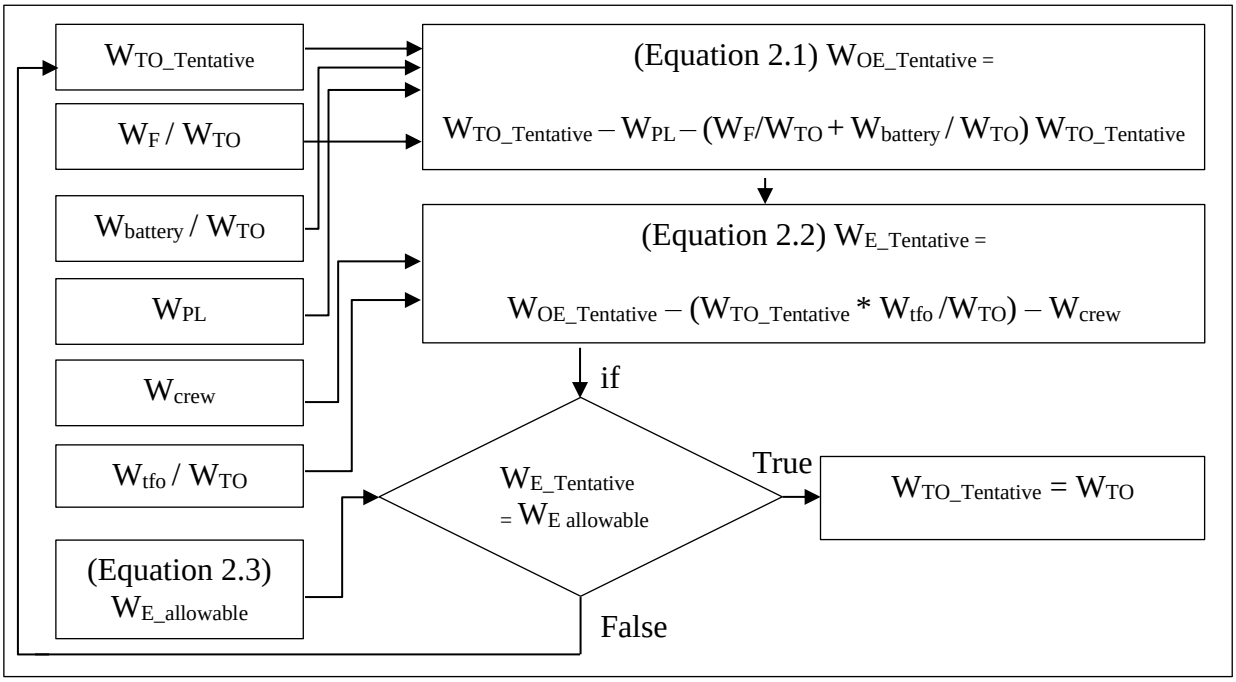

Figure 2.1 Weight Sizing procedure

In the weight sizing process, iterations are performed until the tentative value and the allowable weight are equal. The summary of the preliminary weight sizing parameters is tabulated below:

Table 2.2 Class I preliminary sizing mission weight

Weight component	Weight	Weight fraction
Payload weight	1061.5 kg	0.036
Crew weight	289.5 kg	0.0099
Battery weight	8013 kg	0.275
Empty weight	14520 kg	0.498
Fuel weight	5084 kg	0.17
Trapped fuel and oil weight	145 kg	0.005
Total take-off weight	29112 kg	

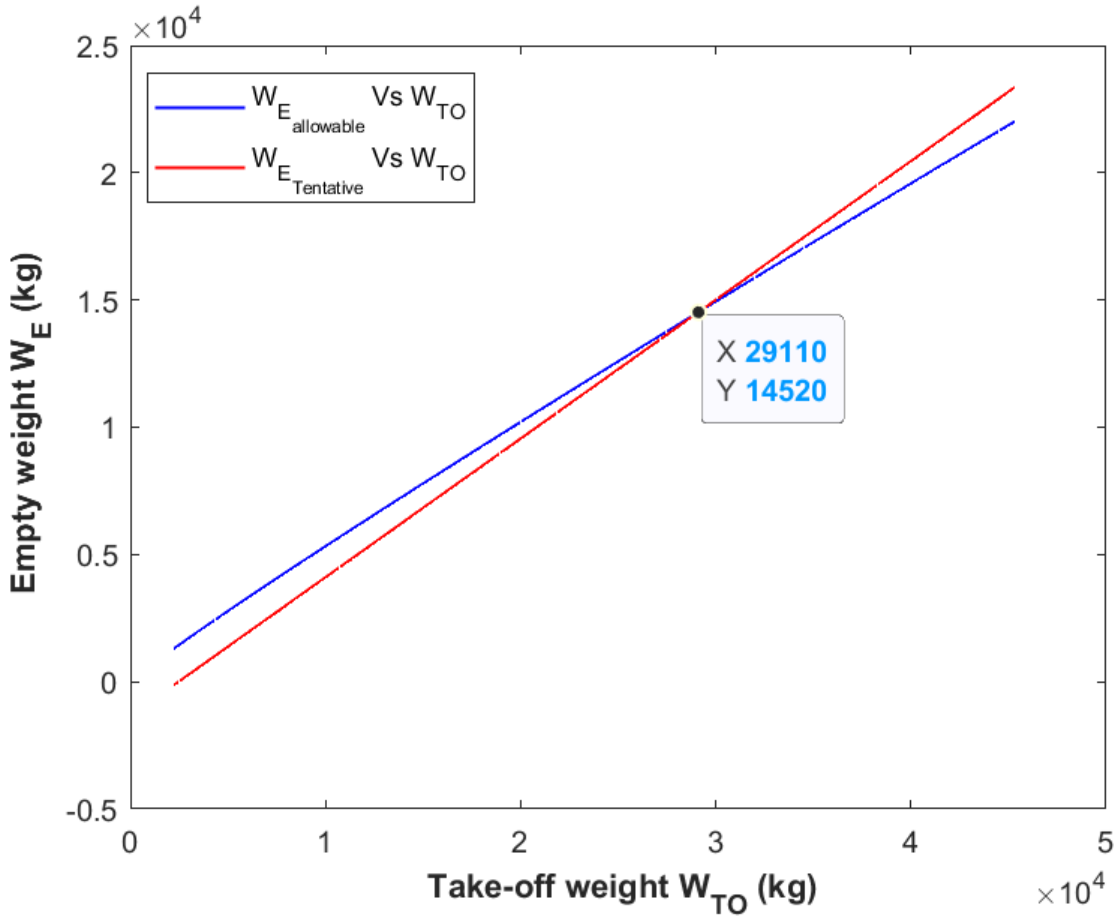

Figure 2.2 Weight sizing design point

2.3 Weight and Range sensitivities

In the preliminary sizing, it is required to estimate the parameters that drive the design and so the sensitivity of the certain parameters assumed for weight estimation is conducted. The critical design requirements for the medium-range hybrid business jet are the take-off weight and range. The sensitivity on these requirements are conducted to predict the design parameters resulting in the moderate take-off weight and achieve the desired range.

2.3.1 Take-off weight sensitivities

The sensitivity of the aircraft take-off weight with respect to the empty weight, range, endurance, lift-to-drag ratio, cruise speed, cruise altitude, payload, mass of the battery and specific fuel consumption are evaluated in this section. The sensitivity equations for the hybrid aircraft accounts for the contribution from the battery weight to the total weight. Therefore, the following equations for determining the weight sensitivities are adapted from Roskam 's equation for weight sensitivities (Roskam, *Airplane Design: Part I*, 2018):

$$W_E = W_{PL} - W_C - W_F - W_{tfo} - W_{battery} - W_{TO} \tag{2.10}$$

$$W_E = CW_{TO} - D \tag{2.11}$$

$$C = 1 - (1 - Mff) - \left(W_{tfo}/W_{TO}\right) \tag{2.12}$$

$$D = W_{PL} + W_C + W_{battery} \tag{2.13}$$

The value of C is 0.8203 and D is 9364 kg. The take-off weight equation for estimating the sensitivity is obtained by replacing the empty weight in equation 2.3 with the equation 2.11, which is expressed as (Roskam, *Airplane Design: Part I*, 2018):

$$log_{10}W_{TO} = A + B\, log_{10}(W_{TO} - D) \tag{2.14}$$

The airplane growth factor due to the empty weight is estimated by differentiating the equation 2.14 with respect to the take-off weight, which is written as:

$$\frac{\partial W_{TO}}{\partial W_E} = BW_{TO}\left[invlog\left(\frac{logW_{TO} - A}{B}\right)^{-1}\right] \tag{2.15}$$

The following sensitivity equations are obtained from Roskam (Roskam, *Airplane Design: Part I*, 2018). The sensitivity of the take-off weight to the payload weight is estimated as 2.84 using the equation below. It means that for take-off weight should be increased by 2.84 kg for every kilogram increase in the payload weight.

$$\frac{\partial W_{TO}}{\partial W_{PL}} = BW_{TO}\{D - C(1-B)W_{TO}\}^{-1} \tag{2.16}$$

The cruise segment is powered by both fuel and battery. The sensitivity of the take-off weight to the range for fuel powered segment for a range of 3500 km is estimated as 5.99 kg/km.

$$\frac{\partial W_{TO}}{\partial R} = FC_j\, V(L/D)^{-1} \tag{2.17}$$

The mission requires an extra loiter time of 45 minutes after the cruise segment and so, the take-off weight sensitivity due to the increase in loiter time is computed using the equation below. It results in a sensitivity of 1505 kg/hr. The signification of the sensitivity is that, if the loiter time is increase from 45 to 105 minutes, the take-off weigh will increase by 645 kg.

$$\frac{\partial W_{TO}}{\partial E} = FC_j\,(L/D)^{-1} \tag{2.18}$$

The specific fuel consumption and the lift-to-drag ratio are important to perform the mission without affecting the range or payload equation and so the sensitivities of cruise speed, lift-to-drag ratio and the cruise specific fuel consumption for the fuel -powered segment are calculated using the equations below. Also, the results obtained are tabulated in Table 2.3.

- Cruise speed (Fuel-powered segment)

$$\frac{\partial W_{TO}}{\partial V} = FR_{fuel}C_j\,(L/D)^{-1} \tag{2.19}$$

- Lift-to-drag ratio (Cruise segment)

$$\frac{\partial W_{TO}}{\partial (L/D)} = -FR_{fuel}C_j\left(V(L/D)^2\right)^{-1} \tag{2.20}$$

- Specific fuel consumption (Cruise segment)

$$\frac{\partial W_{TO}}{\partial C_j} = FR_{fuel}\,V(L/D)^{-1} \tag{2.21}$$

The sensitivity of take-off weight with respect to the lift-to-drag ratio and the specific fuel consumption for the loiter segment are computed using the equations below:

- Lift-to-drag ratio (loiter segment)

$$\frac{\partial W_{TO}}{\partial (L/D)} = -FEC_j\left(V(L/D)^2\right)^{-1} \tag{2.22}$$

- Specific fuel consumption (loiter segment)

$$\frac{\partial W_{TO}}{\partial C_j} = FE\,(L/D)^{-1} \tag{2.23}$$

where, F is the Breguet's partial, which is expressed as

$$F = -BW_{TO}{}^2\left(CW_{TO}(1-B-D)\right)^{-1} \tag{2.24}$$

The value of Breguet partial is 82803 kg obtained by substituting the constants B, C, and D and the take-off weight computed in the previous sections.

2.3.2 Range sensitivities

The electric powered segment of the aircraft is very sensitive to the range, as even a slight variation in the specific energy density and the total efficiency alter the range the aircraft can cover. The range sensitivities are computed using the Hepperle's method (Hepperle, 2012) for determining sensitivities of a battery-powered aircraft. The fuel weight is added in all the equations obtained from Hepperle's for computing the sensitivity for the hybrid aircraft. The battery weight is substituted in Equation (2.2) to obtain the range of the aircraft as:

$$R_{Battery} = E^{*}\eta_{battery}\frac{1}{g}\frac{L}{D}\left(\frac{W_{TO} - W_E - W_F - W_{PL}}{W_{TO}}\right) \tag{2.25}$$

The range of the battery powered segment is differentiated with respect to the mass of the aircraft and is expressed as:

$$\frac{\partial R}{\partial W_{TO}} = -E^{*}\eta_{battery}\frac{1}{g}\frac{L}{D}\left(\frac{W_{battery}}{{W_{TO}}^2}\right) \tag{2.26}$$

The sensitivity of the range with respect to the lift-to-drag ratio is computed using the relation:

$$\frac{\partial R}{\partial L/D} = E^{*}\eta_{battery}\frac{1}{g}\left(\frac{W_{TO} - W_E - W_F - W_{PL}}{W_{TO}}\right) \tag{2.27}$$

The sensitivity of range to the lift-to-drag ratio (L/D) shows that, to cover a long range, a high L/D is required.

$$\frac{\partial R}{\partial E^{*}} = \eta_{battery}\frac{1}{g}\frac{L}{D}\left(\frac{W_{TO} - W_E - W_F - W_{PL}}{W_{TO}}\right) \tag{2.28}$$

The summary of the weight and range sensitivities is presented in Table 2.3.

Table 2.3 Weight and range sensitivities

$\partial W_{TO}/\partial W_E$	1.1703
$\partial W_{TO}/\partial W_{PL}$	2.8433
$\partial W_{TO}/\partial R_{fuel}$	5.99 kg/km
$\partial W_{TO}/\partial E$	1505 kg/hr
$\partial W_{TO}/\partial V$	-11.9 kg/kmph
$\partial W_{TO}/\partial c_j$ (Cruise)	19033 kg/hr
$\partial W_{TO}/\partial\ (L/D)$ (Cruise)	-499 kg
$\partial W_{TO}/\partial c_j$ (Loiter)	2822 kg/hr
$\partial W_{TO}/\partial\ (L/D)$ (Loiter)	-51.3 kg
$\partial W_{TO}/\partial R_{battery}$	2 kg/km
$\partial R/\partial\ W_{TO}$	-0.12 km/kg
$\partial R/\partial\ (L/D)$	159 km
$\partial R/\partial\ E^{*}$	0.566 s^2/m

2.4 Parametric study

A trade study is performed to understand the influence of the parameters on the take-off weight. The trade study between the take-off weight and the lift-to-drag ratio shows that, for an increase in the L/D from 22 to 23, the take-off weight reduces by 13%. While increasing the lift-to-drag certainly reduces the take-off weight, the challenging issue will be dealing with high aspect ratio wings due to high L/D. The high aspect ratio wing is subjected to large amounts of bending stress and it generates higher amount of parasite drag due to the increased surface area of the wing. Therefore, considering the structural and the aerodynamic challenges on the high aspect ratio wing, the lift-to-drag ratio for the medium range hybrid business jet will not be modified at this preliminary stage of design.

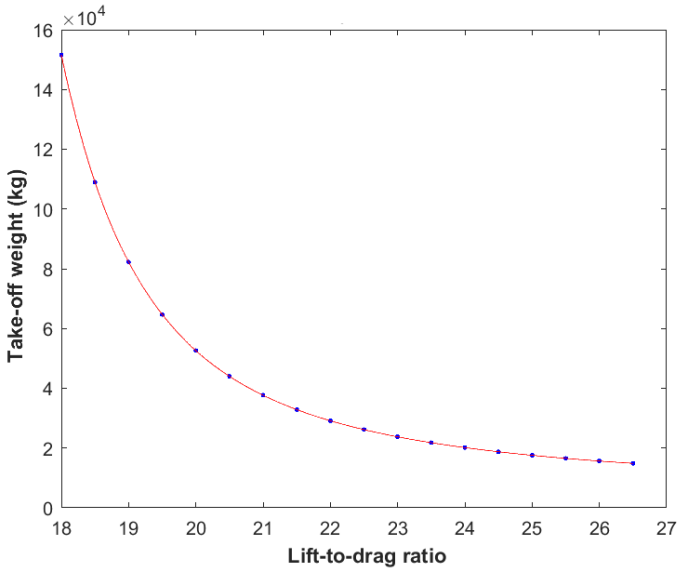

Figure 2.3 Take-off weight Vs. Lift-to-drag ratio

The next trade study is performed between the specific fuel consumption and the total take-off weight of the aircraft. The study shows a direct proportionality between the take-off weight and the specific fuel consumption (SFC). The SFC is the measure of the propulsion system efficiency and a smaller SFC reduces the take-off weight by means of reducing the amount of fuel required for the desired mission.

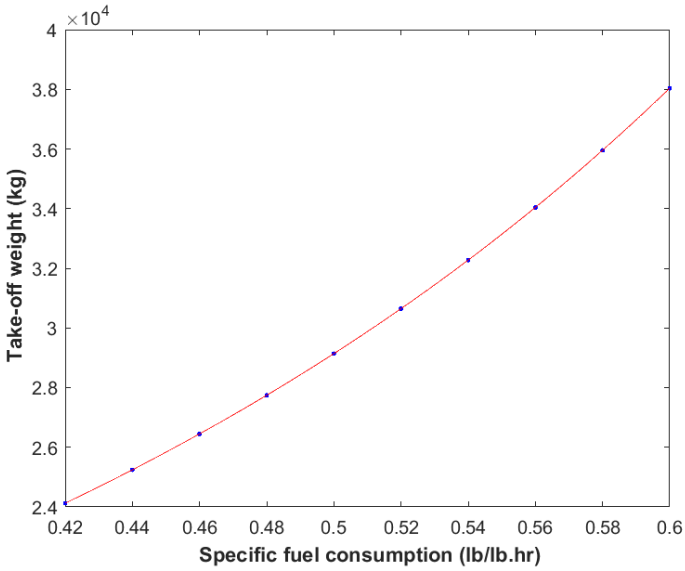

Figure 2.4 Take-off weight Vs. Specific fuel consumption

The take-off weight trade with respect to the specific energy density (E*) shows a significant reduction in the take-off weight for an increase in the specific energy density; but, the battery technology in the next 15-20 years is predicted to provide an E* of 1750 Wh/kg (Hepperle, 2012). For the preliminary design, the value of E* is assumed as 1750 Wh/kg.

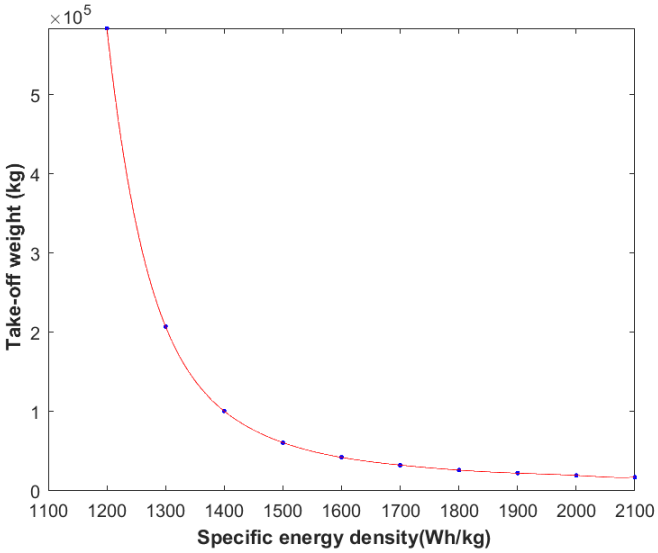

Figure 2.5 Take-off weight Vs. Specific energy density

The parametric study between the take-off weight and the payload capacity, shows a direct proportionality.

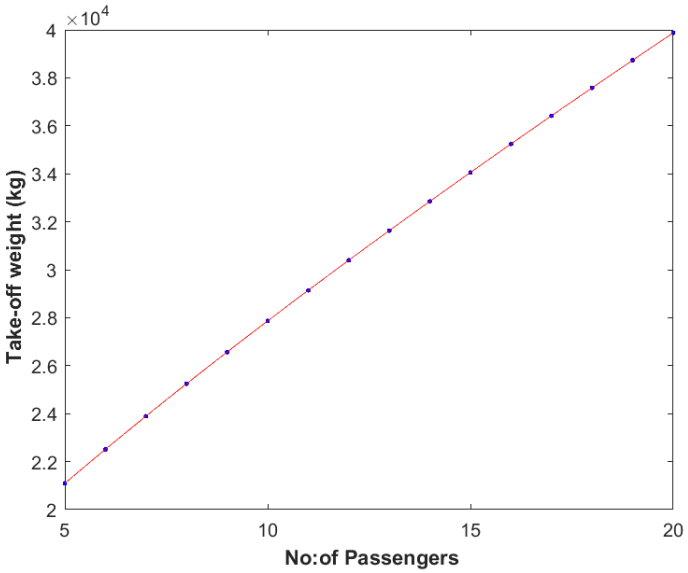

Figure 2.6 Take-off Weight Vs. Payload weight

The trade study between the take-off weight and battery efficiency is predicted to be critical as it affects the take-off weight and the range of the vehicle. If the efficiency is high, the battery weight required to perform the desired mission reduces, as the battery weight and the efficiency show an inverse relationship.

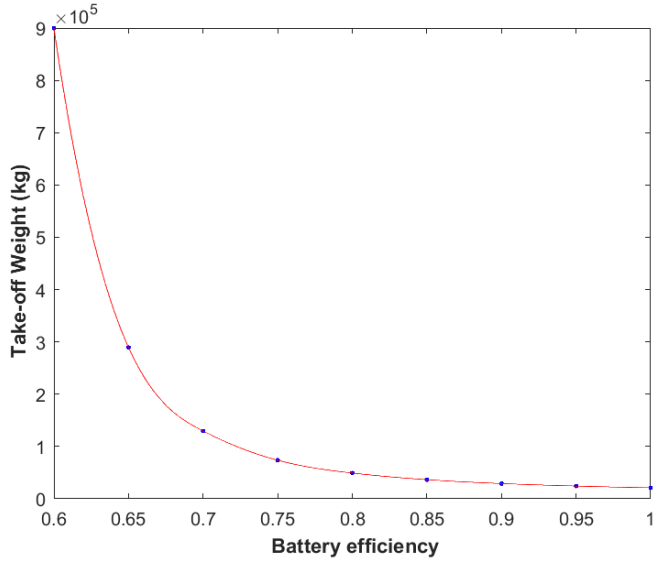

Figure 2.7 Take-off weight Vs. Battery efficiency

The trade study between the take-off weight and the range of the aircraft expressed in terms of battery percentage, shows a way to reduce the take-off weight by modifying the range percentage of the electric segment. The aircraft weight for a 60% fuel powered and 40% battery

powered Figure 2.8 is almost equal to that of a conventional model. On the other hand, the take-off weight for a 40% fuel and 60% battery powered model is twice that of the conventional ones. The project aims to design an aircraft that could rely on the battery for propulsion, as much as possible and a low take-off mass. Hence, the take-off weight is not modified at this stage of design, as the assumed parameters are predicted to be optimal choices considering the structural, aerodynamic and battery capabilities.

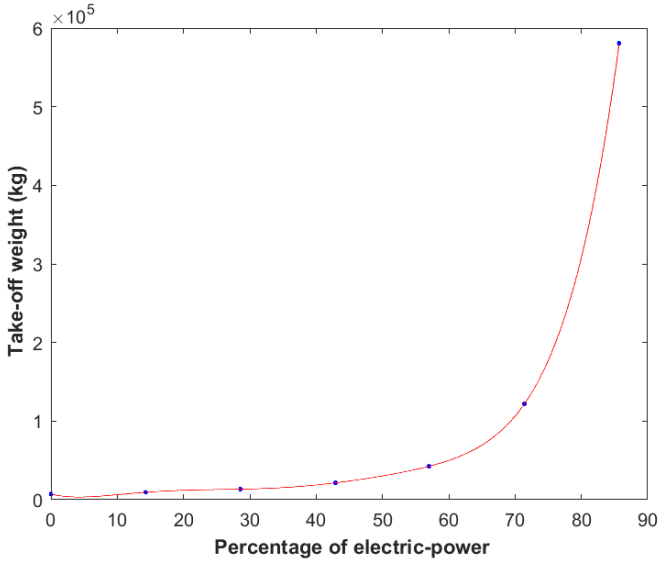

Figure 2.8 Take-off weight vs electricity percentage

The trade study between the range and the payload Figure 2.9 was conducted by keeping the take-off weight constant throughout in order to predict the best combination of the fuel and electricity percentage that provides the desired range with maximum payload. The trade study for the fuel alone, electric alone and a 50%-50% combination of fuel and electric regime were conducted. The area between the fuel and 50% fuel - 50% electric curve is the region with high percentage of fuel used for propulsion. In this segment, it is possible to achieve a range higher than the desired mission requirement and the payload capacity could be increased for the given take-off weight of 29112 kg. The area below 50% fuel and 50% electric curve, is the region which predominantly uses electricity for propulsion in which the payload capacity for a range is limited due to the additional battery weights. The primary objective of

this project is to design an aircraft with reduced fuel amount. The combination with 50% fuel and 50% electric is an ideal choice, as the amount of fuel used for the mission is reduced and also payload capacity is not compromised.

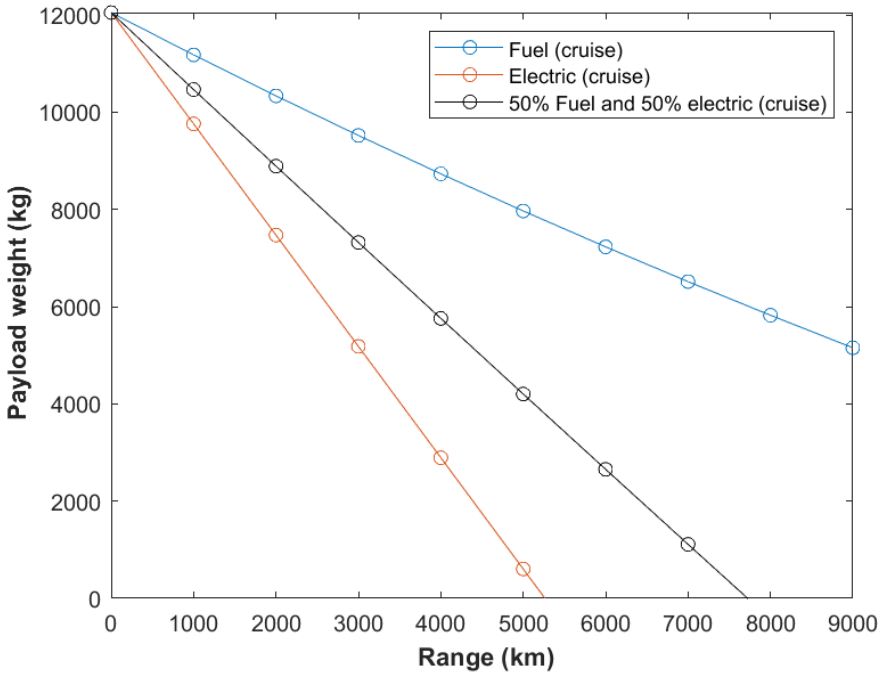

Figure 2.9 Range Payload trade study

2.5 Discussion and Conclusion

The take-off weight of the medium-range hybrid business jet is 30% greater than the weight of conventional business jets, which shows that the specific energy density of battery is low when compared to the aviation fuel. The aircraft is sized to meet the range and payload requirement. The lift-to-drag ratio is found to be the most critical parameter influencing the take-off weight of the aircraft. The achievable lift-to-drag ratio will be estimated in the final phase of preliminary design sequence i.e., drag polar estimation. The lift-to-drag ratio depends on the surface area of major components such as the fuselage, wing, and empennage.

3. Performance Constraints Analysis

3.1 INTRODUCTION

The thrust-to-weight ratio and wing loading are the major parameters associated with the propulsive and the aerodynamic performance of the aircraft. Estimating the thrust-to-weight ratio T/W and the wing loading W/S forms a crucial part of the aircraft design. Based on the mission requirements, the performance constraints to which the medium-range business jet must be sized will be discussed. The aircraft design parameters influencing the mission requirements such as the range, cruise speed, take-off distance, landing distance, and climb rate are wing area, take-off thrust, maximum required coefficient of lift for take-off and landing. The highest possible wing loading, and the lowest possible thrust-to-weight ratio will provide a plane with the lowest weight and the lowest cost (Roskam, *Airplane Design: Part I*, 2018).

3.2 Stall speed sizing

The medium-range, hybrid jet is in the FAR 25 certification category, for which there is no minimum stall speed requirement. The stall speed sizing will provide an allowable wing loading (W/S) for a given maximum lift coefficient. The stall speed is computed as a function of the wing loading and the coefficient of lift (Roskam, *Airplane Design: Part I*, 2018).

$$V_s = sqrt\left(\frac{2\,W}{\rho\; C_{L_{max}} S}\right) \tag{3.1}$$

The stall speed is plotted as a function of the wing loading and the maximum coefficient of lift in the figure below. The stall speed data will be used to compute the stall speed at take-off, landing and clean configuration based on the wing loading and maximum coefficient of lift values from the performance matching graph.

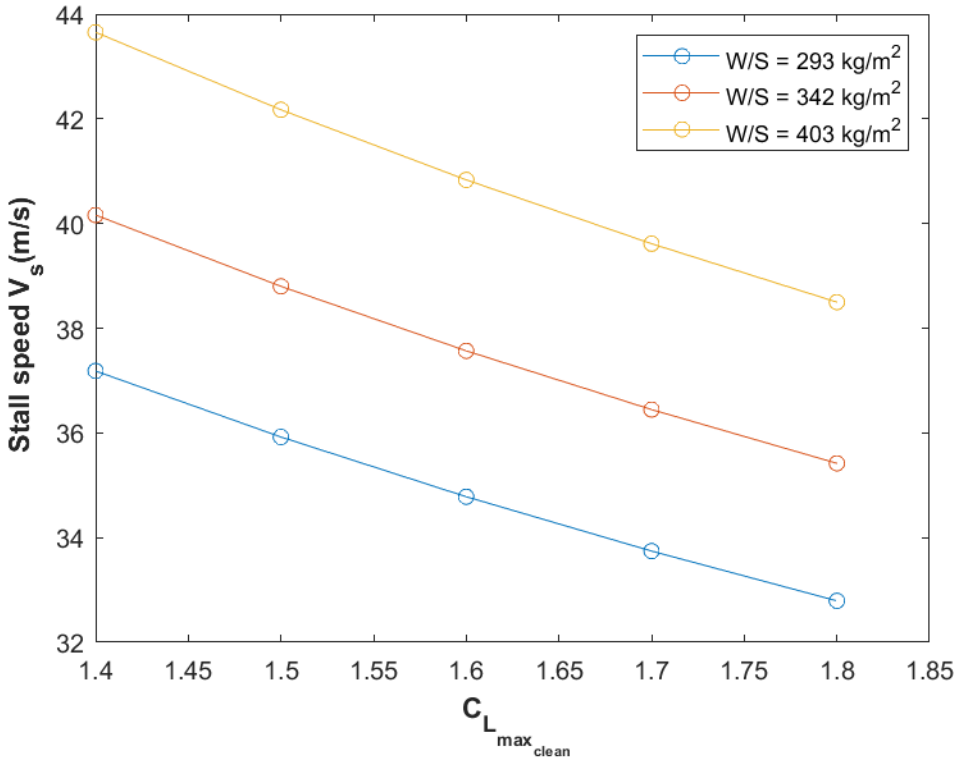

Figure 3.1 Stall speed sizing (Clean)

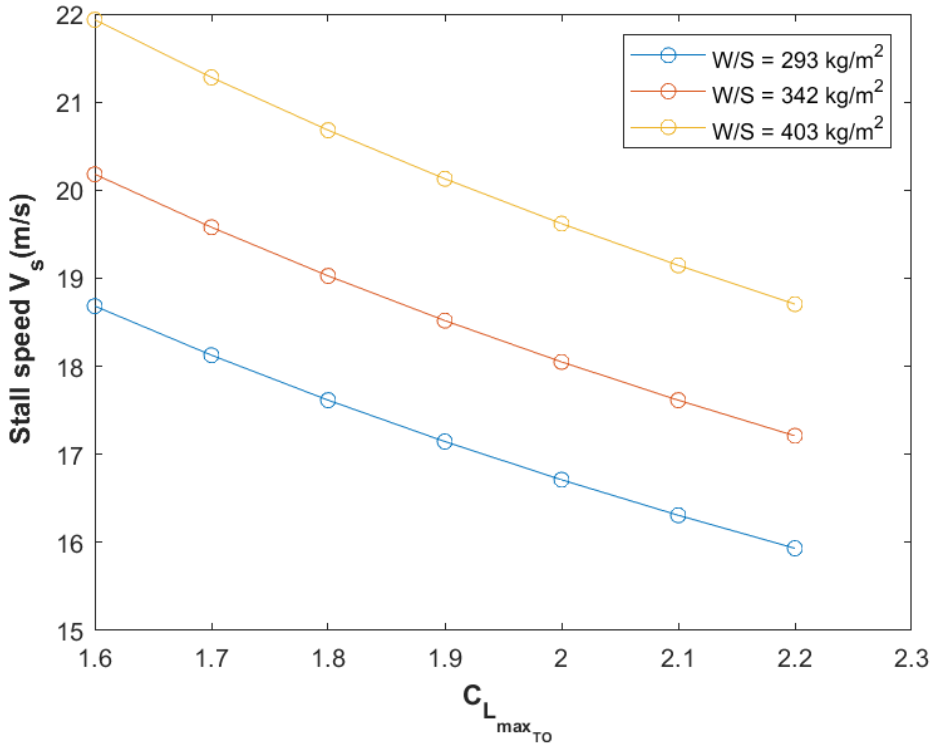

Figure 3.2 Stall speed sizing (Take-off)

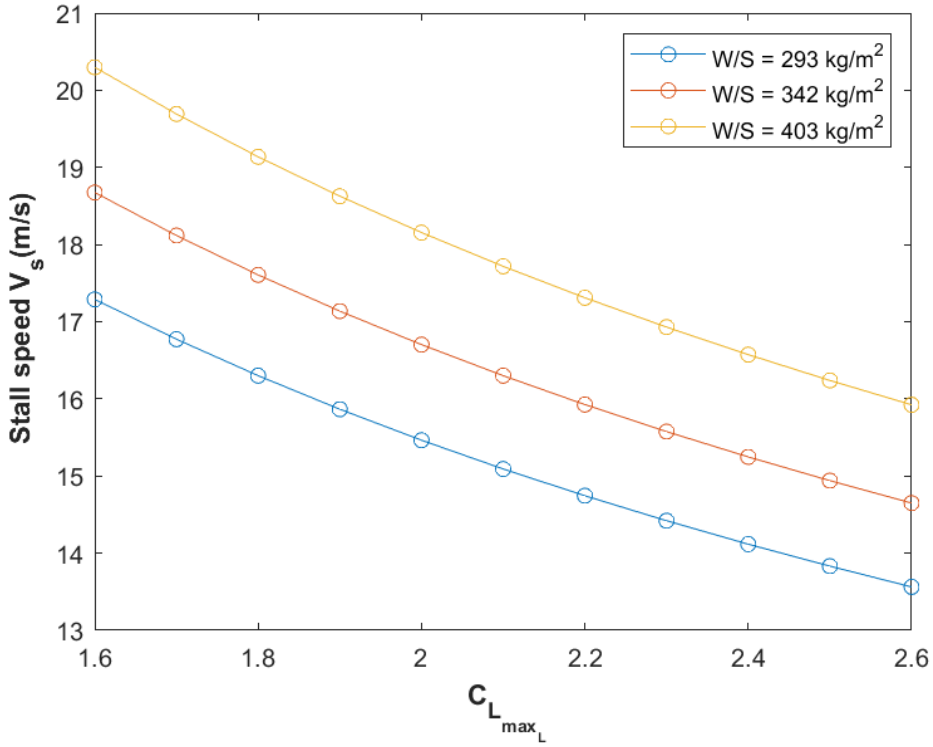

Figure 3.3 Stall speed sizing (Landing)

3.3 Take-off distance sizing

The take-off distance of the airplane is expressed as a function of the coefficient of lift at take-off, wing loading, density (ρ) at the take-off altitude, and the thrust-to-weight ratio. It is required to size the passenger aircraft so that the FAR 25 field length (S_{TOFL}) satisfies the condition:

S_{TOFL} < 1828 m (5984 ft) ft at 1524 m (5000 ft) altitude

The take-off field length is expressed as a function of the take-off wing loading during and the thrust-to-weight ratio as (Roskam, *Airplane Design: Part I*, 2018):

$$S_{TOFL} \propto \frac{(W/S)_{TO}}{\sigma C_{L_{max_{TO}}} (T/W)_{TO}} = TOP_{25} \tag{3.2}$$

$$\sigma = \frac{\rho_{TO}}{\rho_{Sea-level}} \tag{3.3}$$

TOP_{25} is the take-off parameter for FAR 25 aircraft. Roskam determined the proportionality constant in equation 3.2 to be 37.5 (Roskam, *Airplane Design: Part I*, 2018). Hence:

$$S_{TOFL} = 37.5 \frac{(W/S)_{TO}}{\sigma C_{L_{max_{TO}}} (T/W)_{TO}} = 37.5\, TOP_{25} \tag{3.4}$$

The TOP_{25} parameter for the take-off field length of 5984 ft is 159.9 lb/ft^2 or 780.7 kg/m^2. The density ratio for 5000 ft altitude is 0.8614. The maximum take-off coefficient of lift for the business jet category is 1.6 – 2.2 (Roskam, *Airplane Design: Part I*, 2018).

3.4 Landing distance sizing

The landing distance of airplanes is determined by five factors (Roskam, *Airplane Design: Part I*, 2018):

- landing weight W_L
- approach speed V_A
- deceleration method used
- flying qualities of the aircraft
- pilot technique

In the conventional aircraft, the fuel is burnt during cruise and the overall weight of the aircraft will be very less during landing when compared to the take-off. On the contrary, in a hybrid business jet, the battery weight will not be reduced even when the energy is extracted. Such factors are considered while designing the aircraft for meeting the landing requirement. The FAR field length is written as a function of the approach speed as:

$$S_{FL} = 0.3{V_A}^2 \tag{3.5}$$

The landing field length requirement is 1600 m (5249 ft). The approach speed is calculated as 132 knots by substituting the value of S_{FL} in ft in the equation above. The stall speed during

landing is expressed as a function of the approach speed as specified in the mission requirement:

$$V_{S_L} = \frac{V_A}{1.3} \tag{3.6}$$

The stall speed is 101 knots (51.9 m/s). The stall speed equation 3.1 is used to find the range of wing loading for the landing segment for maximum coefficient of lift. The range of maximum coefficient of lift for the business jet category is 1.6 – 2.6. The landing weight is assumed 95% of the take-off weight. The take-off wing loading is estimated by multiplying the $(W/S)_L$ by a factor of 0.95.

3.5 Climb requirement sizing

The FAR climb requirements are primarily for two flight conditions: take-off and balked landing. To size the aircraft to meet the climb requirement, the thrust-to-weight ratio is determined. The equations for sizing the aircraft to meet the necessary climb constraints are obtained from Roskam (Roskam, *Airplane Design: Part I*, 2018). The thrust-to-weight ratio for one engine inoperative (OEI) and All Engines Operating (AEO) are expressed as:

$$T/W = (N/(N-1))(1/(L/D)) + CGR \tag{3.7}$$

$$T/W = ((1/(L/D)) + CGR) \tag{3.8}$$

respectively where, CGR is the climb gradient, N is the number of engines. To compute the lift-to-drag ratio L/D for various flight segments, the drag polar is determined. The drag-polar is vital element to size an airplane for the climb requirement. The total drag is the summation of the profile drag (C_{D_o}) and the drag due to lift which is represented as:

$$C_D = C_{D_o} + KC_L{}^2 \tag{3.9}$$

$$K = \frac{1}{\pi(AR)e} \tag{3.10}$$

The aspect ratio is assumed as 8.7 and the Ostwald efficiency factor e for take-off, clean and landing segment are assumed as 0.8, 0.85, and 0.75 respectively based on data available in the reference (Roskam, *Airplane Design: Part I*, 2018).

Configuration	ΔC_{D_o}	e
Clean	0	0.80 - 0.85
Take-off flaps	0.010 - 0.020	0.75 - 0.80
Landing Flaps	0.055 - 0.075	0.70 - 0.75
Landing Gear	0.015 - 0.025	no effect

Figure 3.4 Zero-lift drag increment (Roskam, *Airplane Design: Part I*, 2018)

The profile drag or the zero-lift drag is a function of the equivalent parasite area (f) and the surface area of the wing.

$$C_{D_o} = f/s \tag{3.11}$$

The wetted surface area is estimated as 3800 ft^2 (353 m^2) using the following expression with c = 0.2263 and d = 0.6977, which are regression line coefficients for the take-off weight versus wetted surface area for the business jet category:

$$log_{10}s_{wet} = c + dlog_{10}W_{TO} \tag{3.12}$$

The equivalent parasite area is determined using the following relation:

$$log_{10}f = a + blog_{10}s_{wet} \tag{3.13}$$

The value of a and b in the equation above, depend on the skin friction coefficient. The coefficient of skin friction has a huge impact on the lift-to-drag ratio which in-turn might affect the mission requirement. Since, no compromise on the lift-to-drag ratio could be made, a brief study on the skin friction coefficient was carried out before making a considerable assumption. The average skin friction coefficient for all aircraft type is 0.0025 – 0.006 and the lowest skin friction is mostly found in commercial jets (Filippone,2000). This is because of the smooth nature of the surface. The skin friction coefficient is assumed as 0.0025 and the constants in the equation are a = -2.61095 and b = 1.000 which is obtained by interpolation of the skin friction coefficient data available in Roskam (Roskam, *Airplane Design: Part I*, 2018). This

results in the equivalent parasite area of 9.3 ft^2 (0.86 m^2). In addition to the parasite drag, there is certain increment in drag due to the take-off flaps, landing flaps, and landing gear which are assumed as:

$$\Delta C_{D_o} = 0.015 \text{ (Take-off flaps)}$$

$$\Delta C_{D_o} = 0.06 \text{ (Landing flaps)};\ \Delta C_{D_o} = 0.017 \text{ (Landing gear)}$$

The drag polar equations for various conditions are computed using the equations 3.9 and 3.10:

Cruise: $C_D = 0.0120 + 0.043{C_L}^2$

Take-off + gear-up: $C_D = 0.0270 + 0.0457{C_L}^2$

Take-off + gear-down: $C_D = 0.0440 + 0.0457{C_L}^2$

Landing + gear-up: $C_D = 0.0720 + 0.0488{C_L}^2$

Landing + gear-down: $C_D = 0.0890 + 0.0488{C_L}^2$

The FAR 25 requirements for climb sizing are presented in the table below:

Table 3.1 Climb sizing

FAR	Configuration	CGR	Condition
25.111 (OEI)	Gear up, Take-off flap	>0.012	$V = 1.2\ V_{STO}$
25.121(OEI)	Gear down, Take-off flap	>0	$V_{lof} = 1.1\ V_{STO}$
25.121(OEI)	Gear up, Take-off flap	>0.024	$V = 1.2\ V_{STO}$
25.121	Gear up, Flap up	>0.012	$V = 1.25\ V_{STO}$
25.121 (OEI)	Clean	>0.012	$V = 1.25\ V_S$
25.119 (AEO)	Balked landing	>0.032	$V = 1.3\ V_{SL}$
25.121 (OEI)	Balked landing	>0.021	$V = 1.5\ V_A$

The thrust to weight ratio in the climb segment depends on the lift-to-drag ratio (Equation 3.8). The drag polar equations are utilized to estimate the lift-to-drag for different segments. Before proceeding with the calculation of T/W, assumption of maximum coefficient of lift for take-off, landing and clean segment is required. The assumed values are:

$C_{L_{max_{TO}}}$ = 2.2; $C_{L_{max_L}}$ = 2.6; $C_{L_{max_{clean}}}$ = 1.4

The coefficient of lift for each segment is obtained by dividing the maximum coefficient of lift with the square of the velocity condition provided in the Table 3.1. The coefficient of drag is estimated using the drag polar for the corresponding segment. The thrust to weight ratio is estimated using the equation 3.7 and 3.8. The values are plotted in the matching graph. The MATLAB script used for computing the performance sizing is provided in Appendix C

3.6 Cruise speed sizing

The mission requires a cruise speed of 222 m/s (0.75 Mach) at 40,000 ft (12192 m). The cruise speed is a function of the wing loading and the lift coefficient. For a W/S, Aspect ratio AR, Oswald efficiency factor e and Coefficient of lift, the thrust to weight ratio required is (Roskam, *Airplane Design: Part I*, 2018):

$$(T/W)_{reqd} = \left(C_{D_o}\bar{q}S\right) + \left(\left({C_L}^2\bar{q}S\right)/\pi ARe\right) \tag{3.14}$$

3.7 Discussion of the Performance sizing results

The mission requirement demands the aircraft to take-off and land at a very high altitude of 5000 ft. The take-off distance and landing distance varies with respect to the altitude due to the change in densities. The equations for sizing to meet the take-off and landing show an inverse relationship to the density. To land or take-off from a high altitude, more lift and thrust are required as compared to sea-level. The additional coefficient of lift for take-off and landing are 1.8 and 2.6 respectively, which is computed from the matching graph, where FAR 25.121(OEI) – balked landing is the most critical requirement. The incremental lift-coefficient will be provided by take-off and landing flaps. The high-lift device design depends on the wing coefficient of lift and so, the surface area to generate additional lift will be determined after the wing sizing.

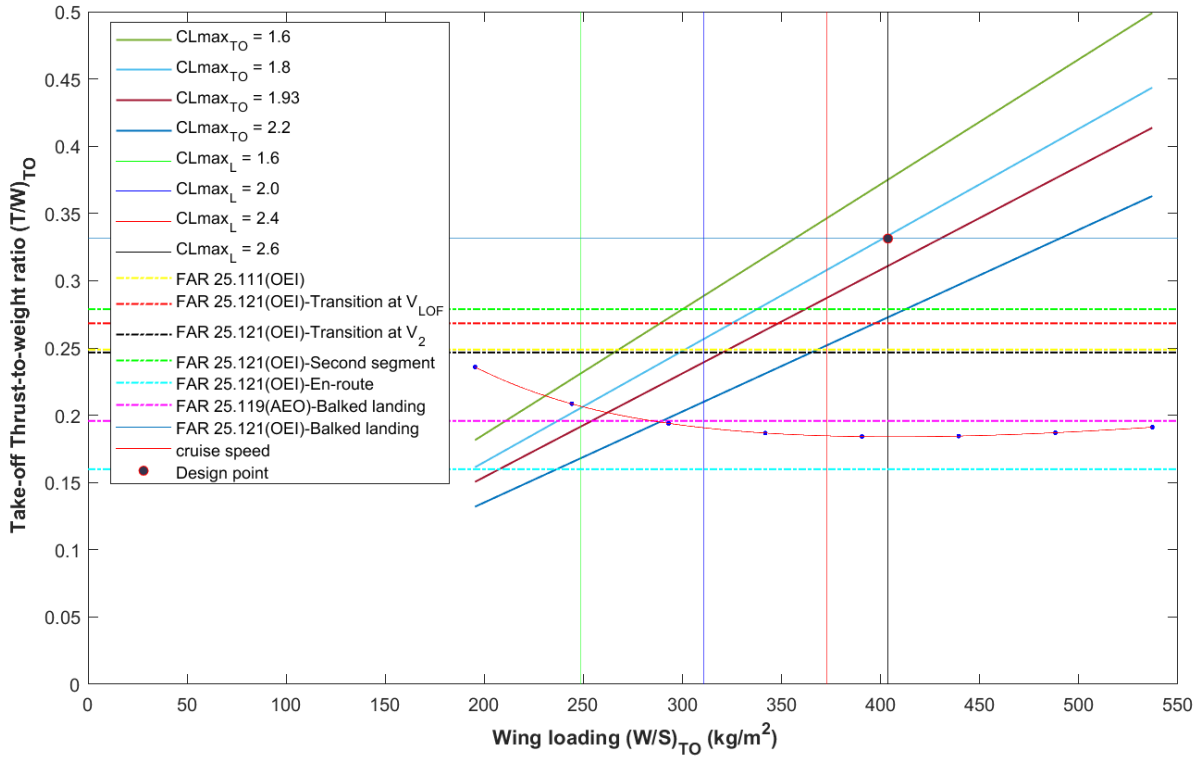

Figure 3.5 Performance sizing (Matching graph)

The results obtained from the matching graph's design point in Figure 3.5 are tabulated below:

Table 3.2 Performance sizing results

Take-off wing loading $(W/S)_{TO}$	403 kg/m^2
Take-off thrust-to-weight ratio	0.331
Take-off Thrust (T_{TO})	94529 N
Take-off lift coefficient ($C_{L_{max_{TO}}}$)	1.8 @ 5000 ft altitude
Landing lift coefficient ($C_{L_{max_L}}$)	2.6 @ 5000 ft altitude
Clean lift coefficient (C_{Lmax})	1.6
Wing Aspect Ratio (AR)	8.7
Stall speed (Take-off - 5000 ft)	20.68 m/s
Stall speed (Landing - 5000 ft)	15.62 m/s
Stall speed (Clean)	43.65 m/s

4. Configuration Selection

4.1 Introduction

Configuration selection is a crucial step in the design process that helps in determining the overall configuration of the aircraft required to meet the mission requirement. Typically, configuration selection includes the overall layout design as well as the integration of the propulsion system for the aircraft. The overall configuration layouts of all aircraft in a particular category have many similarities but have many differences in terms of the dimension and weight. The process of configuration selection is divided into two iterative preliminary design sequences (Roskam, Airplane Design Part II, 2018). In the preliminary design sequence I, it is possible to arrive at a conclusion about the feasibility of the certain configuration. The preliminary design sequence II focuses on detailed configuration layout for the necessary mission requirement (Roskam, Airplane Design Part II, 2018). In this chapter, the Class I (Preliminary design sequence I): configuration layout for the medium-range hybrid business jet is presented. The configuration layout includes the wing, fuselage, empennage, landing gear and the propulsion system. The configuration layout is entirely dependent on the mission specification.

4.1.1 Wing configuration

The wing configuration layout includes the type of wing support, number of wings and their vertical location. The aircraft can be classified based on the number of wings as: monoplane, biplane, triplane (Sadraey, 2013). The one wing configuration is mostly preferred in the commercial transport and the modern aircraft. Based on the type of wing they can be classified into cantilever construction and braced construction (Roskam, Airplane Design Part II, 2018). Most of the modern aircraft has a cantilevered wing. The truss-braced wing is currently in development, as they allow designers to choose high aspect ratio wing, to improve

the aerodynamic efficiency of the vehicle. Based on the vertical location of the wing, they are classified as: high-wing, low-wing, mid-wing, and parasol-wing. The low-wing provides better take-off performance when compared to the high-wing. The main advantage of low-wing is that the landing gear could be positioned below the wing and it can be retracted in the wing, or wing-fuselage fairing (Raymer, 2012). The mid-wing is generally not preferred, as it would not be ideal for the transport aircraft/cargo (Raymer,2012) as it reduces the cabin volume.

The wing configuration for the medium-range hybrid business jet features:

- low-cantilevered wing
- wing sweep to postpone the drag divergence, as the mission requires a high Mach in the cruise regime
- one-wing (monoplane configuration)
- high lift devices

In the performance sizing, it was identified that the aircraft requires additional coefficient of lift for take-off and landing, and hence, the wing will feature a high-lift device system. The batteries for propulsion will be stored in the wing and the wing will be designed to accommodate the batteries. The detailed design of the wing and the high lift device will be presented in the wing and high lift device design chapter.

4.1.2 Fuselage configuration

The fuselage for the medium-range hybrid business jet is a conventional one, like the existing business jet configuration. It will be designed to accommodate 11 passengers, 2 cockpit crew and 1 cabin crew. The fuselage will feature a galley, luxurious single-aisle cabin, and a cockpit. For a comfortable travel, the cabin will be designed with 2-seating abreast and 12 rows. Furthermore, the baggage compartment will be designed to hold a capacity of 238 kg. The location of the baggage compartment will be towards the tail of the fuselage.

4.1.3 Engine configuration

The number of engines is selected based on the thrust requirement from the performance sizing. The hybrid business jet's engine will differ from the conventional gas turbine engine, as the propulsion system should have the ability to allow fuel and electricity for operation. From the literature review, it was identified that the parallel hybrid propulsion system could be an ideal choice, as the mission requirement for the hybrid business jet includes both the fuel and electricity for cruise regime. The engines are typically located in the aft fuselage, in all the business jet aircraft, as it provides the required ground clearance as well as stability. Thus, the configuration for the medium-range hybrid business jet will follow the same. The engine configuration is a bi-jet, powered by two parallel-hybrid turbofan engines providing a net thrust of 94.5 kN and with an integrated motor to convert the electrical energy to the mechanical energy. The engine arrangement is of the pusher type, since the point of thrust applied is in the aft fuselage, which is behind the center of gravity. The engines installation is podded and disposition in the aft of fuselage. The arrangement and installation manner are decided using (Roskam, Airplane Design Part II, 2018). The parallel- hybrid turbofan engines are in the development stage and so, the length and diameter of the engine are approximately calculated based on the conventional engines used for the business jets.

4.1.4 Empennage configuration

The empennage is crucial for the stability of the aircraft. The configuration of the empennage relies entirely on the engine location. The medium-range hybrid business jet will feature a T-tail configuration, with the horizontal tail, above the vertical tail which is preferred for the aft-fuselage engine location, as it clears the tail from the engine exhaust gases. Furthermore, the effect of airflow from the wing and fuselage will not affect the flow over horizontal tail. The vertical tail is straight and perpendicular to the wing and it is in the aft of the fuselage. The location of horizontal tail on the vertical tail and also the location of vertical

tail from the fuselage nose will be estimated based on the center of gravity and stability and control analysis.

4.1.5 Landing gear configuration

The wing configuration strongly impacts the landing gear configuration. The landing gear for the medium-range hybrid business jet, is a retractable, tri-cycle gear in which the main gears are dispositioned below the wing and the nose gear is attached under the fuselage. The tri-cycle gear provides a better forward visibility to the pilot (Raymer,2012). The retractable landing gear reduce the interference drag during the cruise condition and improves the aerodynamic efficiency of the aircraft. The location of the main gears will be based on the stability of the aircraft. The number of wheels, strut length, location of the gear, clearance criteria during take-off and landing, and the loading capacity of the gear during landing will be discussed in the Class I landing gear design chapter.

5. Fuselage Design

5.1 Introduction

This chapter presents the cabin layout, cockpit layout and the overall fuselage layout of the medium-range hybrid business jet. The fuselage is designed to meet the mission requirements in terms of crew, passengers, and payload. The key elements for identifying the dimensions of the fuselage are (Roskam, *Airplane Design: Part II*, 2018):

- number and weight of crew members and passengers
- weight and volume of the baggage
- weight and volume of the fuel and batteries carried in the fuselage
- pilots' visibility from the cockpit

5.2 Fuselage layout

The medium-range hybrid business jet will feature a conventional fuselage designed to hold baggage, crew, and the passengers. The fuselage of a conventional configuration has three segments: Nose, Cabin, and Tail. The fuselage layout is prepared to ensure that the fuselage space is available for meeting the mission requirement without compromising on the structural and the aerodynamic considerations. Furthermore, the fuselage generate five types of drag such as (Roskam, *Airplane Design: Part III*, 2018):

- friction drag
- profile drag
- compressibility drag
- induced drag
- base drag

The fuselage contribution to the overall drag of the aircraft is about 25 – 50% (Roskam, *Airplane Design: Part III*, 2018) and so, the fuselage is shaped to reduce the overall drag of the aircraft.

5.2.1 Geometry of the fuselage

The length of the fuselage is defined as a function of the total take-off weight. The length is determined using the empirical relation (Raymer, 2012):

$$l_F = A * W_{TO}^{C} \tag{5.1}$$

For a jet transport airplane, the constants as defined in the reference are A = 0.67 and C = 0.43.

$Length\ of\ the\ fuselage\ l_F = 0.67 * (64181\ lb)^{0.43}\ =\ 78.21$ ft or 23.84 m

The diameter of the fuselage depends on the fineness ratio, which is the ratio of length to the diameter of the fuselage. The selection of fineness ratio has an influence on the fuselage drag coefficient. The effect of the fineness ratio on the fuselage drag is shown in the figure below:

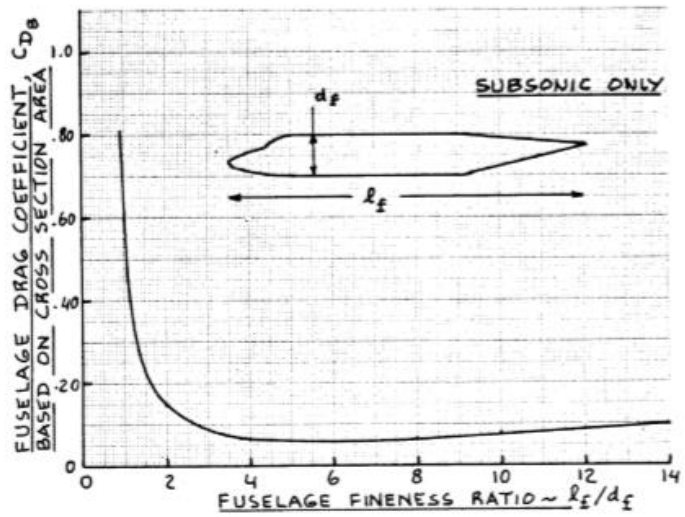

Figure 5.1 Effect of fineness ratio on fuselage drag (Roskam, *Airplane Design: Part III*, 2018)

In fuselage design, it is important to reduce the overall drag contribution from the fuselage. One of the ways to reduce the drag is by choosing a fineness ratio in the range 4 – 10 as this is the region where the fuselage drag is at a minimum. A fuselage fineness ratio of 9.5 is chosen for the preliminary sizing of the medium range hybrid business jet using the

geometric data provided in the figure below. Another important factor in the fuselage design is the fuselage cone fineness ratio, which depends on the length of the tail cone and the diameter of the fuselage. A low fineness ratio of the fuselage cone will result in a fuselage with less weight, but a large base drag penalty and a very high fineness ratio will result in large friction drag and large weight penalty (Roskam, *Airplane Design: Part II*, 2018). The tail cone ratio is assumed as 3 and the tail cone angle as 6^o using the geometric data for the business jet category.

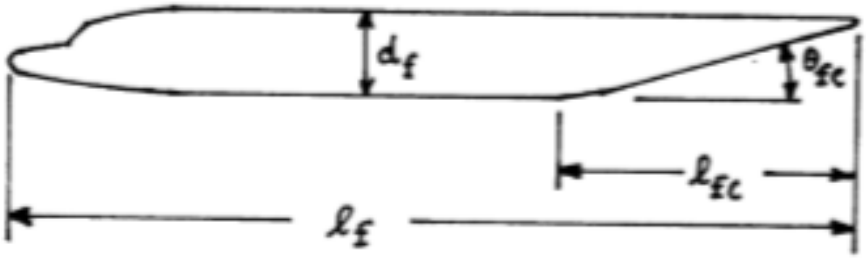

Airplane Type	l_f/d_f	l_{fc}/d_f	θ_{fc} (deg)
Homebuilts	4 - 8	3*	2 - 9
Single Engine	5 - 8	3 - 4	3 - 9
Twins	3.6** - 8	2.6 - 4	6 - 13
Agricultural	5 - 8	3 - 4	1 - 7
Business Jets	7 - 9.5	2.5 - 5	6 - 11
Regionals	5.6 - 10	2 - 4	15 - 19***
Jet Transports	6.8 - 11.5	2.6 - 4	11 - 16
Mil. Trainers	5.4 - 7.5	3*	up to 14
Fighters	7 - 11	3 - 5*	0 - 8
Mil. Transports, Bombers and Patrol Airplanes	6 - 13	2.5 - 6	7 - 25****
Flying Boats	6 - 11	3 - 6	8 - 14
Supersonics	12 - 25	6 - 8	2 - 9

*Tailcone as defined by Figure 4.1 not easily defined
**Cessna 336 (Fig.3.9c) ***Embraer Brasilia (Fig.3.16d)
****Lockheed Hercules (Fig.3.29d)

Figure 5.2 Fuselage geometric data (Roskam, *Airplane Design: Part III*, 2018)

The diameter of the fuselage is computed by substituting the length of the fuselage obtained using Equation 5.2 and the assumed fineness ratio using the following equation:

$$\lambda_f = l_F / D_f \tag{5.2}$$

Diamater of the fuselage $D_f = 23.84\,m/9.5 = 2.51\,m$

The tail cone length is calculated using the tail cone fineness ratio. The length of the tail is obtained as 7.53 m. The area of the cross section of the fuselage is 4.18 m^2, which is computed for a cylindrical fuselage cross section. The height of the fuselage is assumed as 2.6 m. The dimension also includes the structural depth = 0.02 * $W_{\underline{if}}$ + 1 inch. The width of the fuselage is computed using the formula:

$$W_{ef} = 4A_f / \pi h_f \tag{5.3}$$

The internal width of the fuselage to account for the structural depth is obtained as 2.35 m and the external width is 2.42 m. The length of the cabin is assumed as 11 m. The length of the fuselage nose is computed using the following equation:

$$l_N = l_f - l_C - l_{fc} \tag{5.4}$$

The dimensions of the fuselage are tabulated below:

Table 5.1 Summary of Fuselage geometry

Parameter	**Value**
Fuselage fineness ratio (λ_f)	9.5
Fuselage cone fineness ratio (λ_{fc})	3
Length of the fuselage (l_f)	23.83 m
Length of the nose (l_n)	5.31 m
Length of the tail (l_t)	7.53 m
Length of the cabin (l_c)	11 m
Tail cone angle (Θ_{fc})	6^o
Cabin width ($W_{\underline{if}}$)	2.35 m
Cabin height (h_c)	1.88 m
Fuselage height (h_f)	2.6 m

The luggage containers will be stored in the tail of the fuselage. The volume required to store the luggage containers is computed using the typical luggage density and also the total weight of the baggage. The Typical luggage density is 200 kg/ m^3 (Roskam, *Airplane Design: Part I*, 2018) The total weight of the baggage is 238 kg and thus the volume required to store the baggage is 1.19 m^3.

5.3 Cabin layout

The dimensions of the human body decides the minimum cabin size required to accommodate the passengers. The number of seats abreast is decided based on the width of the fuselage. The width of the fuselage allows for two abreast seating in the business class. Also, the statistical relationship between the fuselage width and the total seat width (Roskam, *Airplane Design: Part III*, 2018) shows that a single aisle is sufficient. The minimum allowable width of the aisle between the seats is chosen based on the emergency evacuation considerations. The cabin seating is designed with a seat pitch of 1.2 m, to provide comfort to the passengers during the flight. The cabin also features a galley, lavatory, and a wardrobe closet. The length of the cabin is assumed as 11 m. The dimensions of the cabin are specified in the cabin layout diagram. There are two forward galleys near the cabin door. The lavatory and wardrobe sections are in the aft part of the fuselage. The dimensions are:

- aft- wardrobe: 1 m x 0.5 m x 1.88 m
- aft- lavatory: 1 m x 0.5 m x 1.88 m
- forward galleys: 0.3 m x 0.5 m x 1.88 m

The cabin door is near the galley area with a height of 1.88 m and a width of 0.8 m. The layout of the cabin is designed using SOLIDWORKS and the pictures and dimensions are shown in the Figures 5.3 – 5.5.

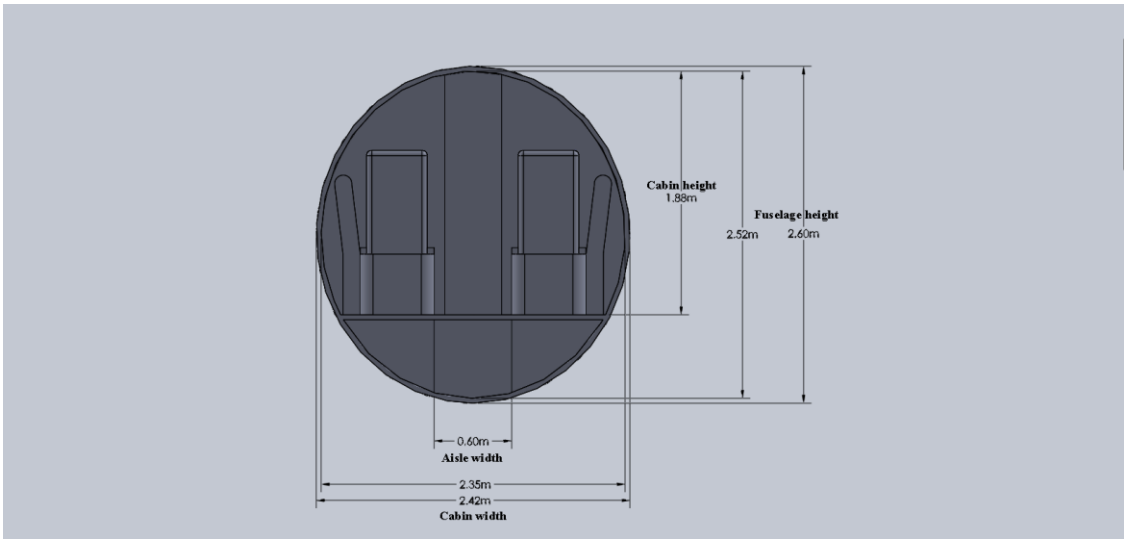

Figure 5.3 Front view of the hybrid jet's cabin

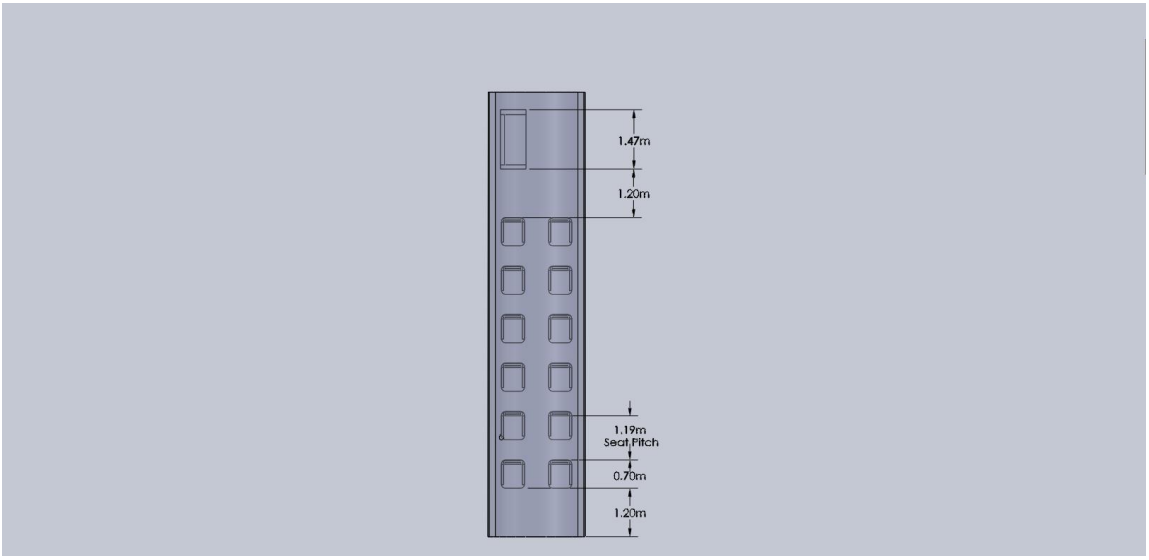

Figure 5.4 Initial cabin layout – Top View

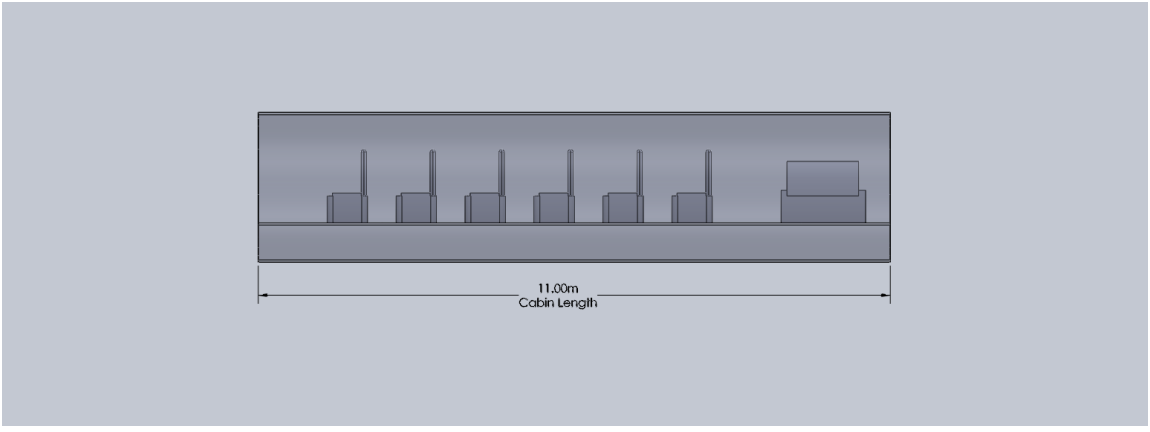

Figure 5.5 Sideview of the hybrid jet's cabin

5.4 Layout design of the cockpit

The dimensional limitation of the human body is accounted for the design of the cockpit. The following factors were considered while preparing the layout of the cockpit based on the methodology for cockpit layout in (Roskam, *Airplane Design: Part III*, 2018):

- the cockpit crew members are positioned in such a way that they can reach all the controls comfortably from the reference position
- the comfortable view of the flight essential instruments to the crew members without undue effort
- to enable communication by voice and touch without undue effort
- visibility from the cockpit adhering to certain minimum standards

Furthermore, human bodies vary greatly in geometrical dimensions. The dimensions of the crew members are fixed based on the baseline data for the standing male crew member available in (Roskam, *Airplane Design: Part III*, 2018). The weight of the crew member is assumed as 79 kg. The cockpit allows a considerable amount of adjustment in order to account for the variation in dimensions of the human body. The variation in the dimensions measured in adults are as follows (Roskam, *Airplane Design: Part III*, 2018):

- variation in arm length: +/- 15 cm
- variation in leg length: +/- 20 cm
- variation in sear-eye distance: +/- 12 cm

The figure below shows the typical dimensions of the standing, male crew member obtained from the (Roskam, *Airplane Design: Part III*, 2018).

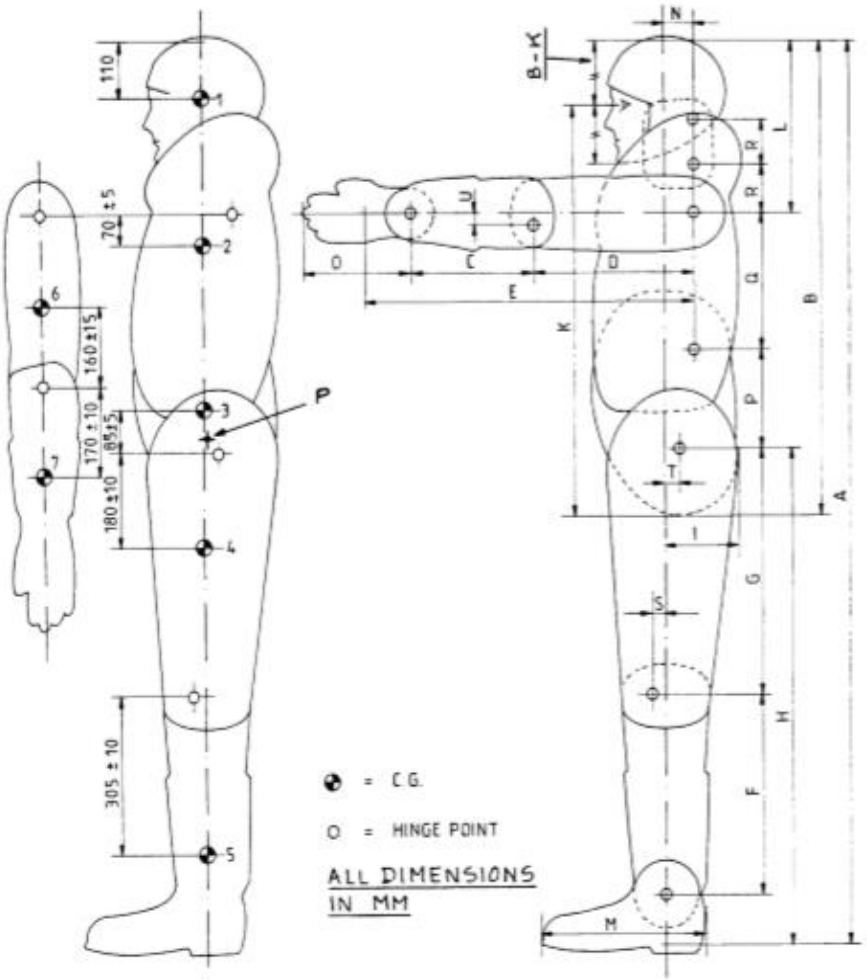

A	B	C	D	E	F	G	H	I	K	L
1,600	870	230	300	620	350	435	850	140	760	300
1,750	920	255	335	685	390	475	950	150	805	330
1,900	990	280	370	750	430	515	1,050	160	875	360

A	M	N	O	P	Q	R	S	T	U
1,600	300	50	200	190	260	80	25	20	20
1,750	325	60	220	200	270	90	30	30	20
1,900	350	70	240	210	280	100	30	30	20

Figure 5.6 Typical dimensions of a standing male crew member (Roskam, *Airplane Design: Part III*, 2018)

The aircraft will be controlled by side-stick controllers. The side-stick controllers are placed on the port side for the pilot and on the starboard side for the co-pilot. The typical cockpit seating arrangement for the stick-controlled aircraft is shown in the figure below (Roskam, *Airplane Design: Part III*, 2018):

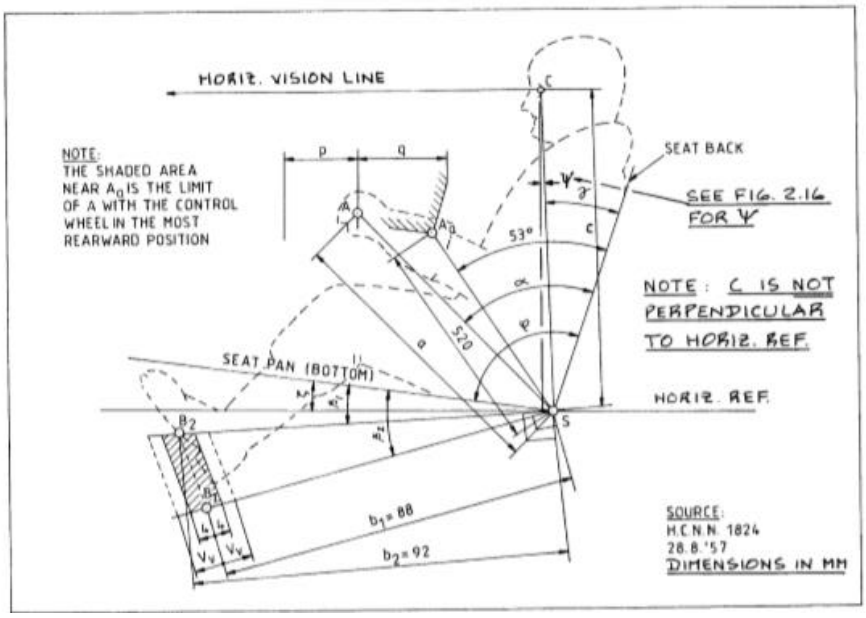

Figure 5.7 Seat arrangement for the stick-controlled aircraft (Roskam, *Airplane Design: Part III*, 2018)

Based on the standard dimensions for the cockpit (Roskam, *Airplane Design: Part III*, 2018) the parameters are tabulated below:

Table 5.2 Dimensions for civil cockpit control and seat adjustments (Roskam, *Airplane Design: Part III*, 2018)

Symbol	Dimension	Symbol	Linear dimension (cm)
ξ	7^o (+/- 2^o)	a	63 (+/- 4)
β_1	22^0	P	16 (+/- 2)
β_2	10^o	q	20 (+/- 2)
γ	21^0 (+/- 1^o)	r	15 (+/- 2)
α	70^0 (+/- 3^o)	c	77 (+/- 2)
φ	102^0 (+/- 2^o)	Vv	7 (+/- 2)
U_v	10 (+/- 2)	S_h	< 10

5.4.1 Determination of Visibility from the cockpit

During take-off and landing, the pilot must have a good visibility of the surroundings from the cockpit. The cockpit is designed based on the minimum cockpit visibility rules for civil transport aircraft. Generally, the visibility is the angular area obtained by intersecting the

cockpit with the radial vectors emanating from the pilot's eyes. The minimum recommended visibility pattern for the port side of the aircraft and the ideal visibility pattern for the transport aircraft (Roskam, *Airplane Design: Part III*, 2018) are shown in the figures below:

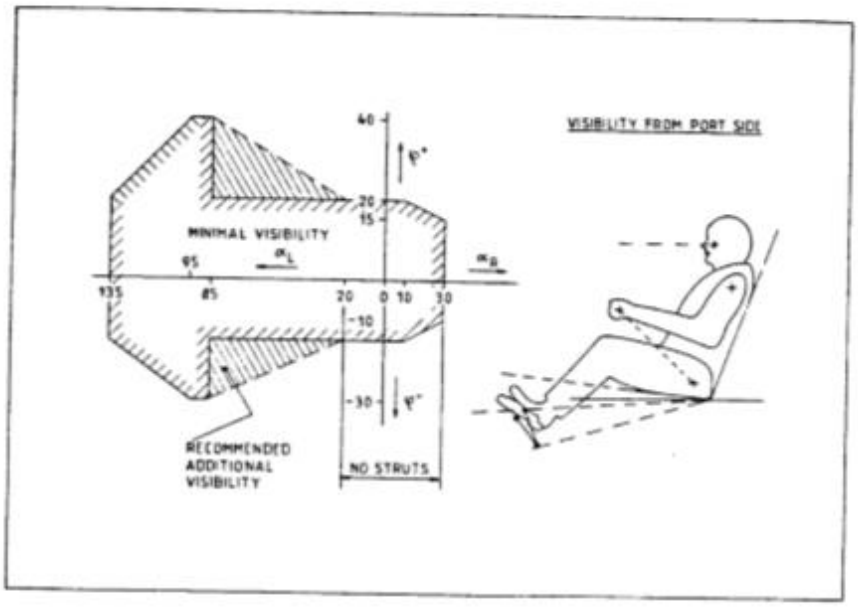

Figure 5.8 Minimum visibility pattern for the port side (Roskam, *Airplane Design: Part III*, 2018)

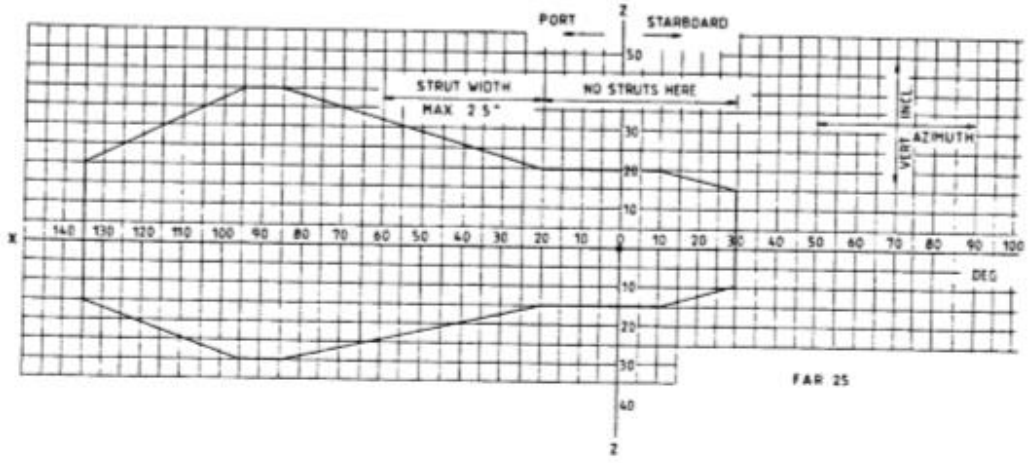

Figure 5.9 Ideal minimum visibility pattern for the transport aircraft (Roskam, *Airplane Design: Part III*, 2018)

The layout of the cockpit and the nose design for the medium-range hybrid business jet is done by considering the visibility factor and the space requirement for pilot in the cockpit.

All the CAD diagram presented below as well as their constituent building parts are prepared using SOLIDWORKS.

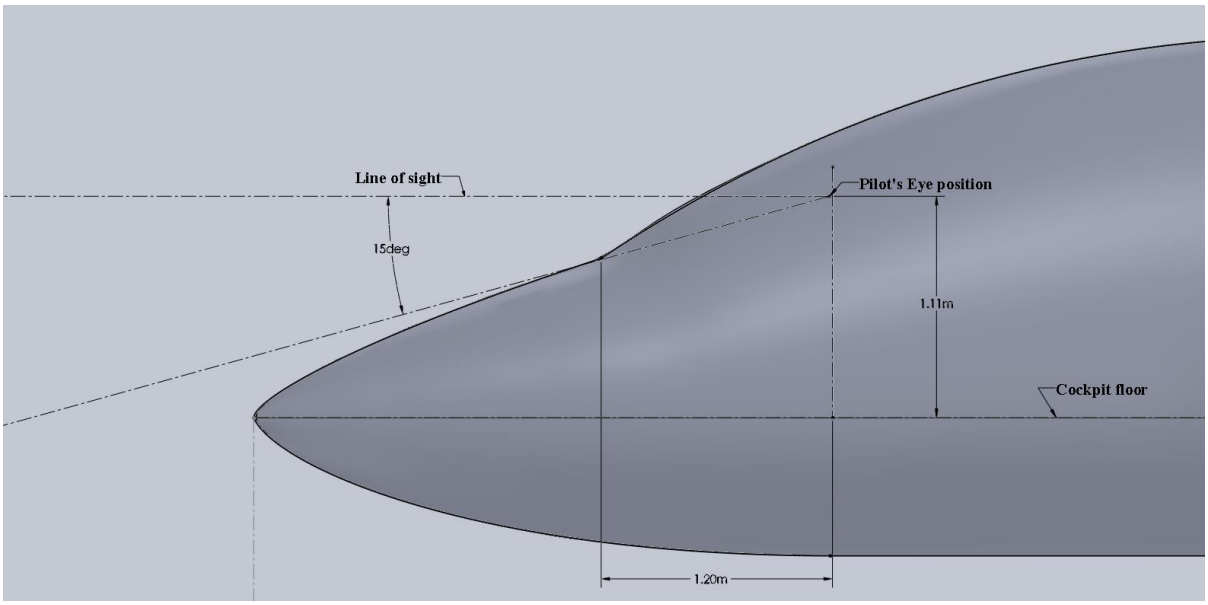

Figure 5.10 Visibility from the cockpit of the hybrid business jet

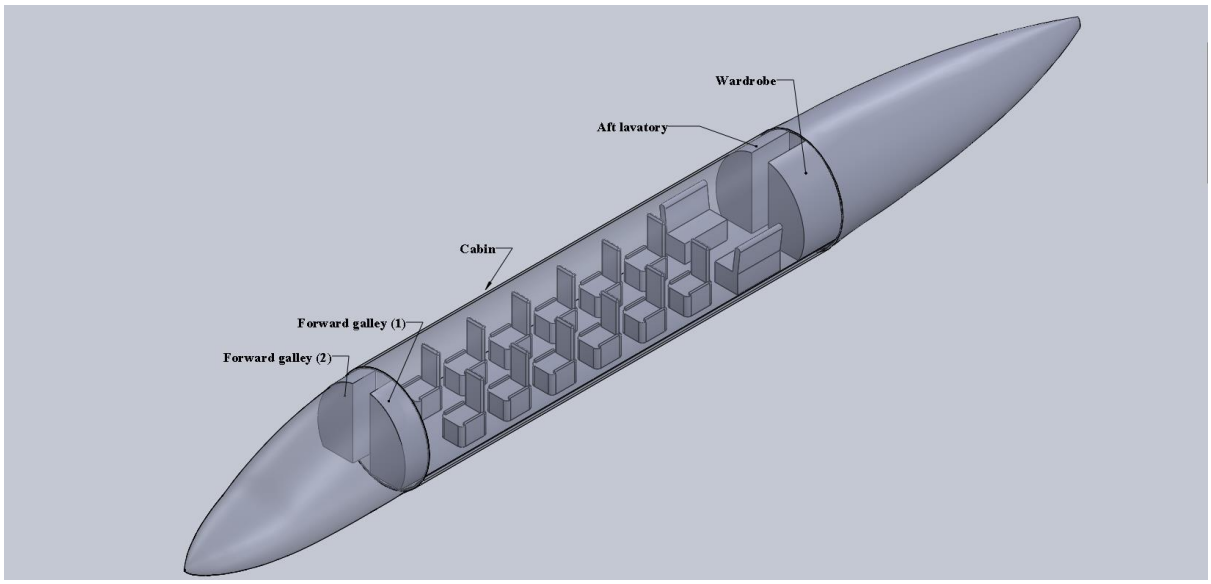

Figure 5.11 Isometric view of the hybrid business jet's fuselage

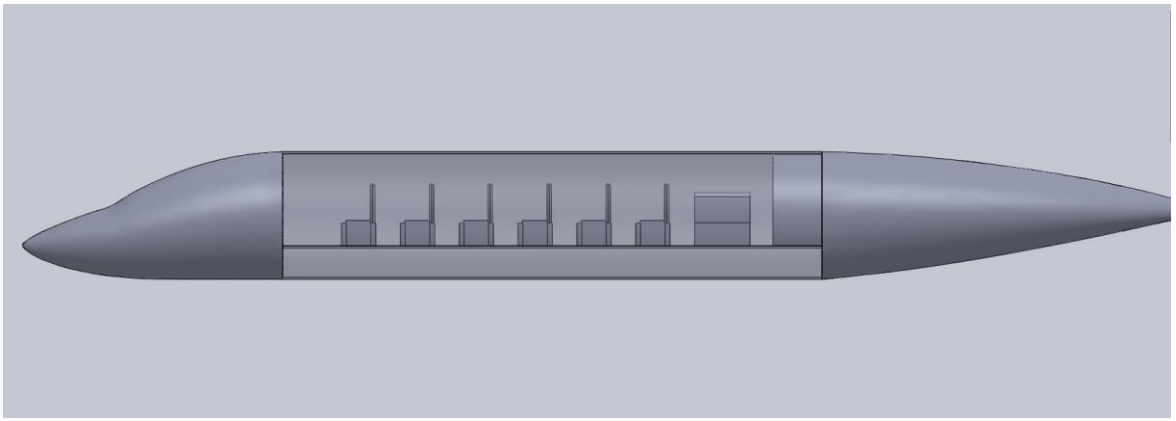

Figure 5.12 Side view of the hybrid business jet's fuselage

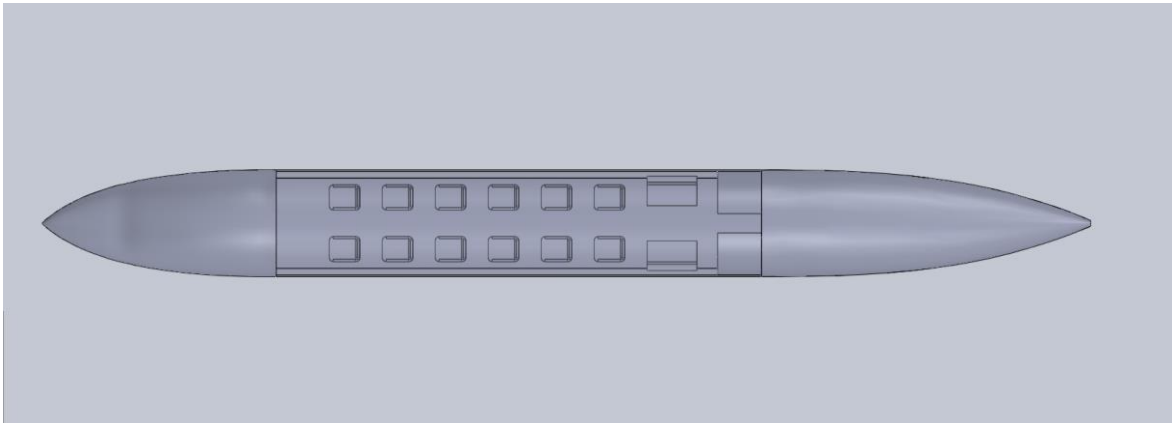

Figure 5.13 Top view of the hybrid business jet's fuselage

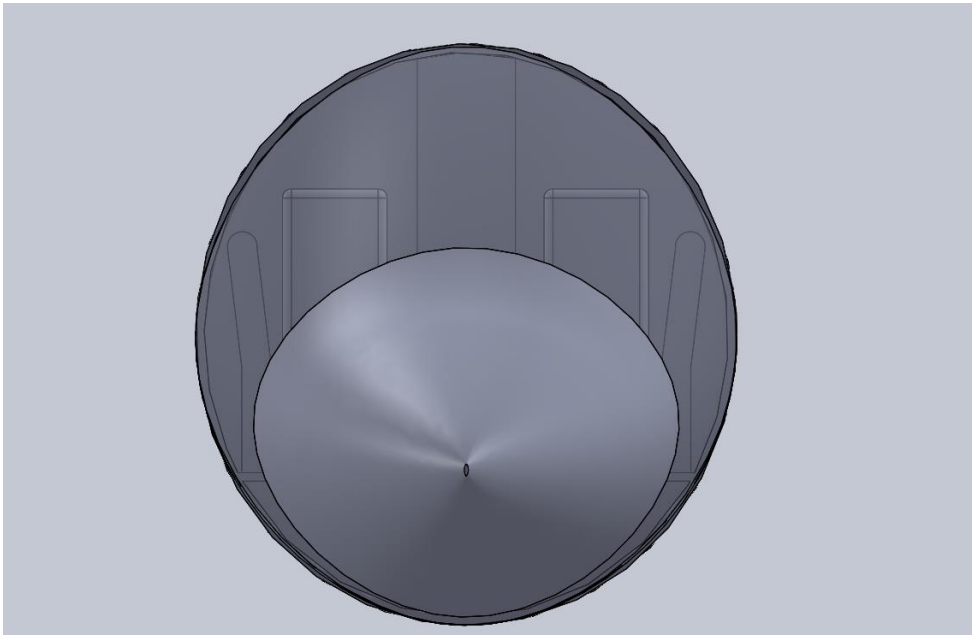

Figure 5.14 Front view of the hybrid business jets' fuselage

6. Wing, High-lift system, and lateral control design

6.1 Introduction

In chapter 4, the proposed wing configuration was a low-cantilever wing with aft-sweep. In the performance sizing chapter, it was identified that a wing loading of 403 kg/m^2 is required to meet the mission requirement. Also, the wing is designed for a high aspect ratio of 8.7 with a high lift-to-drag ratio, for the purpose of reducing the overall weight of the aircraft. The parameters of primary importance for designing the wing are as follows:

- wing plan form area
- number of wings
- vertical position relative to the fuselage (high, mid, or low wing)
- aerofoil selection
- wingspan
- taper ratio
- mean aerodynamic chord
- twist angle (α_t)
- sweep angle (Λ)
- dihedral angle (Γ)
- wing incidence angle, (α_i)
- high lifting devices and lateral control surfaces
- lateral control surfaces
- volume available for battery storage

6.2 Wing design

The primary goal is to make sure that the wing(s) is (are) suitable for all flight regimes and the necessary mission requirements. The wing design is an iterative process, in which the process is carried out several times until the mission requirements and the performance requirements are met.

6.2.1 Number of wings and the vertical location of the wing

The aircraft is classified into three types based on the number of wings: monoplane, bi-plane, triplane (Sadraey, 2013). The medium-range hybrid business jet will fall into the monoplane category, since one-wing is the most preferred option in conventional modern aircraft. The low wing reduces the landing gear weight and provides more cabin volume. The horizontal location of the wing from the fuselage nose will be decided while analysing the weight and balance of the aircraft.

6.2.2 Surface area of the wing

The wing surface area is identified using the wing loading and the take-off weight of the aircraft; Higher the surface area, higher will be the amount of lift produced. On the other hand, it also increases the induced drag of the aircraft. The take-off weight and the wing loading are obtained from the weight estimation and performance sizing, respectively.

$$S = \frac{W_{TO}}{(W/S)} \tag{6.1}$$

For a W_{TO} = 29112 kg and W/S = 403 kg/m^2, Surface area S = 72.12 m^2.

6.2.3 Wingspan

The wingspan is defined by the following relationship which shows a direct proportionality with the aspect ratio and the surface area of the wing:

$$b = \sqrt{AR \cdot S} \tag{6.2}$$

6.2.4 Root chord, tip chord and mean aerodynamic chord

In a rectangular wing, high amount of lift is generated. An untwisted rectangular wing produce 7% more drag than elliptical planform. Tapering the wing modifies the lift distribution over the wing. If the wing is tapered, the tip chord become smaller averting the high lift generated on the tip (Raymer, 2012). Taper ratio is the ratio of the tip chord to the root chord. Although tapering of the wing has certain disadvantages in terms of the stability, cost, and ease of manufacturing. It improves the aerodynamic efficiency of the aircraft as it minimizes the induced drag of the aircraft. The taper ratio of the wing is assumed as 0.15. The root chord, tip chord, and the mean aerodynamic chord of the aircraft are computed with the following relations (Raymer, 2012):

$$Root\ chord\ \ C_r = \frac{2S}{b(1+\lambda)} \tag{6.3}$$

$$Tip\ Chord\ C_t = \lambda C_r \tag{6.4}$$

$$Mean\ Aerodyamic\ chord\ \bar{C} = \frac{2}{3} C_r \frac{1+\lambda+\lambda^2}{1+\lambda} \tag{6.5}$$

Furthermore, the mean aerodynamic centre is computed using the taper ratio, mean aerodynamic chord and the span of the wing. The MAC along the X and Y axis of the wing are computed using the formula (Raymer, 2012):

$$\overline{X} = 0.25\overline{C}\ ;\ \overline{Y} = \frac{b}{6}\frac{(1+2\lambda)*(1+\lambda)}{1} \tag{6.6}$$

6.2.5 Dihedral

The wing dihedral lifts the tip of the wing higher than the root. The dihedral improves the lateral stability of the aircraft by providing restoring moment that brings the aircraft to its original trim level flight condition if disturbed by a sudden gust along the lateral axis of the aircraft. Moreover, the dihedral provides ground clearance for the engines, nacelles, propellers etc. For the preliminary sizing of the wing, a dihedral of 2^0 is chosen. The dihedral angle could be optimized based on the detailed stability and control analysis of the aircraft.

6.2.6 Airfoil selection

The selection of airfoil is a crucial part in the design as it is the primary part of the wing that generates the lift. If the airfoil is selected based on the design cruise lift coefficient, the aerodynamic efficiency and the overall efficiency in the cruise region could be improved, resulting in better performance.

The first step in airfoil selection is the selection of the design cruise lift coefficient which depends on the dynamic pressure at the cruise altitude (q') and the surface area of the wing. While the required cruise lift coefficient for the fuel segment varies as a function of the amount of fuel burnt, the required cruise lift coefficient for the battery segment will remain constant. Hence it is important to choose an optimal design point. The cruise lift coefficient for a fuel-powered aircraft is calculated for 40% of the fuel burnt (Roskam, *Airplane Design: Part II*, 2018). The cruise lift coefficient for the fuel-powered segment is plotted as a function of the fuel burnt using the formula below:

$$C_{L_{cr}} = (W_{TO} - W_f)/(q'S) \tag{6.7}$$

The selection of design point depends on the time at which the aircraft uses electricity for propulsion. If the battery power is turned on after 20% of the fuel is burnt, the required C_L is 0.51. Whereas, if it is turned on after 50% of the fuel is burnt, the required C_L is 0.48. It is assumed that the battery power will be in effect after 40% of the fuel is burnt and the corresponding cruise lift coefficient is 0.4936, which will remain constant throughout the battery powered segment.

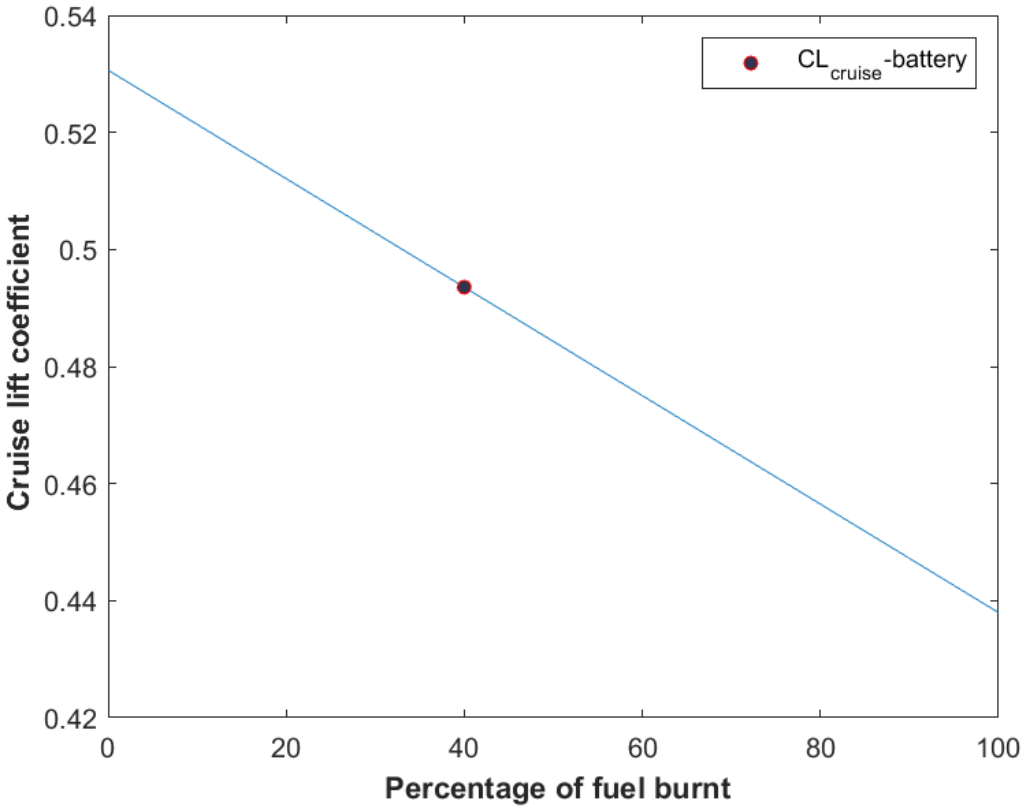

Figure 6.1 Selection of design cruise lift coefficient

The airfoil selected will be studied for sweep effect, taper ratio and the tail down load to trim (Roskam, *Airplane Design: Part II*, 2018). The process is crucial, as it will provide a preliminary prediction of whether the wing can provide the necessary lift during all the segments of flight. A factor of 1.05 $C_{L_{max}}$ is considered for accounting the tail down load to trim since the medium-range hybrid business is expected to be moderately short-coupled i.e., tail arm to the MAC of the wing is 2.94 . To account for the taper ratio, the coefficient of lift is mathematically expressed as:

$$C_{L_{max_W}} = 0.95(C_{Lmax_{root}} + C_{Lmax_{tip}})/2 \tag{6.8}$$

The sweep angle and the thickness ratio have an effect on the critical Mach number. The mission requirement demands a high-speed cruise with a Mach of 0.75 at 40000ft. The swept wing postpones the drag divergence Mach number. A quarter chord sweep angle of 25^o is chosen for the preliminary sizing, based on the historic data that relates the sweep angle and

the Mach number (Raymer, 2012). While high thickness to chord ratios provide the sufficient lift coefficient, they are not aerodynamically efficient at high speeds as the Mach number on the surface of the wing might reach the drag divergence Mach number disrupting the lift produced. As a result, a supercritical airfoil (NASA SC (2)-0612) with a thickness to chord ratio of 12% for the root. For the tip airfoil, the airfoil is chosen with coefficient of lift lesser than the coefficient of the lift of the airfoil at the root. The wing tip airfoil is often thinner than the root airfoil. The lift coefficient of the thinner airfoil is always lesser than the thick airfoil. As the tip airfoil is more prone to stalling, the airfoil chosen is (NASA SC (2)-0610 with the less thickness to chord ratio than the root but provides the required design lift coefficient. The airfoil also has better stalling characteristics and the stall angle at the maximum lift coefficient is around 12^o. The difference in the thickness between the tip and root foil provides the aerodynamic twist. Employing twist in the wing, averts tip stall before the root stall, by means of modifying the lift distribution over the wing. The supercritical airfoil provides high lift coefficient and is suitable for high Mach number design. The supercritical airfoil has very good stall property with the stall angles in the range 12^o – 16^o range. The following are the criteria used to select an airfoil for a wing:

- airfoil with the high maximum lift coefficient, minimum drag coefficient
- airfoil with the higher lift-to-drag ratio and high lift curve slope
- airfoil with the proper stall quality i.e. gradual loss of lift in the stall region (Raymer,2012)

The characteristics of the supercritical airfoils chosen for the wing are shown in the figure below:

- Root airfoil (NASA SC (2) – 0612)

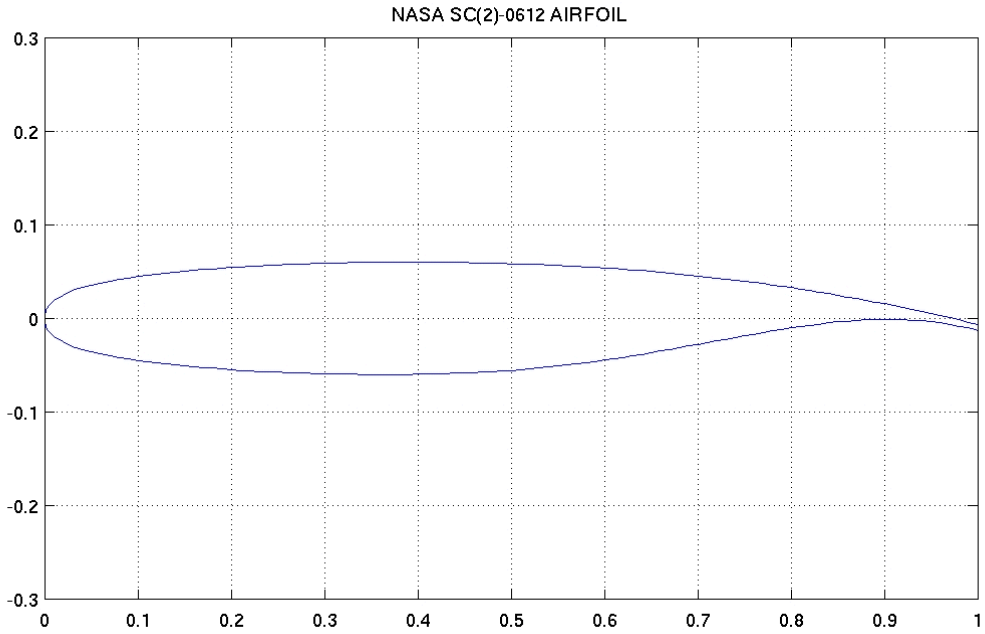

Figure 6.2 NASA SC (2) – 0612 (UIUC Airfoil Coordinates Database NASA SC (2)- 0612, n.d.)

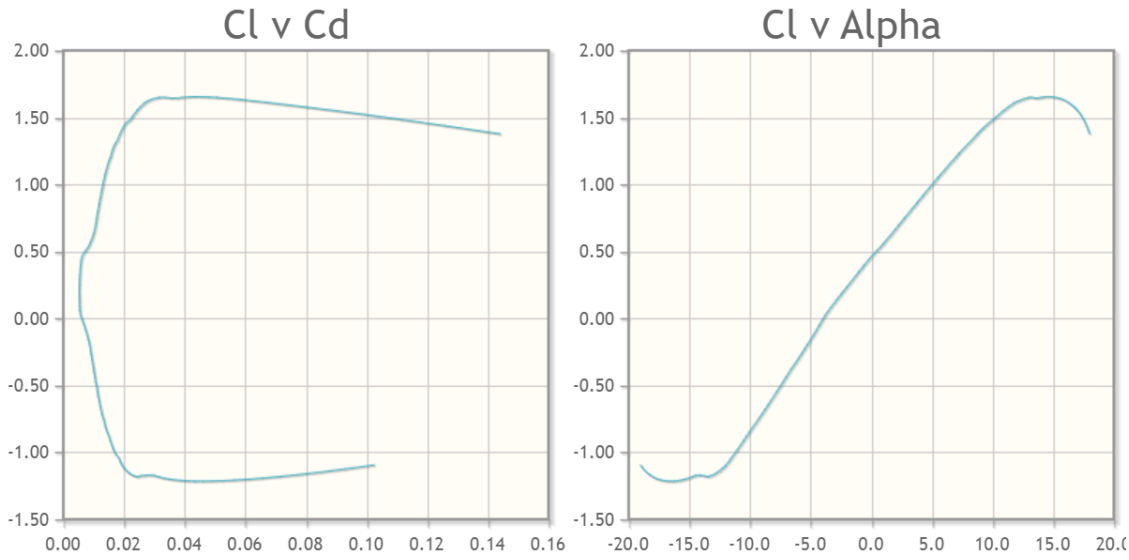

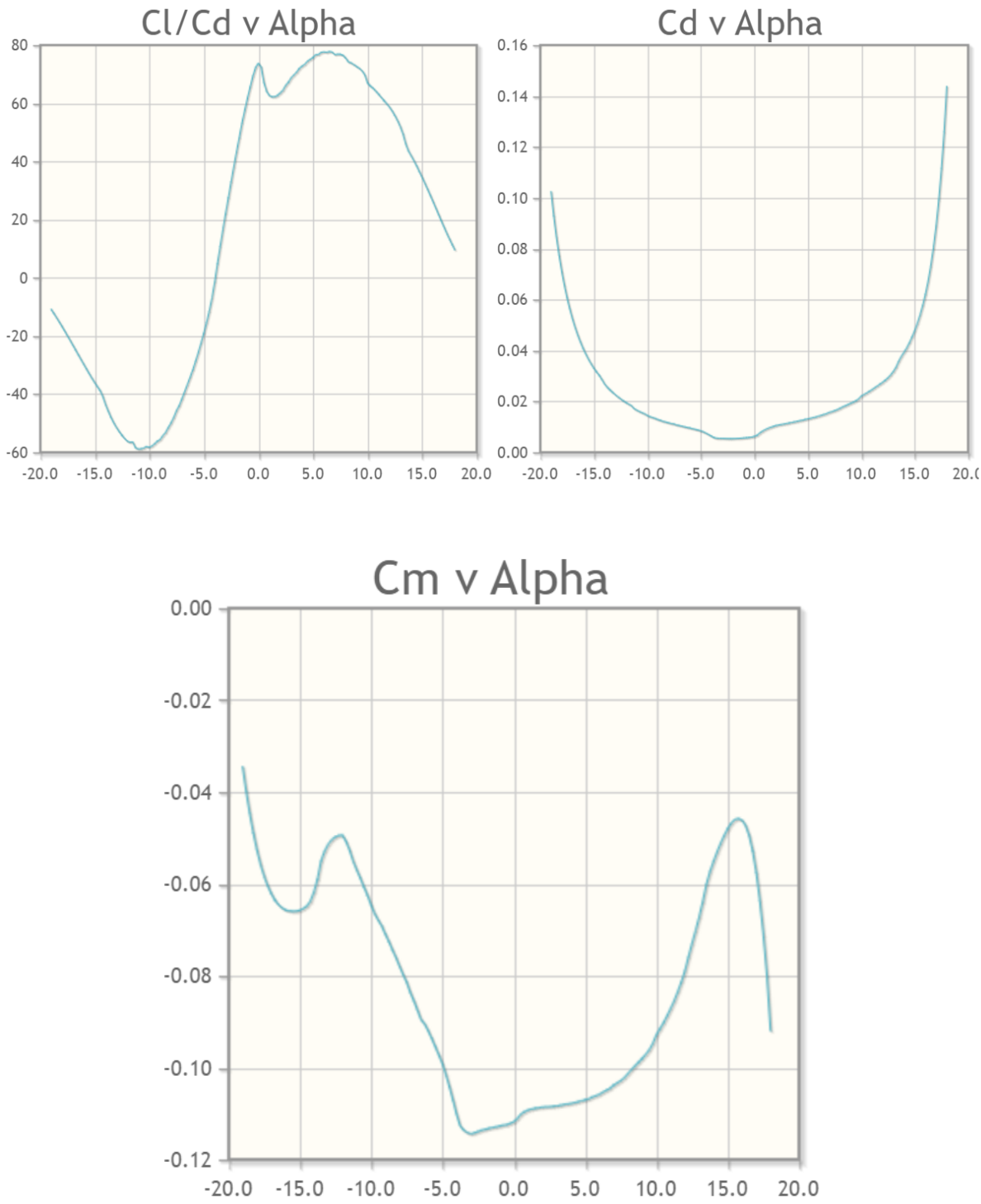

Figure 6.3 Characteristics of NASA SC (2) -0612 (Airfoil NASA SC (2)- 0612, n.d.)

- Tip airfoil (NASA SC (2)- 0610)

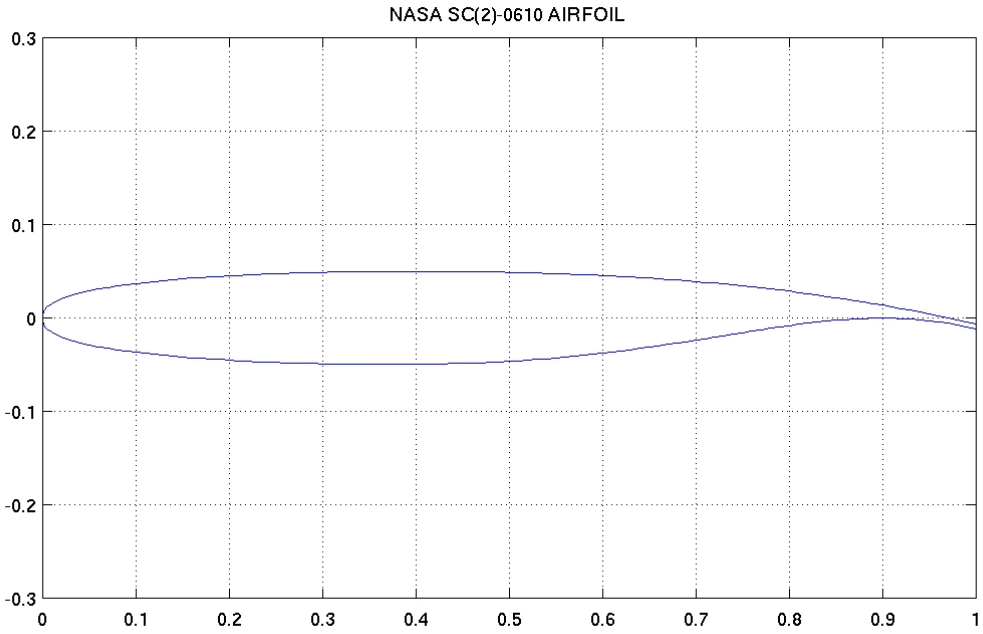

Figure 6.4 NASA SC (2) – 0610 (UIUC Airfoil Coordinates Database NASA SC (2)- 0610, n.d.)

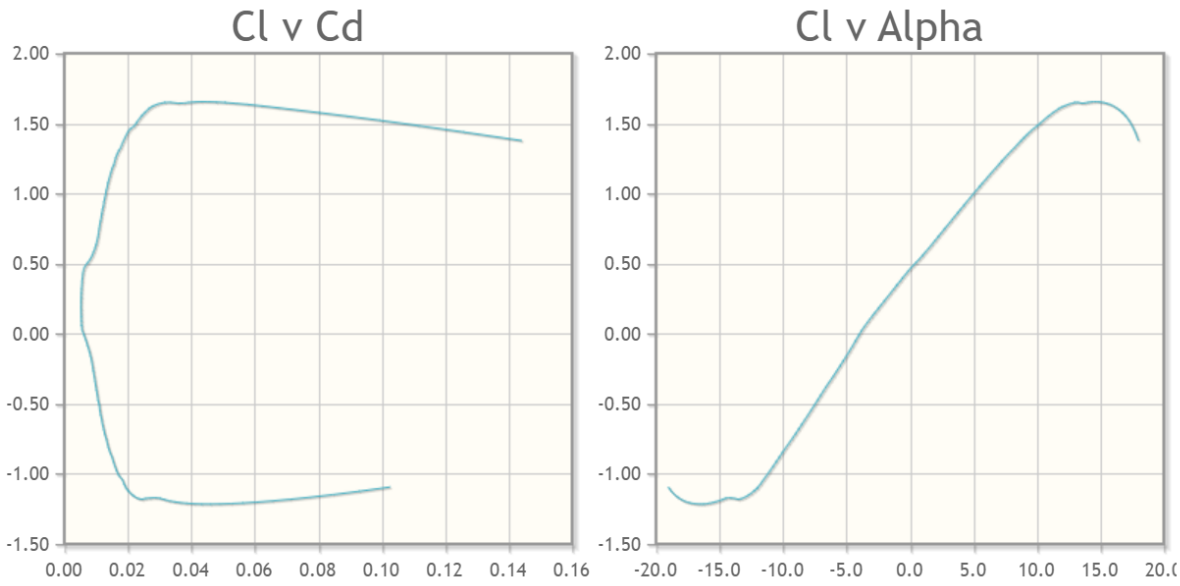

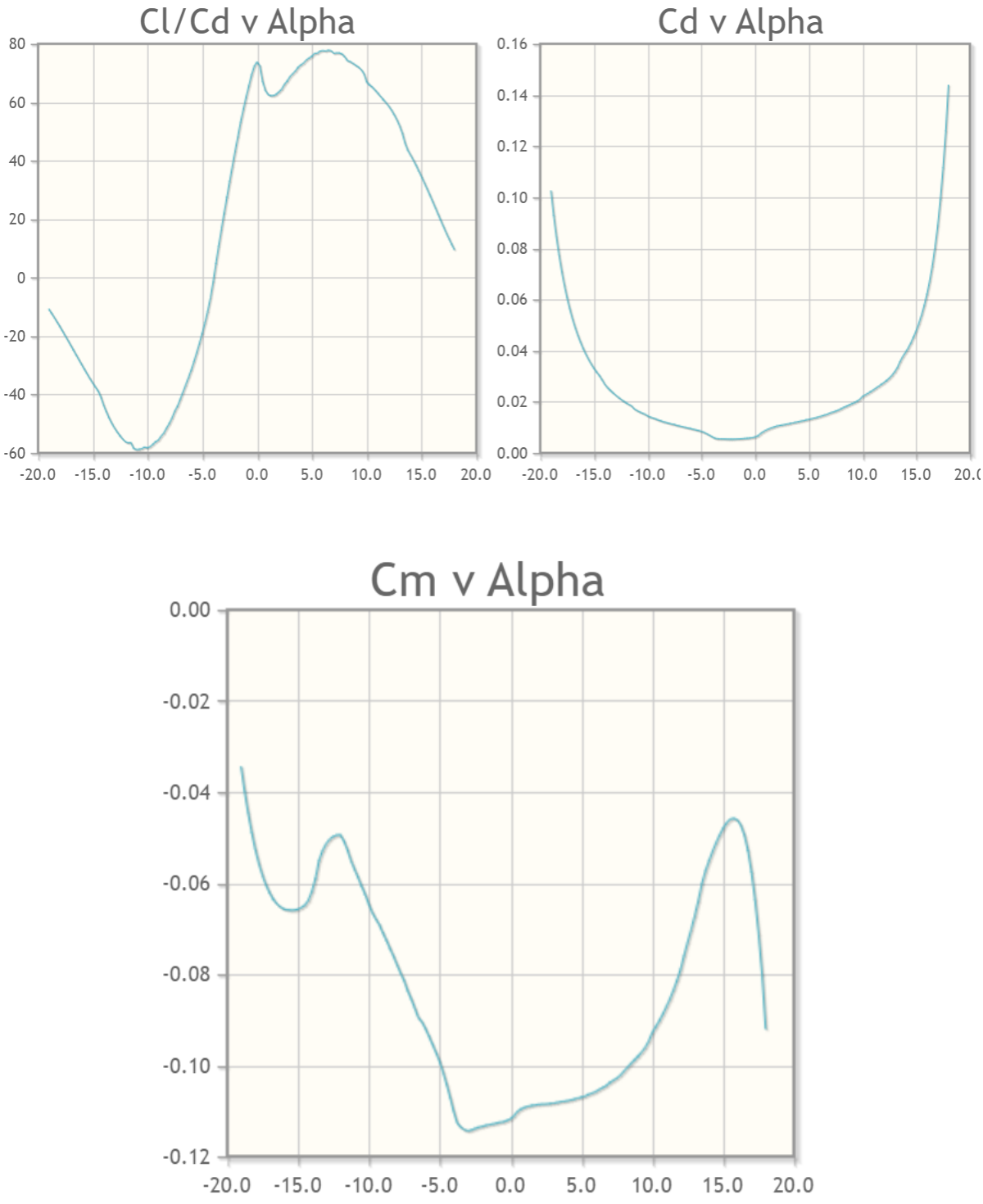

Figure 6.5 Characteristics of NASA SC (2) 0610 (Airfoil NASA SC (2)- 0610, n.d.)

The sweep modifies the lift distribution over the wing, and so the coefficient of lift for the swept wing is computed using the following relation: (Roskam, *Airplane Design: Part II*, 2018):

$$C_{L_{max_W}}(unswept) = C_{L_{max_W}}(Swept)/\cos(\Lambda_{1/4}) \quad (6.9)$$

Table 6.1 Lift- coefficient (Wing and Airfoil)

Lift coefficient	Value
Design lift coefficient $C_{L_{cr}}$	0.494
Lift-coefficient Root $C_{L_{max\_root}}$	1.7
Lift-coefficient Root $C_{L_{max\_tip}}$	1.55
Airfoil Lift coefficient $C_{L_{max\_airfoil}}$	1.543
Lift coefficient (swept wing) $C_{L_{max\_swept}}$	1.399

The maximum coefficient of lift for the swept wing is 1.399 which is less than the maximum coefficient of lift for clean required i.e., 1.4. The error percentage is 0.07%, which is within the 5% error percentage and so the wing will not be redesigned.

6.3 High-lift device design

In the performance sizing, it was identified that the take-off segment requires a C_L of 2.1 and the landing segment requires a C_L of 2.6 to meet the required take-off and landing distance for a wing loading of 376 kg/m^2. The high lift device provides additional lift during take-off and landing. During the take-off and landing, the airspeed is very low compared with cruising speed, and so the wing must produce more lift. The high lift device tends to change pressure distribution over the wing. The incremental lift coefficient for the take-off and landing are determined using the following relations: (Roskam, *Airplane Design: Part II*, 2018).

Take-off: $\Delta C_{LmaxTO} = 1.05(C_{LmaxTo} - C_{Lmax})$ (6.10)

Landing: $\Delta C_{LmaxL} = 1.05(C_{LmaxL} - C_{Lmax})$ (6.11)

The maximum incremental lift coefficient for take-off and landing are obtained as $\Delta C_{LmaxTO} = 0.42$ and $\Delta C_{LmaxL} = 1.26$. From the incremental lift coefficient required, the flap incremental coefficient is computed using the relation:

$$\Delta Clmax = \Delta CLmax((S/S_{wf})k_{\Lambda} \quad (6.12)$$

$$k_{\Lambda} = (1 - 0.08(cos_{\Lambda/4})^2)(cos_{\Lambda/4})^{3/4} \quad (6.13)$$

The flap chord to the wing chord ratio is selected based on the section lift coefficient and the flap incremental lift coefficient for S_{wf} /. The effect of the flap chord ration and the type of flap on k_{Λ} is shown in the figure below: (Roskam, *Airplane Design: Part II*, 2018)

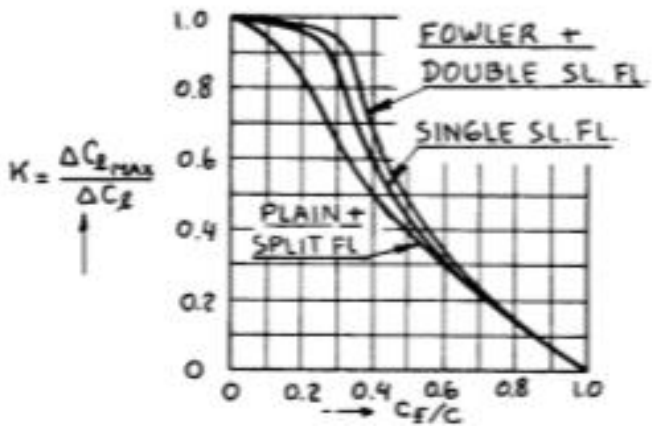

Figure 6.6 Effect of flap chord ratio and flap type on k (Roskam, *Airplane Design: Part II*, 2018)

The incremental section lift coefficient for the take-off and landing are $\Delta \text{Clmax}_{TO} = 1.22$ and $\Delta \text{Clmax}_{L} = 3.64$. Using the figure 6.3, the flap chord ratio for k =0.9 and the fowler flap type is $C_f/C = 0.35$. The take-off and landing flap deflection (δ_f) are computed with the following relation (Roskam, *Airplane Design: Part II*, 2018):

$$\Delta C_l = C_{l_{\alpha_f}} \delta_f \alpha_{\delta_f} \quad (6.14)$$

The parameter α_{δ_f} is the section lift flap effectiveness parameter. It is obtained as 0.57. The flap deflection depends on the section lift flap effectiveness as well as the flap chord to the wing chord ratio. The flapped lift section lift coefficient is given by:

$$C_{l_{\alpha_f}} = C_{l_\alpha}\left(1 + \frac{C_f}{C}\right) \tag{6.15}$$

The flap section lift coefficient is calculated as 8.4823. Using the equations above, the take-off flap deflection and the landing flap deflection are calculated as 16^0 and 48^0 respectively. The wing does not require additional leading-edge flaps for the take-off and landing.

6.4 Control surface sizing

The primary lateral control surfaces on the wing provide lateral stability to the aircraft. The differential aileron provides the rolling motion by means of generating asymmetric pressure distribution on the wing, when deflected upwards or downwards. In the preliminary sizing of the wing, a certain amount of area is allocated for placing the control surface. A preliminary estimate of the lateral control surface is obtained using the data comprising the location and size of the aileron for the transport jet category (Roskam, *Airplane Design: Part II*, 2018). The span wise location and chord-wise location on the wing are obtained from the reference. The location and the surface area of the aileron will be optimized based on the rolling stability and control requirement. For the preliminary estimate, it is assumed that outboard aileron is sufficient and based on the roll requirement inboard aileron could be added as well. The spanwise and chord wise location of the outboard aileron chosen from the data are as follows:

- Outboard aileron starting location: 0.74 (b/2)
- Outboard aileron ending location: 0.94 (b/2)
- Outboard aileron chord location: 0.20 C_w – 0.26 C_w

Type	Wing Area S ft²	Wing Span b ft	Vert. Tail Area S_v ft²	S_r/S_v	x_v ft	$\bar{V}_v$	Rudder Chord root/tip $fr.c_v$	S_a/S	Inb'd Ail. Span in/out fr.b/2	Inb'd Ail. Chord in/out $fr.c_w$
BOEING										
727-200	1,700	108	422	0.16	47.4	0.110	.29/.28	0.034	.38/.46	.17/.24
737-200	980	93.0	233	0.24	40.7	0.100	.25/.22	0.024	none	none
737-300	1,117	94.8	239	0.31	45.7	0.100	.26/.50	0.021	none	none
747-200B	5,500	196	830	0.30	102	0.079	0.30	0.040	.38/.44	.17/.25
747-SP	5,500	196	885	0.27	69.5	0.057	.31/.34	0.040	.38/.44	.17/.25
757-200	1,951	125	384	0.34	54.2	0.086	.35/.33	0.027	none	none
767-200	3,050	156	497	0.35	64.6	0.067	.33/.36	0.041	.31/.40	.23/.20
McDONNELL-DOUGLAS										
DC-9 S80	1,270	108	168	0.39	50.5	0.062	.49/.46	0.030	none	none
DC-9-50	1,001	93.4	161	0.41	46.2	0.079	.45/.44	0.038	none	none
DC-10-30	3,958	165	605	0.18	64.6	0.060	0.35	0.047	.32/.39	.20/.25
AIRBUS										
A300-B4	2,799	147	487	0.30	79.5	0.094	.35/.36	0.049	.29/.39	.23/.27
A310	2,357	144	487	0.35	68.5	0.098	.33/.35	0.027	.32/.40	.23/.27
Lockheed L1011 -500	3,541	164	550	0.23	58.2	0.055	.29/.26	0.051	.40/.49	.22/.23
Fokker F-28 -4000	850	82.3	157	0.16	37.9	0.085	.29/.31	0.034	none	none
Rombac/British Aerospace 1-11 495	1,031	93.5	117	0.28	31.6	0.038	.39/.37	0.030	none	none
British Aerospace										
146-200	832	86.4	224	0.44	38.9	0.12	0.29	0.046	none	none
Tu-154	2,169	123	341	0.27	43.9	0.055	0.37	0.036	none	none

Figure 6.7 Jet transport: Aileron and spoiler data (Roskam, *Airplane Design: Part II*, 2018)

Type	Outb'd Ail. Span in/out fr.b/2	Outb'd Ail. Chord in/out $fr.c_w$	Inb'd Spoiler Span Loc. in/out fr.b/2	Inb'd Spoiler Chord in/out $fr.c_w$	Inb'd Spoiler Hinge Loc. in/out $fr.c_w$	Outb'd Spoiler Span Loc. in/out $fr.c_w$	Outb'd Spoiler Chord in/out $fr.c_w$	Outb'd Spoiler Hinge Loc. in/out $fr.c_w$
BOEING								
727-200	.76/.93	.23/.30	.14/.37	.09/.14	.79/.69	.48/.72	.16/.20	.65/.63
737-200	.74/.94	.20/.28	.40/.66	.14/.18	.66/.67	none	none	none
737-300	.72/.91	.23/.30	.38/.64	0.14	.64/.70	none	none	none
747-200B	.70/.95	.11/.17	.46/.67	.12/.16	0.71	none	none	none
747-SP	.70/.95	.11/.17	.46/.67	.12/.16	0.71	none	none	none
757-200	.76/.97	.22/.36	.41/.74	.12/.13	.73/.69	none	none	none
767-200	.76/.98	.16/.15	.16/.31	.09/.11	.85/.78	.44/.67	.12/.17	.74/.71
McDONNELL-DOUGLAS								
DC-9 S80	.64/.85	.31/.36	.35/.60	.10/.08	.69/.65	none	none	none
DC-9-50	.78/.95	.30/.35	.35/.60	.10/.08	.69/.65	none	none	none
DC-10-30	.75/.93	.29/.27	.17/.30	.05/.06	.78/.74	.43/.72	.11/.16	.75/.70
AIRBUS								
A300-B4	.83/.99	.32/.30	.57/.79	.16/.22	.73/.72	none	none	none
A310	none	none	.62/.83	.16/.22	.69/.66	none	none	none
Lockheed L1011 -500	.77/.98	.26/.22	.13/.39	.08/.12	.82/.73	.50/.74	.14/.14	.67/.67
Fokker F-28 -4000	.66/.91	.29/.28	no lateral control spoilers					
Rombac/British Aerospace 1-11 495	.72/.92	0.26	.37/.68	.06/.11	.68/.63	none	none	none
British Aerospace								
146-200	.78/1.0	.33/.31	.14/.70	.22/.27	.76/.68	none	none	none
Tu-154	.76/.98	.34/.27	.43/.70	.14/.20	.62/.60	none	none	none

Figure 6.8 Jet transport: Aileron and spoiler data (Roskam, *Airplane Design: Part II*, 2018)

One of the secondary control surfaces is the spoiler, which is usually placed on top of the wings. The spoiler reduces the lift component of the wing in a controlled manner by spoiling the streamline flow over the aircraft wing. As a result, it is used to slow an aircraft or make the aircraft descend. It increases the descent rate without increasing the speed of the aircraft. It can

also be used for rolling the aircraft by means of operating only one of the two spoilers, thereby creating differential pressure along the lateral axis and allows the aircraft to roll. For the preliminary sizing, the spanwise and chordwise location of the spoiler are obtained from the aileron and spoiler data:

- spoiler outboard span location = 0.5 (b/2) – 0.66 (b/2)
- location of the hinge: 0.66 Cw
- outboard spoiler chord location = 0.14 Cw – 0.18 Cw

6.5 Wing layout and parameters

The top view of the wing/ planform is shown in the figure below.

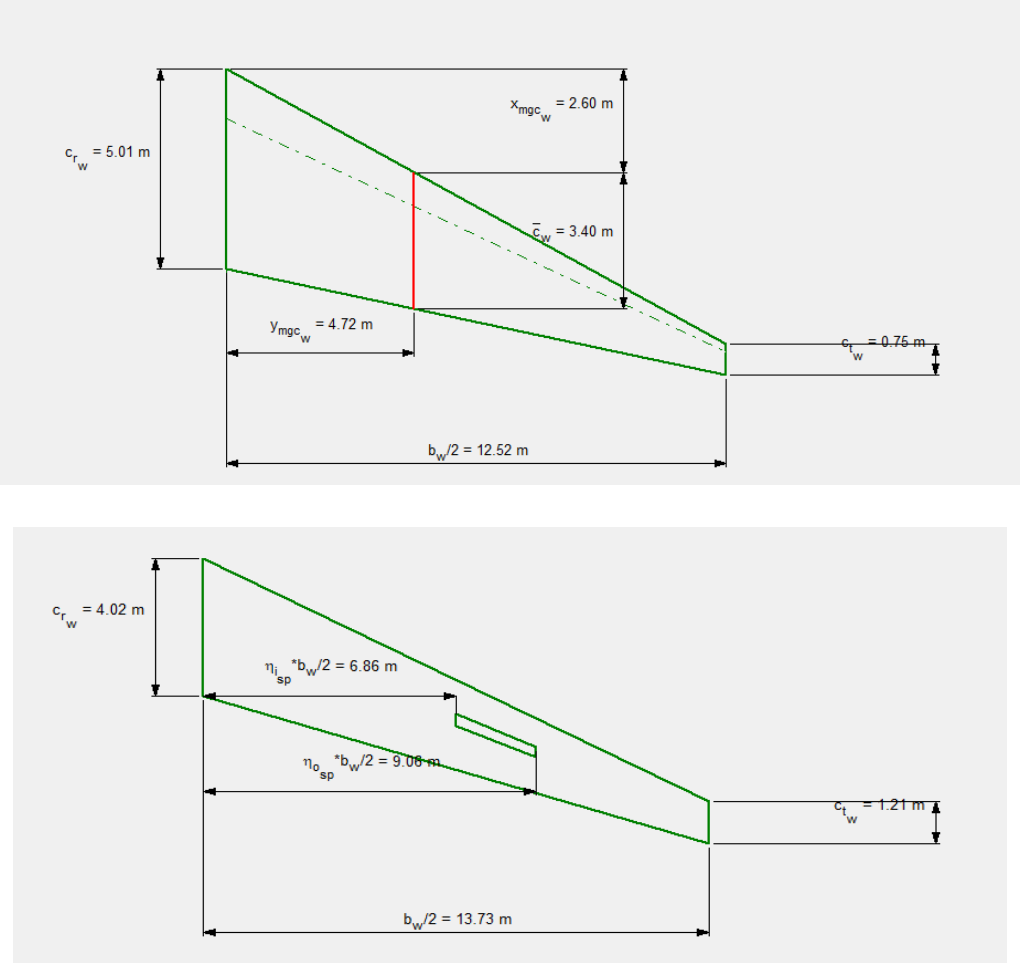

Figure 6.9 Wing and control surface layout

Table 6.2 Wing parameters

Parameter	Value
Wing area S	72.12 m^2
Wing Aspect Ratio	8.7
Wingspan b	25.05 m
Root chord Cr	5 m
Tip chord Ct	0.75 m
Taper ratio	0.15
Sweep angle	25^o
Mean Aerodynamic chord	3.4 m
Dihedral angle	^{2o}
Thickness to chord ratio (Root, tip)	12%, 10%
Root airfoil	NASA SC (2) 0612
Tip airfoil	NASA SC (2) 0610
High lift device type	Trailing edge fowler flap
Take-off flap deflection	16^o
Landing flap deflection	48^o
Flap chord ratio	0.35
Flap area ratio	0.4

The wing is positioned at a distance of 8.05 m from the nose of the fuselage. The isometric view of the wing and fuselage is shown in the figure below.

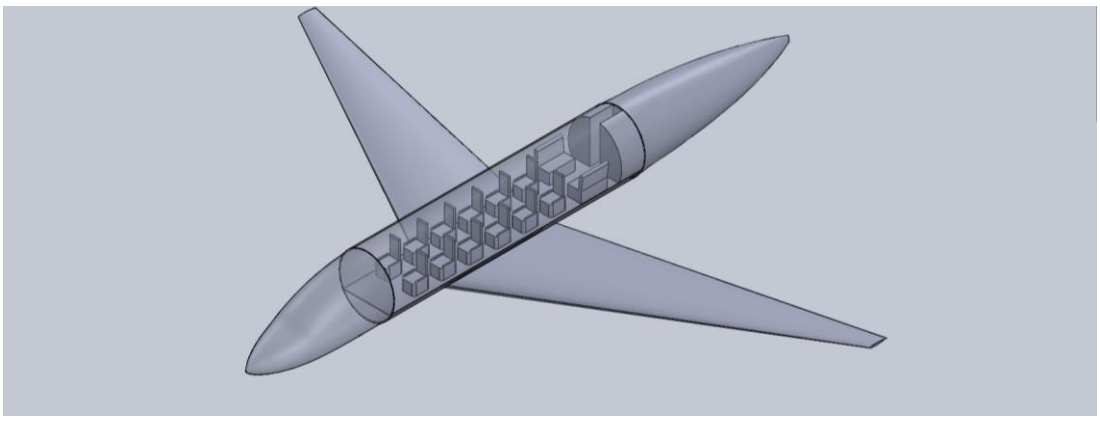

Figure 6.10 Wing + fuselage of the medium range hybrid business jet

6.6 Preliminary battery sizing and fuel tank sizing

The wing carries batteries for propulsion. It avert the dangers of placing the batteries and fuel in the immediate vicinity, the fuselage is stored in the aircraft belly. A rough layout of wing with batteries is also presented in the CAD diagram below. The lithium oxygen batteries are in development and so the battery size and volume are currently unavailable. A rough calculation is carried out using the lithium-ion battery pack developed by Pipistrel for electric propulsion (Pipistrel aircraft PB345V124E-L battery pack, n.d.).

Table 6.3 Battery sizing

Parameters	**Pipistrel PB345V124E-L**	**Hybrid business jet**
Battery type	Li-ion	Li-O_2
Nominal voltage	345 V	
Battery weight	72 kg	8013 kg
Nominal Energy capacity	30 Ah	
Dimension	546 X 265 X 375 mm	

The specific energy density (SED) for the lithium-oxygen (Li-O_2) battery is assumed as 1750 Wh/kg. The SED for the Lithium-ion is computed by multiplying the nominal energy capacity and nominal voltage and dividing it by the battery weight which will result in a SED for the Lithium-ion battery as 143.75 Wh/kg. The SED value of Li-O_2 is 12 times greater than the calculated value of SED for the battery pack. Thus, for a given volume, the lithium-oxygen battery could hold 12 times the energy of a corresponding lithium-ion battery. For the hybrid business jet, the total energy provided by the Li-O_2 battery is 14022750 Wh (Specific energy density multiplied by the net weight of the battery). The energy stored in the lithium-ion battery volume of 0.054 m3 (546 X 265 X 375 mm) is 10350 Wh. With the lithium-oxygen battery possible energy storable in volume of 0.054 m^3 volume of 124200 Wh. For energy of 14022750

Wh, the total battery volume required is 6.1 m^3. The rough layout is prepared with the battery dimensions of:

Table 6.4 Approximate estimation of battery dimension

Cell	Dimension (L x W x H) m	Volume (m^3)
Cell 1	1.85 x 2.5 x 0.3	1.39
Cell 2	1.8 x 2.78 x 0.2	1
Cell 3	1.75 x 3 x 0.1	0.53
Cell 4	1.7 x 2 x 0.04	0.136
		3.05 (One side of the wing)

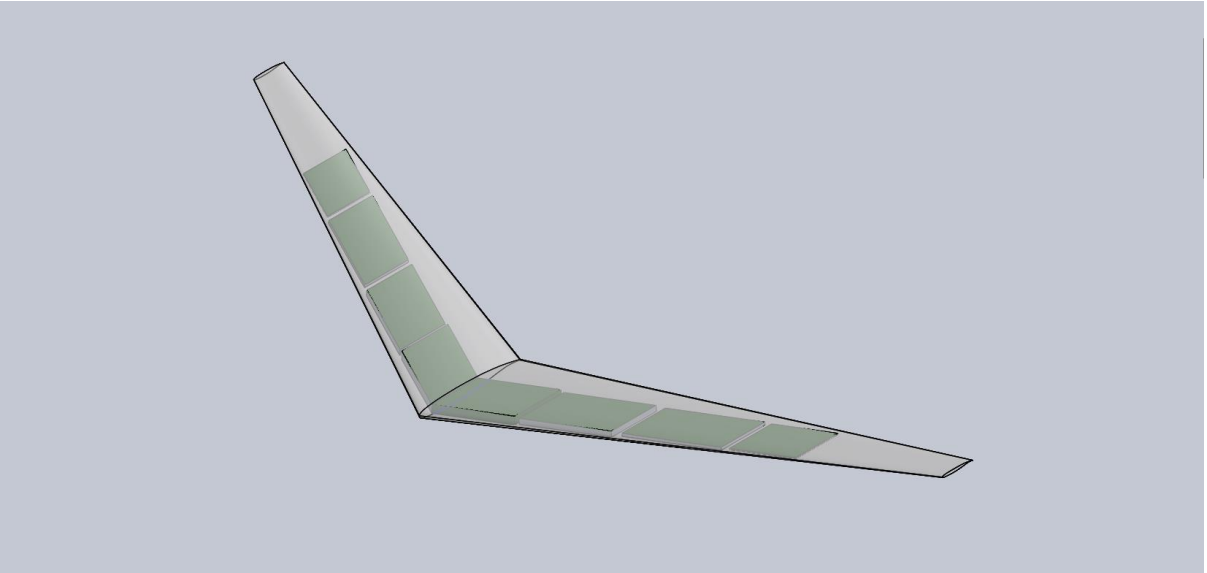

Figure 6.11 Preliminary battery layout on the MRHBJT wing

The total fuel required for the mission is 5084 kg. The aircraft will have three fuel tanks on the forward and aft of fuselage and tail cone. The density of jet A-1 fuel at 15^0 c is 808 kg/m^3 (Jet fuel properties, 2021). The total volume required to store the required fuel is 6.29 m^3. The forward tank has a volume of 3.21 which could store up to 2600 kg of fuel. The aft tank has a volume of 2.84 with a capacity of 2300 kg of fuel. The remaining 184 kg of fuel will be stored in the tail cone. The rough battery and fuel layout are prepared to do a preliminary verification of the volume available for storing these components. The fuselage and wing have the required volume for storage. The volume and space required for other subsystem will be carried out in the detailed sizing. The wing and fuselage have good capacity to hold battery and

fuel and so the wing will not be redesigned in this preliminary sizing. The rough sketch of fuel tank is shown in the figure below.

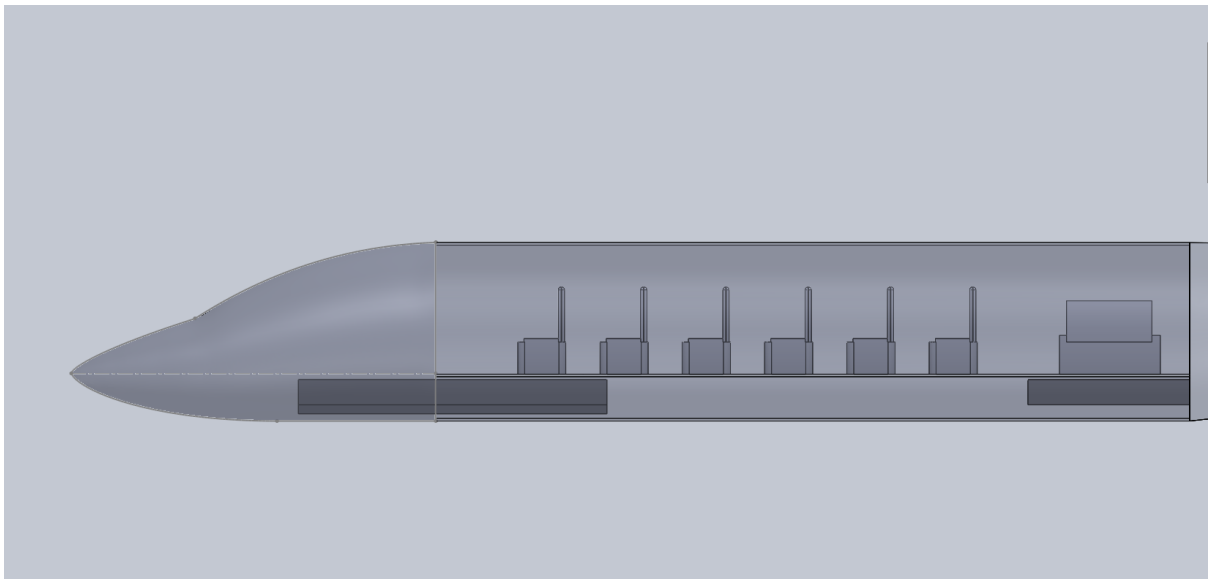

Figure 6.12 Rough sketch of fuel tanks in the fuselage

6.7 Discussion and Conclusion

The wing has been designed with sufficient volume to hold the batteries. The layout of the batteries in the wing is prepared with rough estimation. The lithium-oxygen battery is in the development stage and so, if the actual size of battery is available, the battery volume could be thoroughly estimated which might change the layout of battery on the wing. Furthermore, the structural members of the wing such as spar location and airfoil location along the span could alter the layout of batteries. Besides, the heat generated from the battery pack is another factor that could modify the spacing between cells. In summary, detailed thermal analysis of the battery system and wing design is required to predict the accurate cell dimensions and layout on the wing.

7. Design of the Empennage and the control surfaces

7.1 Introduction

The empennage in a conventional aircraft has a horizontal tail and a vertical tail. The proposed configuration is a T-tail with the horizontal tail placed on the vertical tail. A T-tail lifts the horizontal tail clear of the propwash and downwash from the wing. It allows the use of engine mounted pods in the rear portion of the fuselage (Raymer,2012).. The control surface on the horizontal tail and vertical tail controls the aircraft in the longitudinal and directional axis. The empennage is designed using the methodology followed in the wing design.

7.2 Disposition of the empennage

The empennage stabilizes the destabilizing effects from components that lie ahead of the center of gravity and so, the disposition of empennage is a crucial task. There are two factors that are taken into consideration in the empennage design:

- Weight of the aircraft
- Skin friction drag

To minimize the effect of drag and weight, it is desirable to design empennage with a small area. While a small surface area is ideal from the structural and aerodynamic standpoint, it might not be able to satisfy the stability and control requirement. This issue is generally resolved by positioning the empennage with a long moment arm from the center of gravity. The restoring moment depend on the force generated from the surface and the perpendicular distance. The horizontal and vertical tail arm chosen based on the data available in the reference (Roskam, *Airplane Design: Part II*, 2018).

$$l_h or\ X_h = 10\ m$$

$$l_v or\ X_v = 8m$$

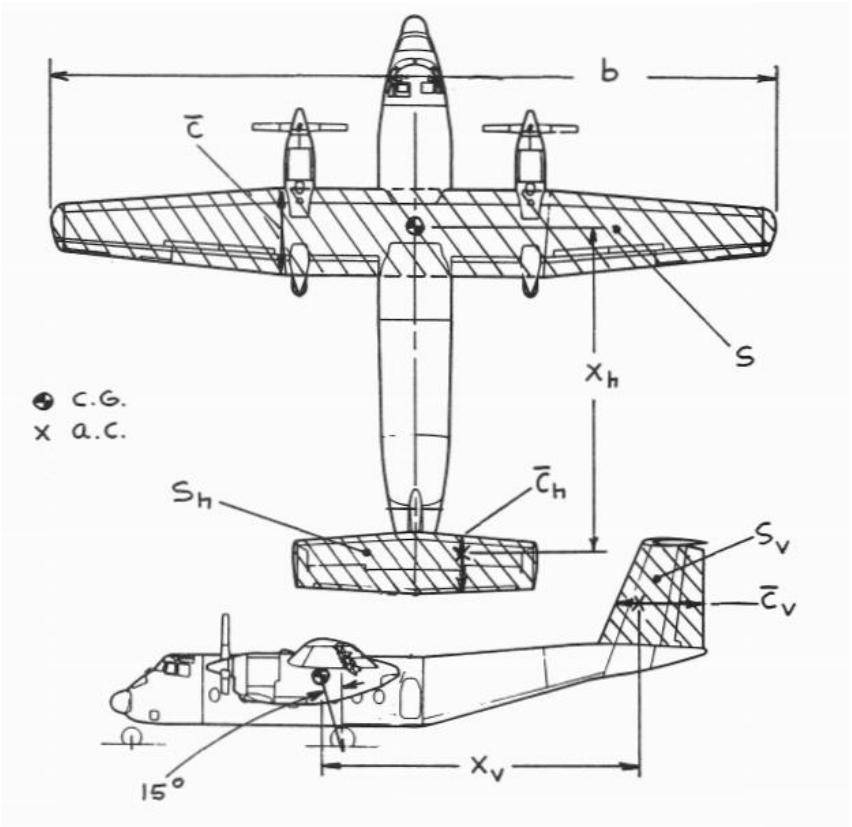

Figure 7.1 Horizontal and vertical tail arm (Roskam, *Airplane Design: Part II*, 2018)

Type	Wing Area S ft^2	Wing mgc $\bar{c}$ ft	Wing Airfoil root/tip NACA*	Hor. Tail Area S_h ft^2	S_e/S_h	x_h ft	$\bar{V}_h$	Elevator Chord root/tip $fr.c_h$
DASSAULT-BREGUET								
Falcon 10	259	6.71	NA	72.7	0.20	16.5	0.69	.31/.29
Falcon 20	440	9.33	NA	122	0.22	21.9	0.65	.28/.31
Falcon 50	495	9.31	NA	144	0.23	21.7	0.68	.31/.34
CESSNA CITATION								
500	260	6.44	23014/23012	70.6	0.29	17.3	0.73	.32/.23
II	323	6.77	NA	73.1	0.36	19.2	0.64	.37/.35
III	312	6.07	NASA Sprcrt	69.6	0.34	26.9	0.99	.39/.42
GATES LEARJET								
24	232	7.03	64A109	54.0	0.26	20.2	0.67	.36/.26
35A	253	7.22	64A109	54.0	0.33	21.9	0.65	.33
55	265	6.88	NA	57.8	0.32	23.8	0.76	.31/.35
Canadair Challenger								
CL-601	450	11.3	NA	105	0.28	32.2	0.67	.30/.31
Aerospatiale								
SN-601	237	5.60	NA	58.9	0.42	16.7	0.74	.40/.44
ISRAEL AIRCRAFT IND.								
Astra	317	5.62	Sigma 2	77.1	0.25	22.8	0.99	.30/.32
Westwind	308	7.58	64A212	70.1	0.25	19.8	0.59	.29/.26
British Aerospace HS								
125-700	353	7.52	NA	100	0.48	19.1	0.72	.37/.67
G.A.-III	935	13.8	NA	184	0.33	35.6	0.51	0.33
MU Diam.I	241	6.23	NA	57.2	0.37	22.4	0.85	0.37

* Unless otherwise indicated.

Figure 7.2 Horizontal tail data – Business jets (Roskam, *Airplane Design: Part II*, 2018)

Type	Wing Area S ft^2	Wing Span b ft	Vert. Tail Area S_v ft^2	S_r/S_v	x_v ft	$\bar{V}_v$	Rudder Chord root/tip fr.c_v	S_a/S	Ail. Span Loc. in/out fr.b/2	Ail. Chord in/out fr.c_w
DASSAULT BREGUET										
Falcon 10	259	42.9	48.9	0.32	14.4	0.063	.34/.49	0.051	.67/.95	.27/.31
Falcon 20	440	53.5	81.8	0.23	18.1	0.063	.25/.39	0.057	.62/.92	0.25
Falcon 50	495	61.9	106	0.12	18.7	0.064	.21/.32	0.049	.68/.97	0.27
CESSNA CITATION										
500	260	43.9	50.9	0.36	18.2	0.081	0.36	0.096	.55/.94	.32/.30
II	323	51.7	53.0	0.34	19.36	0.062	.35/.31	0.078	.56/.89	.32/.30
III	312	53.5	70.2	0.30	20.5	0.086	.37/.38	NA*	.70/.86	.21/.17
GATES LEARJET										
24	232	35.6	38.4	0.17	16.6	0.077	.23/.22	0.050	.63/.89	.25/.23
35A	253	38.1	38.4	0.17	16.6	0.066	.26/.25	0.066	.55/.79	.30/.27
55	265	43.8	52.4	0.17	19.2	0.086	.26/.25	0.062	.49/.71	0.30
Can.CL601	450	64.3	96.0	0.26	24.9	0.083	.29/.31	0.033	.73/.91	.23/.26
Aerospatiale										
SN-601	237	42.2	45.4	0.30	15.7	0.071	.36/.32	0.033	.68/.91	.22/.20
ISRAEL AIRCRAFT IND.										
Astra	317	52.7	48.3	0.21	22.0	0.064	.33/.32	0.040	.67/.95	.26/.25
Westwind	308	44.8	59.7	0.18	20.1	0.087	.34/.44	0.050	.59/.90	.21/.31
British Aerospace HS										
125-700	353	47.0	63.8	0.22	15.9	0.061	.31/.37	0.084	.66/1.0	.33/.46
G.A. III	935	77.8	159	0.24	26.9	0.059	0.28	0.038	.66/.86	.24/.27
MU Diam.I	241	43.4	55.9	0.25	17.4	0.093	.33/.28	0.012	.86/.94	.20/.22

* Also uses spoilers for lateral control

Figure 7.3 Vertical tail data – Business jets (Roskam, *Airplane Design: Part II*, 2018)

7.3 Size of the empennage

The size of the horizontal and vertical tail is determined using the tail volume coefficient. The horizontal and vertical tail volume coefficients are expressed using the following relations:

$$\bar{V}_H = \frac{X_H S_H}{\bar{C}_W S} \tag{7.1}$$

$$\bar{V}_V = \frac{X_V S_V}{bS} \tag{7.2}$$

The tail volume coefficients are chosen as $\bar{V}_H = 0.77$ and $\bar{V}_V = 0.07$. This results in a surface area of horizontal and vertical tail as 18.89 m^2 and 15.8 m^2 respectively. In the stability and control analysis, the typical surface area required to meet the static stability requirement will be calculated. The tail will not be resized if the resulting surface area from the stability and control analysis is within 10% of the surface area obtained from the volume coefficient.

7.4 Geometric parameters for the empennage

The planform design of the horizontal and vertical tail require important geometric parameters such as the aspect ratio, taper ratio, sweep angle, dihedral, and incidence angle etc.

The parameters are selected from the reference data comprising planform parameters for different airplane category (Roskam, *Airplane Design: Part II*, 2018) provided below:

Type	Dihedral Angle, Γ_h deg.	Incidence Angle, i_h deg.	Aspect Ratio, A_h	Sweep Angle, $\Lambda_{c/4_h}$ deg.	Taper Ratio, λ_h
Homebuilts	+5 - -10	0 fixed to variable	1.8 - 4.5	0 - 20	0.29 - 1.0
Single Engine Prop. Driven	0	-5 - 0 or variable	4.0 - 6.3	0 - 10	0.45 - 1.0
Twin Engine Prop Driven	0 - +12	0 fixed to variable	3.7 - 7.7	0 - 17	0.48 - 1.0
Agricultural	0 - +3	0	2.7 - 5.4	0 - 10	0.59 - 1.0
Business Jets	-4 - +9	-3.5 fixed	3.2 - 6.3	0 - 35	0.32 - 0.57
Regional Turbo-Props.	0 - +12	0 - 3 fixed to variable	3.4 - 7.7	0 - 35	0.39 - 1.0
Jet Transports	0 - +11	variable	3.4 - 6.1	18 - 37	0.27 - 0.62
Military Trainers	-11 - +6	0 fixed to	3.0 - 5.1	0 - 30	0.36 - 1.0
Fighters	-23 - +5	0 fixed to variable	2.3 - 5.8	0 - 55	0.16 - 1.0
Mil. Patrol, Bomb and Transports	-5 - +11	0 fixed to variable	1.3 - 6.9	5 - 35	0.31 - 0.8
Flying Boats, Amph. and Float Airplanes	0 - +25	0 fixed	2.2 - 5.1	0 - 17	0.33 - 1.0
Supersonic Cruise Airplanes	-15 - 0	0 fixed to variable	1.8 - 2.6	32 - 60	0.14 - 0.39

Figure 7.4 Horizontal tail planform parameters (Roskam, *Airplane Design: Part II*, 2018)

Type	Dihedral Angle, Γ_v deg.	Incidence Angle, i_v deg.	Aspect Ratio, A_v	Sweep Angle, $\Lambda_{c/4_v}$ deg.	Taper Ratio, λ_v
Homebuilts	90	0	0.4 - 1.4	0 - 47	0.26 - 0.71
Single Engine Prop. Driven	90	0	0.9 - 2.2	12 - 42	0.32 - 0.58
Twin Engine Prop Driven	90	0	0.7 - 1.8	18 - 45	0.33 - 0.74
Agricultural	90	0	0.6 - 1.4	0 - 32	0.43 - 0.74
Business Jets	90	0	0.8 - 1.6	28 - 55	0.30 - 0.74
Regional Turbo-Props.	90	0	0.8 - 1.7	0 - 45	0.32 - 1.0
Jet Transports	90	0	0.7 - 2.0	33 - 53	0.26 - 0.73
Military Trainers	90	0	1.0 - 2.9	0 - 45	0.32 - 0.74
Fighters	75 - 90	0	0.4 - 2.0	9 - 60	0.19 - 0.57
Mil. Patrol, Bomb and Transports	90	0	0.9 - 1.9	0 - 37	0.28 - 1.0
Flying Boats, Amph. and Float Airplanes	90	0	1.2 - 2.4	0 - 32	0.37 - 1.0
Supersonic Cruise Airplanes	75 - 90	0	0.5 - 1.8	37 - 65	0.20 - 0.43

Figure 7.5 Vertical tail planform parameters (Roskam, *Airplane Design: Part II*, 2018)

The vertical tail will have a dihedral angle of 90^0 since any other angle for a typical conventional tail configuration result in unnecessary yaw moment along the directional axis. The choice of dihedral/ anhedral for the horizontal tail is not made at this stage of design and is assumed as 0^0. The aspect ratio and taper ratio for tails are chosen as $AR_H = 6.3$; $\lambda_H = 0.32$ and $AR_V = 1.6$ and $\lambda_V = 0.4$. The sweep angle is chosen higher than the quarter chord sweep angle of wing $\Lambda_H = 29^o$ and $\Lambda_{VT} = 30^o$. The selection of airfoil for the tail depends on two important factors:

- The airfoil must be symmetric.
- The lift curve slope must be as high as possible.

Table 7.1 Tail parameters

Parameter	Horizontal tail	Vertical tail
Moment arm from the CG	10 m	8 m
Tail volume coefficient	0.77	0.07
Surface area	18.89 m^2	15.4 m^2
Aspect Ratio	6.3	1.6
Span	10.5 m	5.02 m
Taper ratio	0.32	0.4
Sweep angle	29	30
Dihedral angle	0	90
Root chord	2.62	4.49 m
Tip chord	0.84	1.79 m
Mean Aerodynamic chord	1.88 m	3.35 m
Thickness to chord ratio (root)	10%	10%
Thickness to chord ratio (tip)	10%	10%
Control surface area ratio	0.3	0.28
Control surface area	5.67 m^2	4 m^2
Airfoil	NACA 64A010	NACA 64A010

The planform of the horizontal and vertical tail are prepared with AAA software:

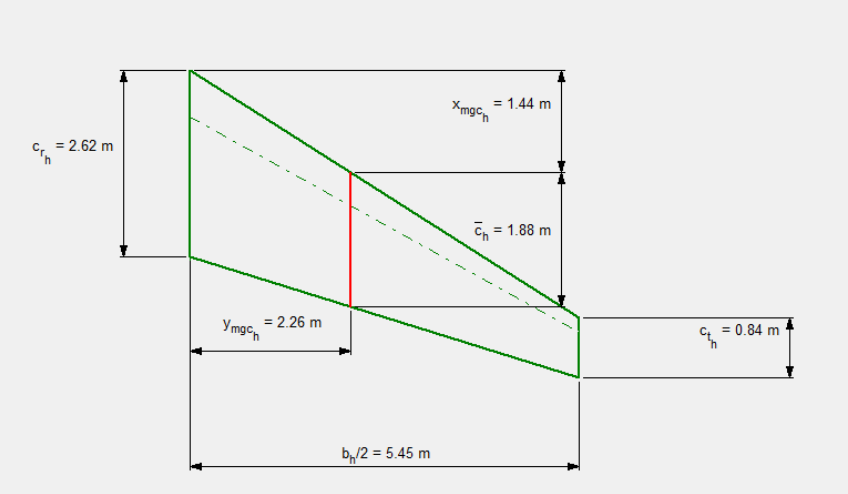

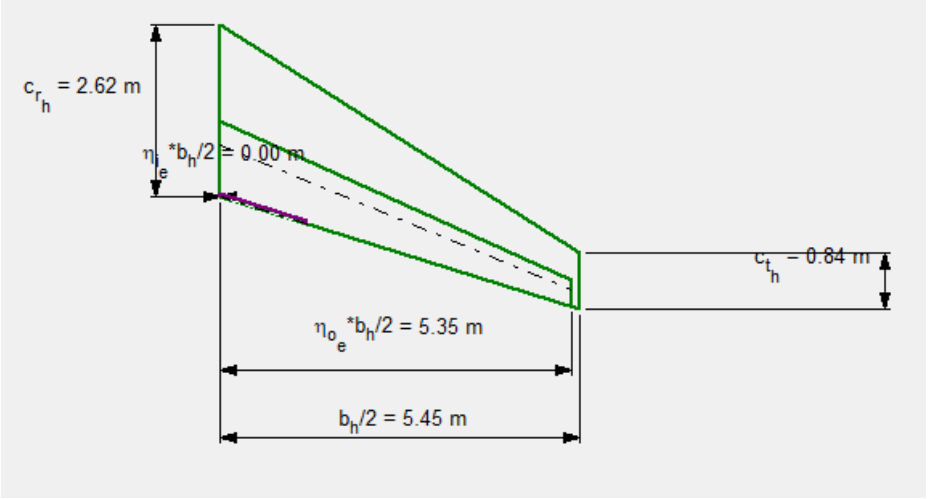

Figure 7.6 Horizontal tail and elevator

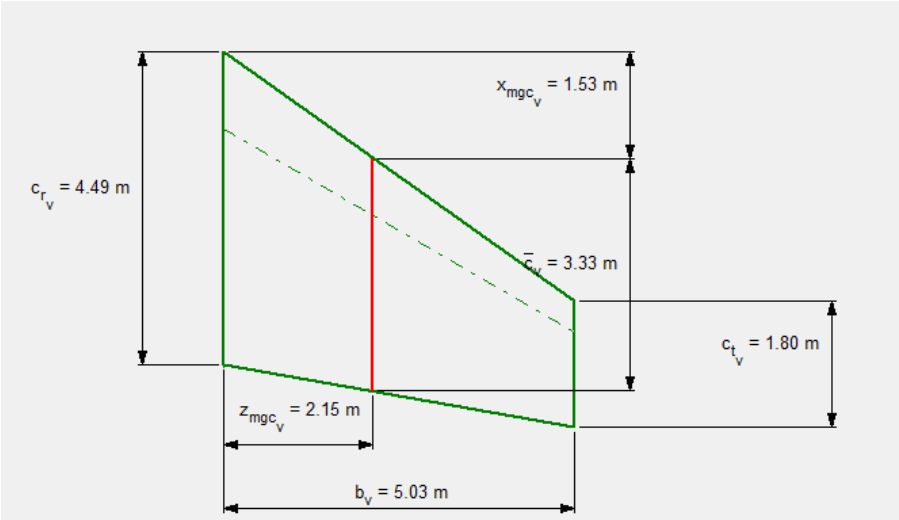

Figure 7.7 Vertical tail

8. Weight and balance Analysis

8.1 Introduction

The weight and balance are analysed to determine whether or not the center of gravity of the proposed configuration is in the right place for different loading scenarios. Furthermore, to position the main landing gear, iterations between the CG and the location of the landing gear has to be carried out to ensure that the main landing gear is placed behind the most aft CG position.

8.2 Estimation of the center of gravity

The location of the centre of gravity of the aircraft depends on the weight and location of CG of individual components. The weight of the structural and fixed equipment components are estimated using component weight fraction for business jet category. The payload and crew weights are available from the mission requirement. The battery weight and fuel weight are obtained from the class I weight sizing and the powerplant weight is obtained from the performance sizing. The structural components are broken down into the following segments:

- fuselage
- wing
- fixed equipment weight
- horizontal and vertical tail
- landing gears (nose and main gear)
- nacelle

The group weight data for the business jet category is obtained from (Roskam, *Airplane Design: Part V,* 2018) is tabulated below:

Table 8.1 Component weight fraction data (Roskam, *Airplane Design: Part V*, 2018)

Type	**Lockheed Jetstar**	**Cessna Citation II**	**Gulfstream American GII**
Wing group	0.092	0.095	0.098
Empennage group	0.029	0.022	0.03
Fuselage group	0.114	0.079	0.092
Nacelle group	0.026	0.016	0.019
Landing gear group	0.035	0.034	0.031
Fixed equipment group	0.165	0.167	0.173
Powerplant group	0.081	0.106	0.106
Empty weight fraction	0.541	0.52	0.55
Design gross weight (kg)	13920	6126	29401

In the class I weight and balance analysis, a preliminary configuration arrangement is made by fixing the locations of component and the center of gravity along the X, Y, Z axis is determined. The aircraft is symmetrical, and the cabin weight is distributed equally on either side of the aircraft in the final fuselage layout prepared. Furthermore, all the components are arranged in a symmetrical way from the center line of the fuselage to avoid unnecessary rolling motion along the lateral axis. The location of CG of major components along the longitudinal axis is estimated using Figure 8.1.

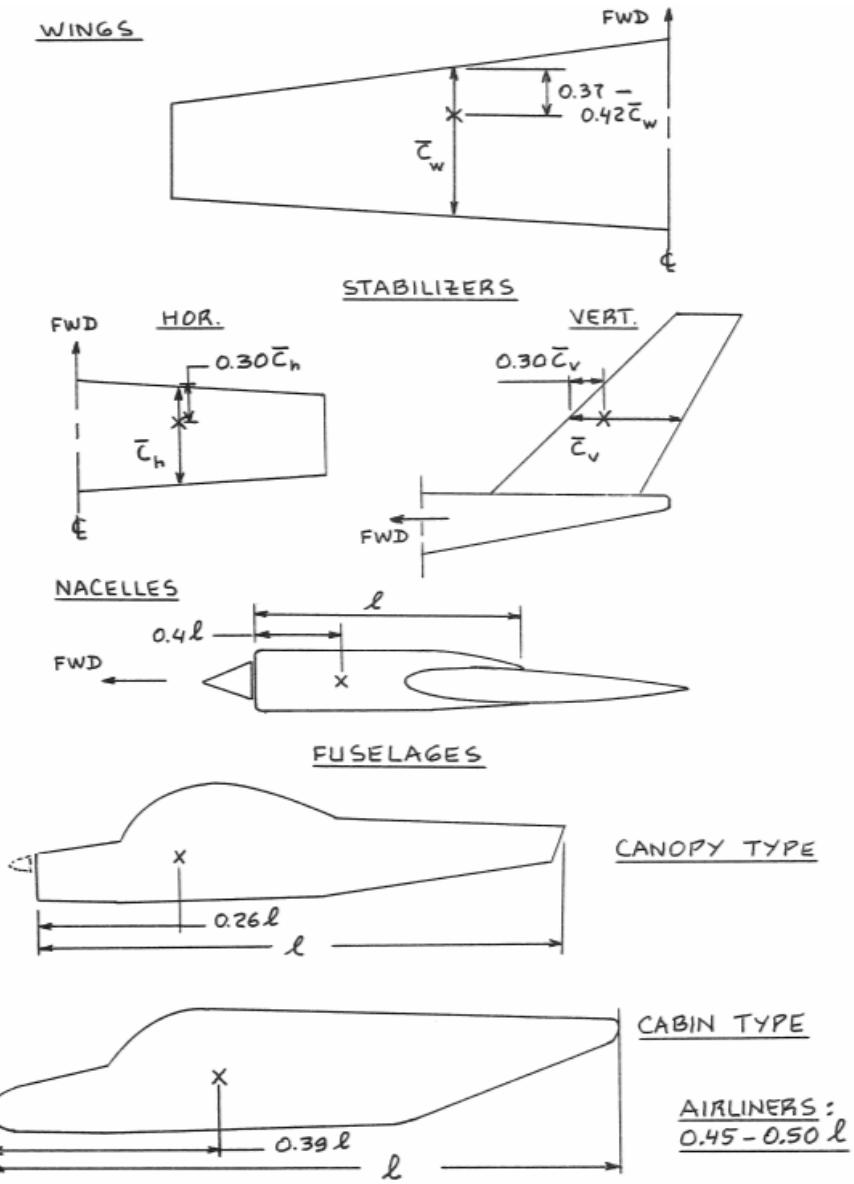

Figure 8.1 Location of CG of major components (Roskam, *Airplane Design: Part II*, 2018)

The location of center of gravity of the fuselage from the nose is assumed to be at a distance of 0.45 times the length of the fuselage. The horizontal location of the wing is 8.05 m from the nose. Through the course of the design, the location of components have been altered multiple times before finalizing, since balancing the weight is an iterative process. The weight of components and the location of CG for the full weight loading scenario is presented in the Table 8.2. The weight of the components are obtained using the weight fraction data in Table 8.1.

Table 8.2 Component weight and center of gravity

Components	**Weight**	**X**	**Wx**	**Y**	**W_Y**	**Z**	**Wz**
Fuselage	2680	10.72	28729.6	0	0	2.4	6432
Wing	2704	11.9	32177.6	0	0	1.5	4056
Horizontal tail	425	22.3	9477.5	0	0	7.6	3230
Vertical tail	375	20.3	7612.5	0	0	6.1	2287.5
Nacelle	580	19.5	11310	0	0	2.75	1595
Powerplant	2200	19.5	42900	0	0	2.75	6050
Fixed equipment	4800	9.3	44640	0	0	2.1	10080
Nose gear	200	2.3	460	0	0	0.9	180
Main gear	700	12.9	9030	0	0	0.9	630
fuel tank (fuselage - forward)	2600	5	13000	0	0	1.86	4836
Fuel tank (aft)	2300	17	39100	0	0	1.86	4278
fuel tank (tail cone)	184	22	4048	0	0	2.4	441.6
Battery	8013	11.5	92149.5	0	0	1.5	12019.5
Fuel tank (center)	0	0	0	0	0	0	0
Crew(cockpit)	159	3	477	0	0	2.22	352.98
Passenger + cabin crew	954	10.8	10303.2	0	0	2.2	2098.8
Baggage	238	19	4522	0	0	2.2	523.6
Total weight (kg)	29112	Wx	349936.9			Wz	59090.98
		X_{CG}(m)	12.02	Y_{CG} (m)	0	Z_{CG} (m)	2.03

The center of gravity along X axis is computed by taking the nose as reference and for the Z axis a rough assumption based on the landing gear height is made as the reference i.e. the reference point is the ground. The center of gravity travels during the flight based on the amount of fuel burnt and the payload capacity. The hybrid business jet has fuel tanks in the forward and aft of the fuselage as well as the tail cone. The CG shift due to the presence and absence of fuel in the tanks are estimated. It was observed in the class I weight and balance analysis that landing the aircraft with fuel in the aft tank alone is not desirable and the fuel filling order could begin with front tank or the tail cone tank, but the aft tank should be filled only in the end. The CG travel for different loading scenarios is conducted and the values of the CG along the X axis are presented in the table below.

Table 8.3 Location of CG for different loading scenario

Loading Scenario	**W_{TO} (kg)**	**CGx (m)**	**Fraction of $\bar{C}$**
Full weight	29112	12.020	0.405
No payload + No Cabin crew	27920	12.003	0.400
Empty weight + Fuel weight + Battery weight	27761	12.057	0.416
Empty weight + Half-fuel weight (Forward tank) + Tail tank + Payload	25462	11.943	0.383
Empty weight + battery weight	22677	12.281	0.482
Empty weight + Battery weight+ Fuel weight (Tail cone) + payload	24212	12.301	0.488
Empty weight + Battery weight + Fuel weight + Half payload	28533	12.016	0.404
Empty weight + Battery weight + Half-fuel (All tanks) + Payload	26570	12.136	0.440
Empty Weight + Battery Weight + Fuel Weight (5%) + Payload	24282	12.151	0.444
Empty Weight + Battery Weight + Fuel Weight (5%) + Half-Payload	23703	12.220	0.464

The most forward center of gravity is when the forward tank is half full and the tail tank is full which is at 0.38 $\bar{c}$ and the most aft CG is for the case with fuel in the tail tank alone which is at 0.488 $\bar{c}$. The CG range in terms of the fuselage station is 0.358 m which is 0.105 $\bar{c}$. The values obtained are consistent with the CG range data for the business jet category which is 0.203 – 0.43 m or 0.10 $\bar{c}$ – 0.21 $\bar{c}$ (Roskam, *Airplane Design: Part II*, 2018). The CG excursion plot with respect to the fuselage station and the mean aerodynamic chord are shown in the following graphs.

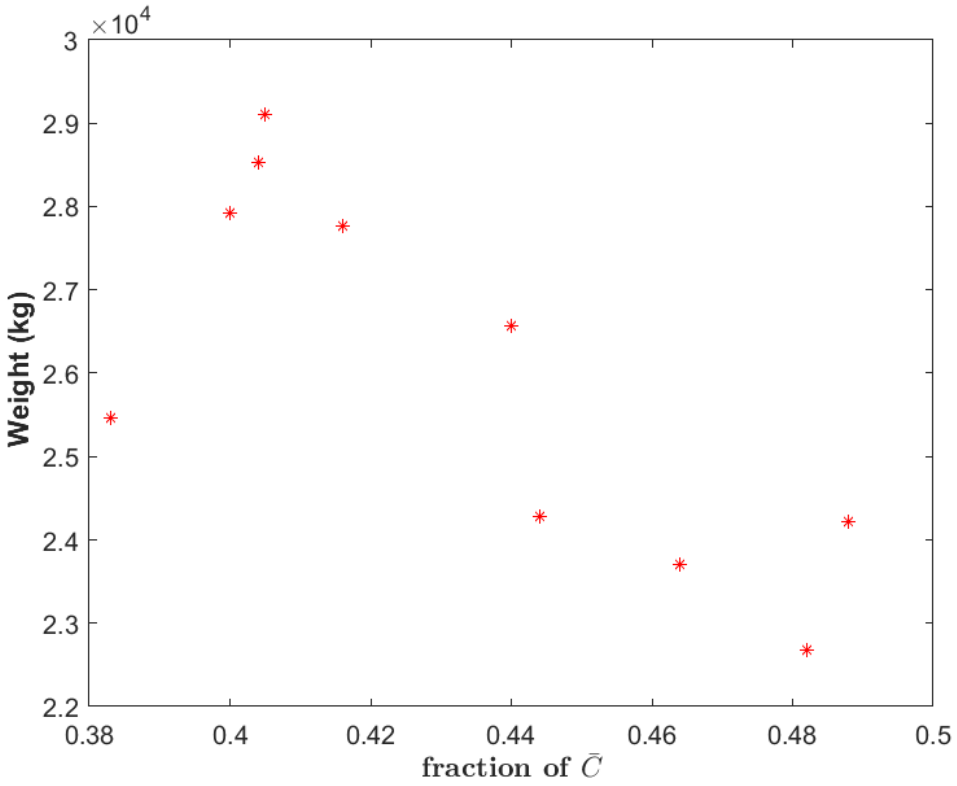

Figure 8.2 CG Excursion plot (Fraction of mean aerodynamic chord)

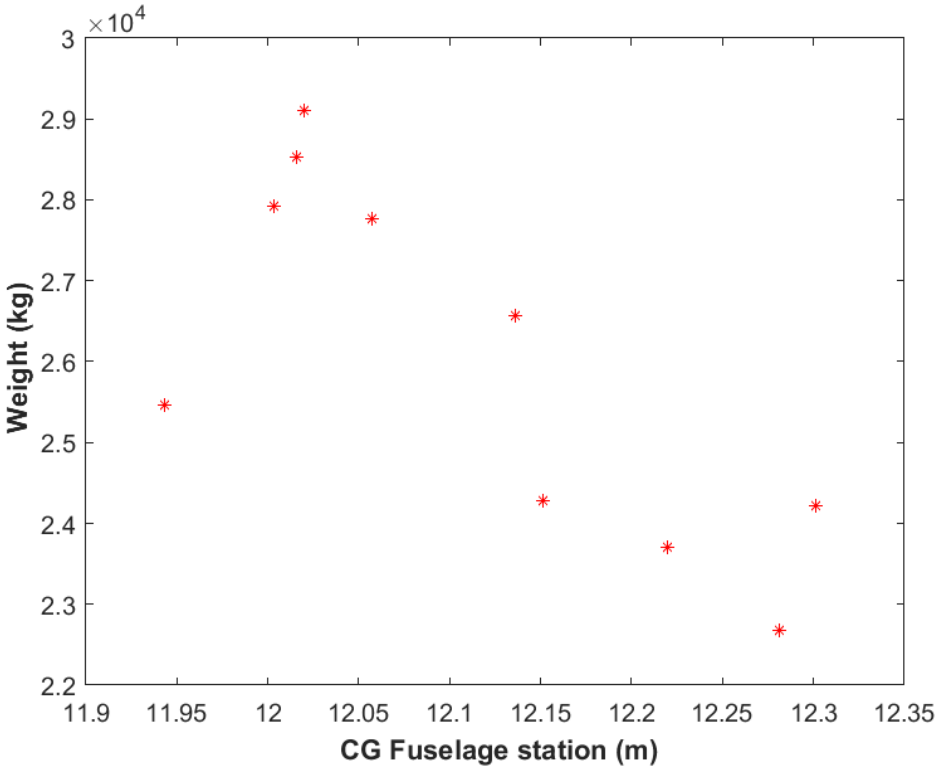

Figure 8.3 CG Excursion plot (Fuselage Station)

9. Landing Gear Design

9.1 Introduction

This chapter presents the Class I landing gear sizing and disposition. The landing gear sizing and the location of the center of gravity are a coupled system; so the gear sizing is an iterative process. Furthermore, the choice of the landing gear system depends on the cruise speed of the aircraft. If the cruise speed is above 150 knots (77 m/s), a fixed landing gear imposes a high drag penalty (Roskam, *Airplane Design: Part II*, 2018). The medium-range hybrid business jet will feature a retractable landing gear system to avoid high-drag penalty from the fixed type landing gear. The configuration of landing gear is chosen as tri-cycle type. The landing gear sizing begins with the rough estimation of the center of gravity by assuming the location of disposition of the landing gear. Once the CG is obtained for different loading scenarios, the geometric criteria such as the tip-over criteria and ground clearance criteria are investigated before fixing the location of the landing gear. If the assumed landing gear does not meet the geometric criteria, iterations will be performed until the requirements are met. The next stage of the sizing is the determination of the following landing gear characteristics:

- number of tires
- size and type of tires
- preliminary disposition of the landing gear
- feasibility of landing gear retraction

9.2 Landing gear design

The disposition of the landing gear depends on the center of gravity and the geometric criteria to avoid tip-over and ensure sufficient ground clearance during take-off, land, taxi segment. Furthermore, the feasibility for retracting the landing gear is investigated to identify the space available in the wing and fuselage for holding the landing gear. The center of gravity

for different loading scenario obtained in the weight and balance analysis will be utilized to decide the disposition of the landing gear. The most forward center of gravity and the most aft aft center of gravity are the main point of interest in designing the landing gear.

9.2.1 Tip-over criteria

The longitudinal tip-over criterion and the lateral tip-over criterion are the two tip-over criteria that are considered in the disposition of the landing gear design (Roskam, *Airplane Design: Part II*, 2018).

The longitudinal tip-over criterion for the tricycle landing gear configuration is that the location of the main landing gear must be behind the aft CG location. Furthermore, a 15^0 angle is required between the bottom of the strut to the aft CG location. The criterion is shown in the figure below (Roskam, *Airplane Design: Part II*, 2018).

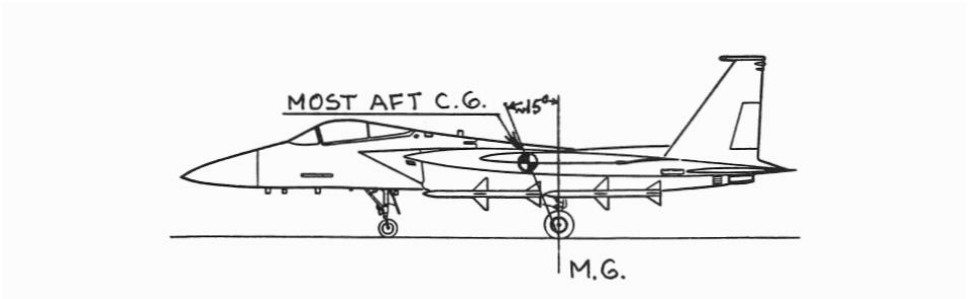

Figure 9.1 Longitudinal tip-over criterion (Roskam, *Airplane Design: Part II*, 2018)

The most aft CG for the aircraft is 12.3 m from the nose of fuselage. The distance between the aft CG and the main landing gear is about 0.6 m. The angle between the aft CG and main landing gear has satisfied the required longitudinal tip over criterion with an angle of 16.14^o which is shown in the Figure 9.2.

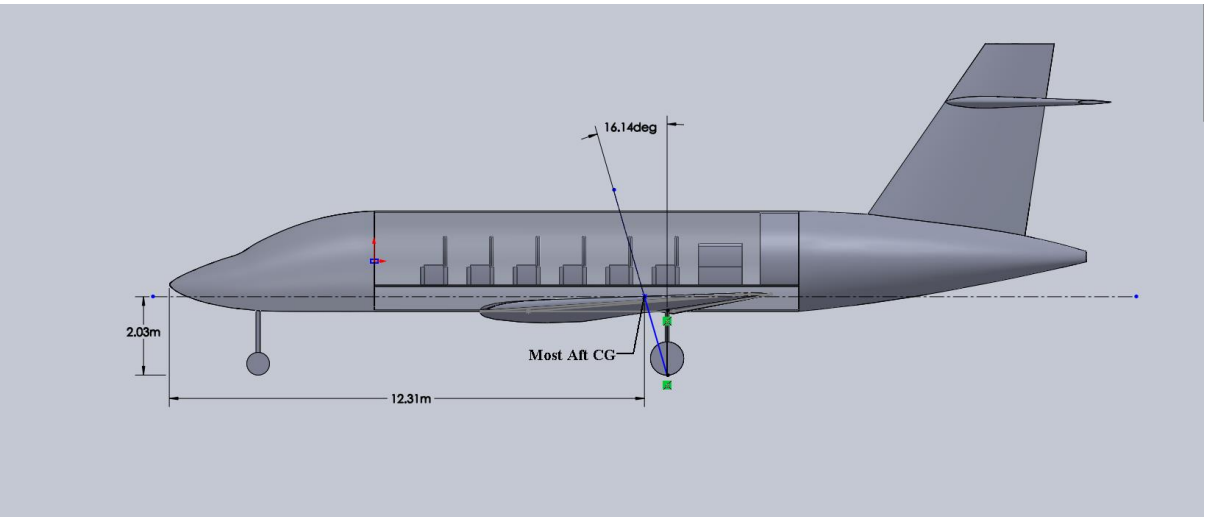

Figure 9.2 Longitudinal tip-over criterion diagram for MRHBJT

The lateral tip over criterion is to ensure that landing gear has enough wheel track and wheelbase to avoid tip over in the lateral direction. The wheel track is the distance between main landing gears and the wheelbase is the distance between the nose gear and main landing gear. This criterion is based on the most forward CG location for the tricycle type landing gear configuration, and it is shown in the figure below (Roskam, *Airplane Design: Part II*, 2018).

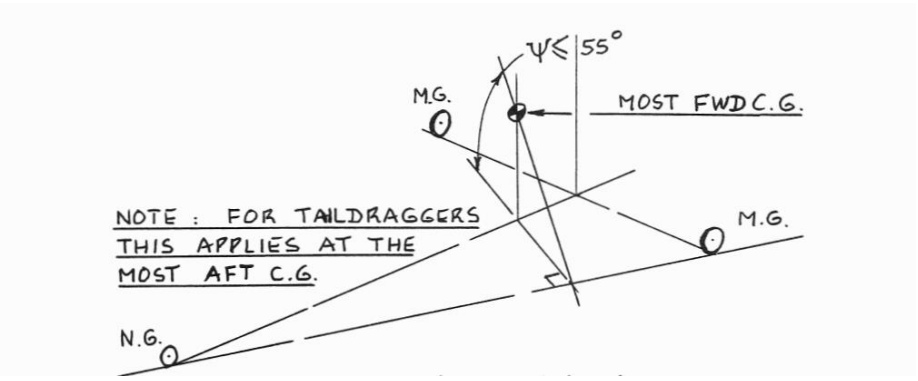

Figure 9.3 Lateral Tip-over criterion (Roskam, *Airplane Design: Part II*, 2018)

The landing gears of the medium-range hybrid business jet has satisfied the lateral-tip over criterion with ψ = 48.21^{o} and is shown in Figure 9.4.

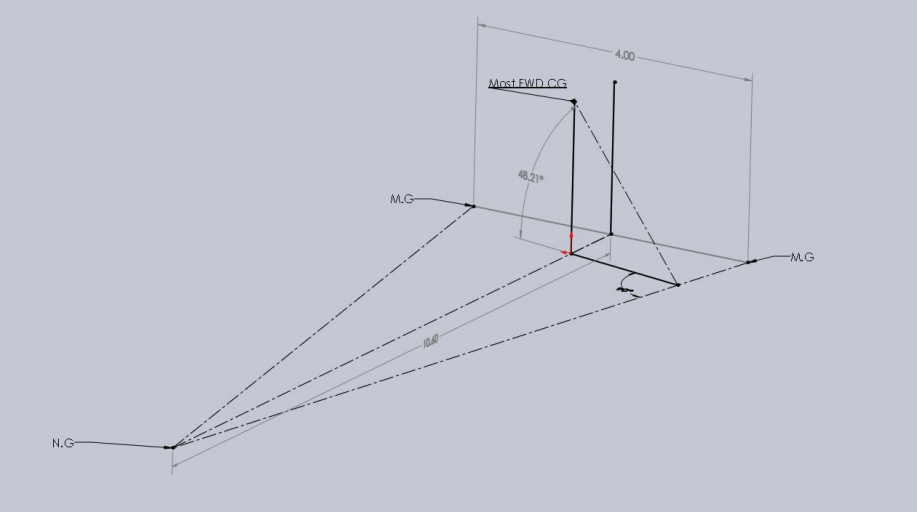

Figure 9.4 Lateral tip-over criterion for the MRHBJT

9.2.2 Ground clearance criteria

The longitudinal ground clearance criterion and the lateral ground clearance criterion are the two ground clearance criteria that are considered in the disposition of the landing gear design (Roskam, *Airplane Design: Part II*, 2018). The following parameters are estimated once the landing gear disposition satisfies the criteria:

- number of main gear and nose gear struts
- length of main gear and nose gear strut

The longitudinal ground clearance criterion states that angle between the tail cone and the wheel should be at least 15° so that the tail has enough ground clearance during take-off. The lateral ground clearance criterion determines the required wheel track to ensure that there is sufficient ground clearance in the lateral direction. The generic ground clearance criteria is shown in the Figure 9.5 and the specific criteria for the hybrid business jet is shown in Figures 9.6 and 9.7.

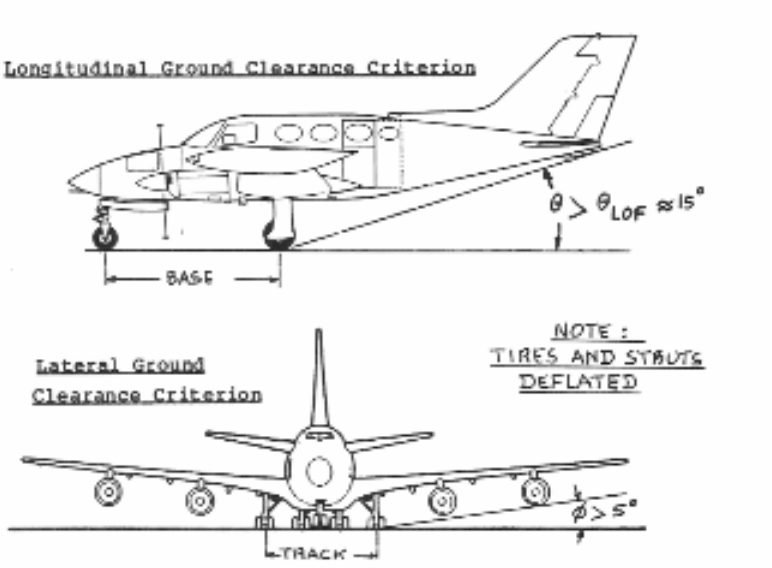

Figure 9.5 Ground clearance criteria (Roskam, *Airplane Design: Part II*, 2018)

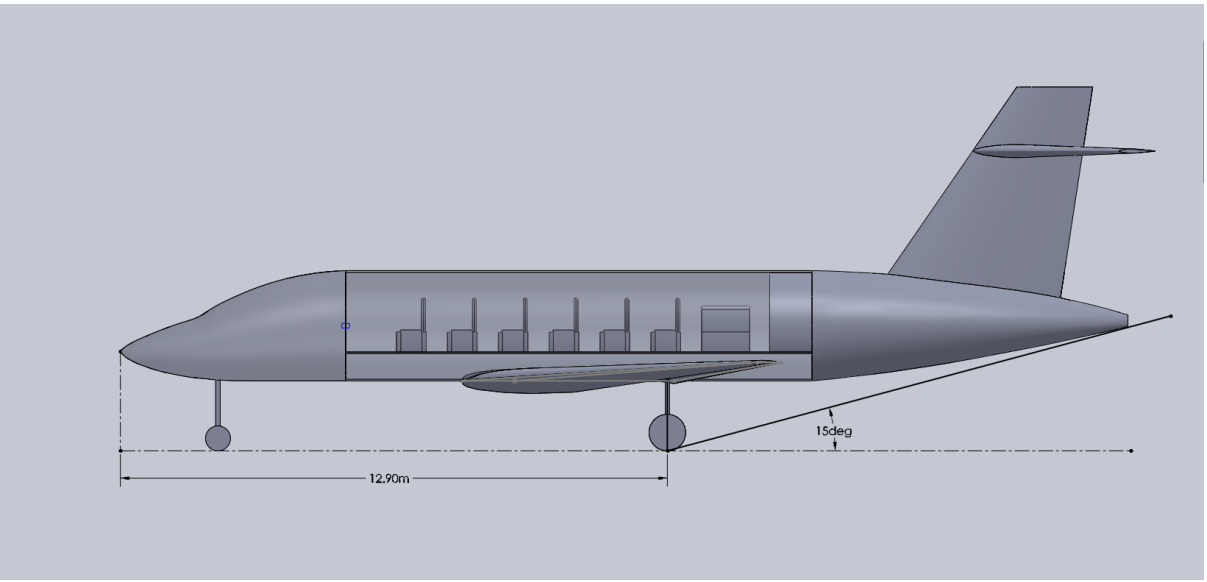

Figure 9.6 Longitudinal ground clearance criterion for MRHBJT

The location of the landing gear at 12.9 m from the nose has satisfied the ground clearance criterion and so the tail cone angle of 6^0 assumed in the fuselage design will not be changed. The medium-range business jet does not have a wing-mounted propeller or nacelle and so the lateral clearance with respect to the wing tip is conducted.

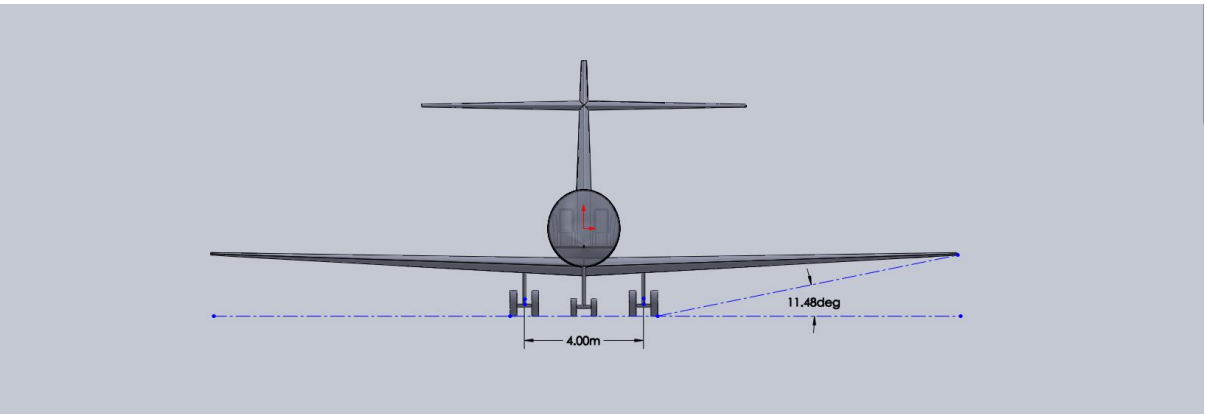

Figure 9.7 Ground clearance criterion for gear placement for MRHBJT

9.2.3 Strut and tire sizing

The amount of static load on the nose and main strut depends on the take-off weight and the location of the landing gear from the CG of the aircraft. The static loading on the nose wheel strut and main wheel strut are computed using the equations given below (Roskam, *Airplane Design: Part II*, 2018):

$$P_n = \frac{W_{TO} l_m}{(l_m + l_n)} \tag{9.1}$$

$$P_m = \frac{W_{TO} l_n}{2(l_m + l_n)} \tag{9.2}$$

The parameters in the equation above is defined in the following figure:

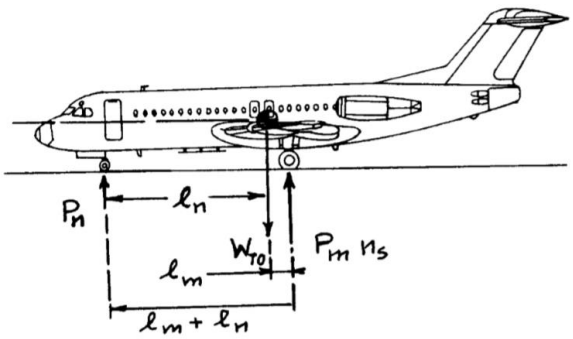

Figure 9.8 Geometry for static load calculation (Roskam, *Airplane Design: Part II*, 2018)

Type	W_{TO}	Main Gear				Nose Gear			
		$D_t x b_t$	$2P_m/W_{TO}$	PSI	n_{mt}	$D_t x b_t$	P_n/W_{TO}	PSI	n_{nt}
	lbs	in.xin.				in.xin.			
Homebuilts	600	13x5	0.80	25	1	9x3.4	0.17	25	1
	1,200	12x5	0.78	45	1	12x5	0.22	45	1
	3,300	16x6	0.87	45	1	16x6	0.13	45	1
Single Engine	1,600	15x6	0.80	18	1	15x5	0.20	28	1
Prop. Driven	2,400	17x6	0.84	19	1	12.5x5	0.16	22	1
	3,800	16.5x6	0.84	55	1	14x5	0.16	49	1
Twin Engine	5,000	16x6	0.83	55	1	16x6	0.17	40	1
Prop. Driven	8,000	22x6.5	0.88	75	1	17x6	0.12	40	1
	12,000	26.6x7	0.84	82	1	19.3x6.6	0.16	82	1
Agricultural	3,000	22x8	0.95	35	1	9x3.5*	0.05*	55*	1*
	7,000	24x8.5	0.92	35	1	12.4x4.5*	0.08*	50*	1*
						*Note: these are tailwheel data			
	10,000	29x7.5	0.85	35	1	25x7	0.15	35	1
Regional Turbo-	12,500	18x5.5	0.89	105	2	22x6.75	0.11	57	1
propeller Driven	21,000	24x7.25	0.90	85	2	18x5.5	0.10	65	2
Airplanes	26,000	36x11	0.92	40	1	20x7.5	0.08	40	1
	44,000	30x9	0.93	107	2	23.4x6.5	0.07	77	2
Business Jets	12,000	22x6.3	0.93	90	1	18x5.7	0.07	120	1
	23,000	27.6x9.3	0.95	155	1	17x5.5	0.05	50	2
	39,000	26x6.6	0.92	208	2	14.5x5.5	0.08	130	2
	68,000	34x9.25	0.93	174	2	21x7.25	0.07	113	2

Figure 9.9 Landing gear wheel data (Roskam, *Airplane Design: Part II*, 2018)

The static load on the nose strut and main strut are computed as 1648 kg and 13732 kg using $l_m = 0.6$ m and $l_n = 10$ m based on the aft center of gravity obtained from the weight and balance analysis. The nose gear takes about 5.6 % of the net loading and the main gear carries 94.4 % of the loading. The main gear has two struts, and the nose gear has one strut. The nose and main gear tire dimensions are obtained from the landing gear wheel data available in the figure above.

Table 9.1 Summary of landing gear sizing for MRHBJT

Wheel base	10.6 m
Wheel track	4 m
Nose gear location	2.3 m (From the nose of fuselage)
Main gear location	12.9 m (From the nose of fuselage)
Static loading on the main strut	13732 kg (Each strut)
Static loading on the nose strut	1648 kg
Nose gear tire dimension (d_t x b_t)	0.53 m x 0.18 m
Main gear tire dimension (d_t x b_t)	0.86 m x 0.23 m

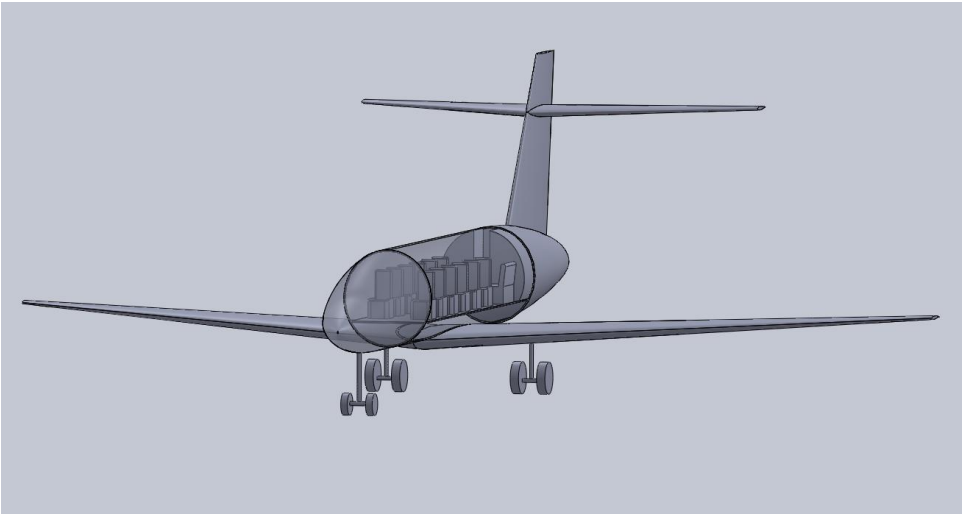

Figure 9.10 Isometric view of hybrid business jet with landing gear disposition

9.3 Discussion

The disposition of the landing gear for the medium-range hybrid business jet has satisfied the required tip-over criteria and ground clearance criteria. The arrangement of components in the weight and balance analysis will not be altered.

10. Stability and Control Analysis

10.1 Introduction

The design and performance of the tail and stabilizer are an integral part of the stability and control of the aircraft. The stability is the tendency of the aircraft to return to its equilibrium position after a disturbance. The controllability of the aircraft is referred to as the vehicle's handling quality to achieve equilibrium and perform manoeuvres for a range of flight speeds and altitudes (Nelson, 1998). The stability of the aircraft is classified into two parts, ie. static and dynamic stability. In this section, the influence of stability and control on the design parameters of the horizontal and vertical tail and the static longitudinal and static directional stability are presented.

10.2 Static longitudinal stability

The ability of the aircraft to develop a restoring moment along the longitudinal axis after a disturbance is the static longitudinal stability. For the static longitudinal stability to exist, the pitching moment curve must be negative and the pitching moment coefficient at zero angle-of attack must be positive (Nelson, 1998). The components that generate pitching moment about the center of gravity are the fuselage, wing, horizontal tail, and the propulsion system. The effect of the thrust line offset on the longitudinal stability for most jet engines is very small (Roskam, *Airplane Design: Part VI*, 2018) and so the contribution from the propulsion system is not considered for the preliminary sizing. In the weight and balance analysis, it was observed that the center of gravity changes during the flight regime. Similarly, the aerodynamic centre of the aircraft travels based on the moment contribution from the components. The important criterion is that the center of gravity should not move past the aerodynamic center for the stability to exist (Nelson, 1998). This is represented as the static margin, which is the distance between the CG and AC of the aircraft as a function of the mean aerodynamic chord. The

medium-range hybrid business jet is designed with de-facto stability i.e., the aircraft will be stable with the aid of feedback augmentation system and the required static margin is 5% (Roskam, *Airplane Design: Part II*, 2018).

$$Static\ margin\ \frac{dC_m}{dC_L} = \frac{X_{cg} - X_{ac}}{\bar{C}} = -0.05 \tag{10.1}$$

The CG travel component is estimated using the weight and balance analysis in which the surface area of the tail is varied. The location of the tail from the nose of the fuselage and the weight of tail are assumed independent of the surface area of the tail.

Another component in the equation 10.1 is the aerodynamic center of the aircraft. The AC leg is calculated using the equations from Roskam (Roskam, *Airplane Design: Part II*, 2018):

$$\bar{X}ac_A = [\bar{X}ac_{wf} + \{C_{L_{\alpha_h}}(1 - (d\varepsilon_h/d\alpha)(S_h/S)\bar{X}ac_h)/\left(C_{L_{\alpha_{wf}}}\right)\}]/F \tag{10.2}$$

$$F = 1 + \{C_{L_{\alpha_h}}(1 - (d\varepsilon_h/d\alpha)(S_h/S))/\left(C_{L_{\alpha_{wf}}}\right)\} \tag{10.3}$$

$$\bar{X}ac_{wf} = \bar{X}ac_w + \Delta\bar{X}ac_f \tag{10.4}$$

where,

$\bar{X}ac_w$ is the aerodynamic centre of the wing as a fraction of MAC and $\Delta\bar{X}ac_f$ is the aerodynamic shift due to the fuselage. It is assumed that AC of the wing is at 25% the Mean Aerodynamic Chord of the wing.

10.2.1 Calculation of the aerodynamic center shift due to the fuselage

In the fuselage design, the mission requirement in terms of the payload and crew capacity were satisfied. In this section, the fuselage contribution to the stability of the aircraft is studied. The fuselage is divided into three segments and the local angle of attack of each section changes due to the wing upwash in the area ahead of the wing and downwash in the area behind the wing (Nelson, 1998). The upwash gradient and downwash gradient is computed at different segments of the fuselage, where w_{f_i} is the width at the segment and Δx_i is the distance between segments. The change in aerodynamic center due to the fuselage is given as:

$$\Delta\bar{X}ac_f = -\left(\frac{dM}{d\alpha}\right) / \left(\bar{q}s\bar{c}C_{L_{\alpha_W}}\right) \tag{10.5}$$

$$\left(\frac{dM}{d\alpha}\right) = (\bar{q}/36.5)(C_{L_{\alpha_W}}/0.08) \sum_{i=0}^{i=l_f} \left(w_{f_i}\right)^2 \left(\frac{d\bar{\varepsilon}}{d\alpha}\right)_i \Delta x_i \tag{10.6}$$

The segment 1-7 is ahead of the wing and the segment 8-13 is behind the wing. The upwash gradient for segment 1-7 from figure below.

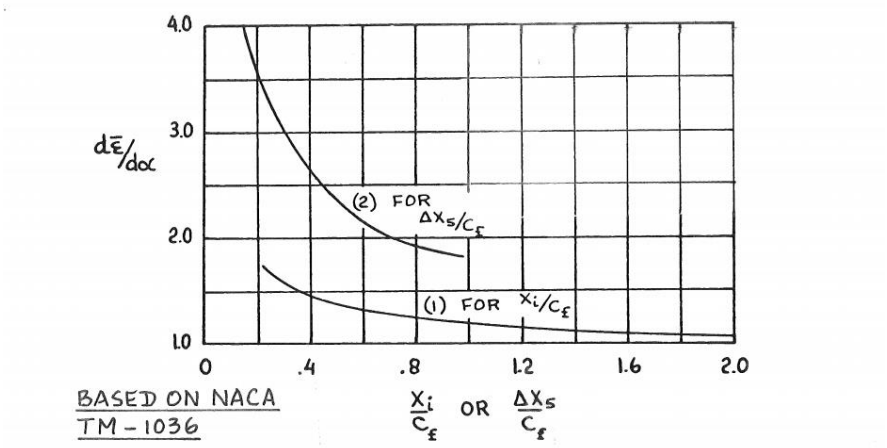

Figure 10.1 Upwash gradient due to fuselage (Roskam, *Airplane Design: Part VI*, 2018)

The region 7-8 is between the wing leading edge and trailing edge and the gradient is assumed unaffected by the wing's flow field (Nelson, 1998). The downwash gradient i.e., $\left(\frac{d\bar{\varepsilon}}{d\alpha}\right) < 1$ for the segment 8 – 13 is computed using the formula below (Roskam, *Airplane Design: Part VI*, 2018):

$$\left(\frac{d\bar{\varepsilon}}{d\alpha}\right) = \left(\frac{x_i}{x_h}\right)\left(1 - \frac{d\varepsilon}{d\alpha}\right) \tag{10.7}$$

$$\left(\frac{d\varepsilon}{d\alpha}\right) = \frac{4 \cdot 44\left(k_A k_\lambda k_n \sqrt{\cos \Lambda_{C/4}}\right)^{1.19} C_{L_{\alpha_{W_{M=0.75}}}}}{C_{L_{\alpha_{W_{M=0}}}}} \tag{10.8}$$

The lift curve slope of the wing is computed using the lift curve slope of the airfoil chosen for the wing NASA SC(2) 0612 and NASA SC(2) 0610. The lift-curve slope is computed using the equation below (Roskam, *Airplane Design: Part VI*, 2018)

.

$$C_{L_{\alpha_w}} = \frac{2\Pi AR_w}{\left[2 + \left\{\left(\frac{AR^2\beta^2}{k^2}\right)\left(I + \frac{\tan^2 \Lambda_{\frac{C}{2}}}{\beta^2}\right) + 4\right\}^{1/2}\right]} \quad (10.9)$$

The aspect ratio of the wing is 8.7 and the sweep angle at semi-chord location is obtained from the wing drawing which is equal to 21.9. The lift curve slope of the airfoils obtained at low speed are averaged as 0.09 deg^{-1}. The high-speed lift curve slope requires compressibility correction i.e., for a Mach number of 0.75. It is computed using the equations below:

$$\beta = \sqrt{1 - M^2} \quad (10.10)$$

$$k = \frac{c_{l_{\alpha_{at\,M}}}}{(2\pi\ /\ \beta)} \quad (10.11)$$

The lift-curve slope at M = 0.75 is computed with the following relation:

$$c_{l_{\alpha_{at\,M}}} = c_{l_{\alpha_{at\,M=0}}} / \beta \quad (10.12)$$

The lift-curve slope at M = 0 and M = 0.75 are 0.1158 deg^{-1} and 0.0767 deg^{-1} respectively. The remaining parameters in the equation 10.8 are estimated using the following equations obtained from Roskam (Roskam, *Airplane Design: Part VI*, 2018):

$$K_A = \left(1/_{AR}\right) - \frac{1}{(1 + AR^{1.7})} \quad (10.13)$$

$$k_\lambda = \frac{10 - 3\lambda}{7} \quad (10.14)$$

$$k_h = (1 - |h_h\ /\ b|)\ /\ \left(\frac{2l_h}{b}\right)^{1/3} \quad (10.15)$$

To compute the downwash gradient, the parameter h_h is equated to 0. The parameter h_h is the vertical location of the horizontal tail from the wing. Since, the downwash gradient at the wing is computed in this section, the parameter h_h will not be used for the calculation of wing-fuselage contribution to the horizontal stability. The assumed location of the fuselage, width of each section and the upwash/downwash gradient are tabulated below:

Table 10.1 Upwash and downwash along the fuselage

Fuselage station	X_i	w_{f_i}	$d\bar{\varepsilon} / d\alpha$
1	1.06	1.28	1.73
2	1.8	1.75	1.5
3	2.58	2.07	1.4
4	3.19	2.23	1.3
5	3.81	2.34	1.2
6	5.31	2.42	1.1
7	8.05	2.42	0
8	13.05	2.42	0.2143
9	16.61	2.42	0.1525816
10	17.83	2.39	0.0522892
11	19.83	1.86	0.08572
12	22.83	0.87	0.12858
13	23.83	0.05	0.04286

The aerodynamic shift due to the fuselage is computed by substituting the value obtained from the table in the equations 10.5 through 10.7. It results in a shift of -0.055 as a function of the MAC of wing. The aerodynamic center of wing-fuselage is obtained using equation 10.4.

$\bar{X}ac_{wf} = 0.25 - 0.055 = 0.195$

The stability equation has another component i.e. lift curve slope of the wing-fuselage. It is determined by multiplying the lift curve slope of the wing with a factor k_{wf} (Roskam, *Airplane Design: Part VI*, 2018) which is expressed as follows:

$$k_{wf} = 1 + 0.025\left(\frac{d_f}{b}\right) - 0 \cdot 25\left(\frac{df}{b}\right)^2 \tag{10.16}$$

10.2.2 Contribution of horizontal tail to the aerodynamic center

The horizontal tail and the stabilizer play a major part in stabilizing the aircraft in the longitudinal axis. In the AC leg equation, the parameters associated with the horizontal tail such as the lift-curve slope of the horizontal tail and the horizontal tail downwash gradient are estimated using a procedure similar to the lift-curve slope of the wing. The location of the horizontal tail from the wing is included in computing the downwash gradient at the tail.

10.2.3 Calculation of AC leg

The equation 10.2 is used for computing the AC leg. The summary of parameters required for the calculation are:

$\bar{X}ac_{wf}$ = 0.195; $C_{L_{\alpha_h}}$ = 0.131 deg^{-1}; $d\varepsilon_h/d\alpha$ = 0.5101; $C_{L_{\alpha_{wf}}}$ = 0.1158 deg^{-1}; $\bar{X}ac_h$ = 2.94

$\bar{X}ac_A$ = [0.195 + {0.131 (1 – 0.5101)(2.94)(S_h/S)/ 0.1158}] / F

$F = 1 + \{ 0.131(1 - 0.5101)(2.94)(S_h/S) / 0.1158 \}$

The longitudinal X-plot is shown below:

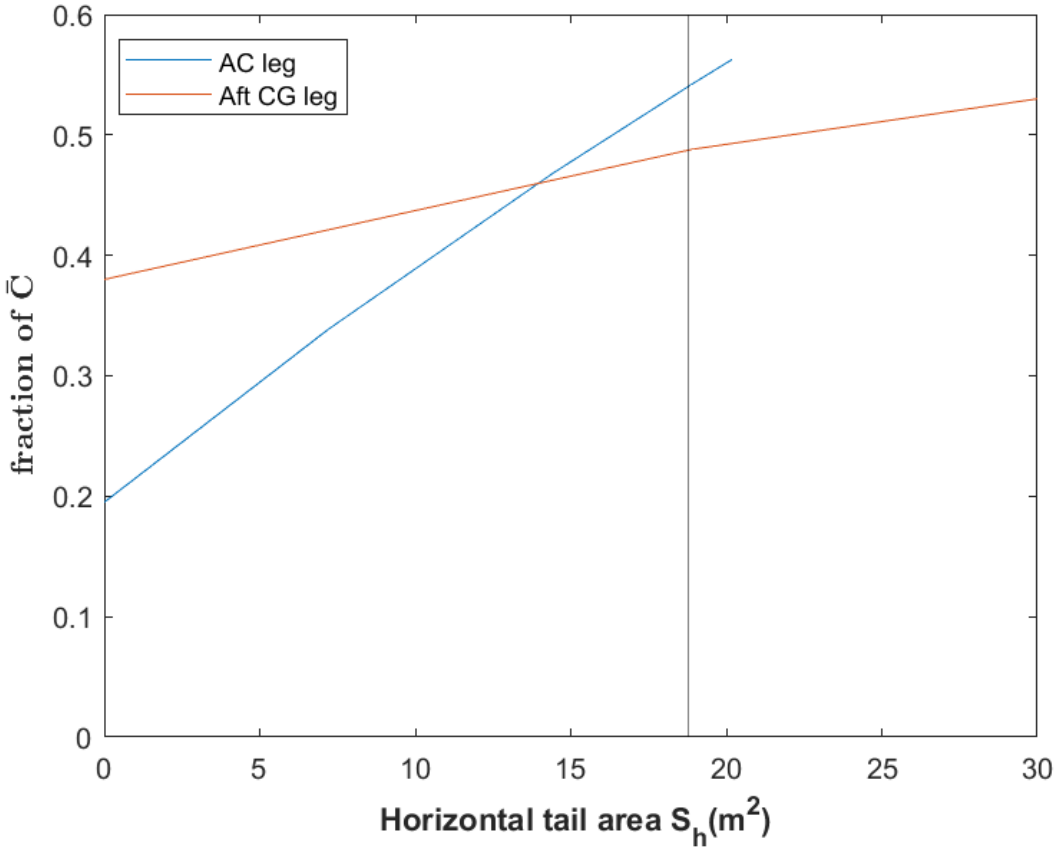

Figure 10.2 Longitudinal X-plot

The surface area of the tail for a static margin of 5% is 18.89 m^2, which is the same as the value obtained from tail sizing. Many iterations were performed between the horizontal tail, weight and balance analysis and stability and control to reduce the error percentage in the surface area of the horizontal tail.

10.2.4 Estimation of feedback gain

The aircraft is design with de-facto stability, which relies on augmentation system for stabilizing the aircraft. So, the feedback gain from the Stability Augmentation system is estimated from the following equations (Roskam, *Airplane Design: Part II*, 2018):

$$k_\alpha = \frac{(\Delta SM) C_{L_\alpha}}{C_{m_{\delta_e}}} \tag{10.17}$$

Where:

$$C_{L_\alpha} = C_{L_{\alpha_{wf}}} + \{C_{L_{\alpha_h}} (1 - (d\varepsilon_h/d\alpha)(S_h/S)\} \tag{10.18}$$

The feedback gain is computed for a negative static margin. The value of incremental static margin in the equation 10.9 is obtained from the de-facto stability requirement:

$$\Delta SM = \left|\bar{x}_{ac} - \bar{x}_{cg} - 0.05\right| \tag{10.19}$$

The highest level of static instability is when the feedback gain is above 5 deg/deg. i.e 5 deg. of elevator per degree of angle of attack. The contribution of elevator to the pitching moment coefficient is computed using the following relations: The feedback gain value for a static instability of -0.1 with $C_{L_\alpha} = 0.1324$ and $C_{m_{\delta_e}}$= -0.0478 is 0.2773. The elevator control effectiveness is obtained using the relation below (Nelson,1998):

$$C_{m_{\delta_e}} = -\eta_h v_h C_{L_{\alpha_h}} \tau \tag{10.20}$$

10.3 Directional stability

Directional stability is the static stability of the airplane about the Z-axis. The vertical tail is the main component providing directional stability to the aircraft. The wing's contribution to the directional stability is small and the fuselage provides a destabilizing contribution to the directional stability of the aircraft. Furthermore, the rudder provides directional control to the aircraft. The overall directional stability equation is written as (Roskam, *Airplane Design: Part II*, 2018):

$$C_{n_\beta} = C_{n_{\beta_{wf}}} + C_{L_{\alpha_V}}(s_v/s)(x_v/b) \tag{10.21}$$

For the aircraft to be directionally stable the yawing moment due to sideslip C_{n_β} should be a positive value (Nelson, 1998).

The wing-fuselage contribution to the directional stability is calculated using the equation below (Nelson, 1998):

$$C_{n_{\beta_{wf}}} = -k_n k_{RI}\left(\frac{S_{bs}}{S_w}\right)\left(\frac{l_f}{b}\right) \tag{10.22}$$

The empirical factor k_n is computed with the figure 10.4 which accounts for the effect of wing-fuselage interference with directional stability. The factor k_{Rl} is the Reynolds number correction factor. The value is obtained from the figure below.

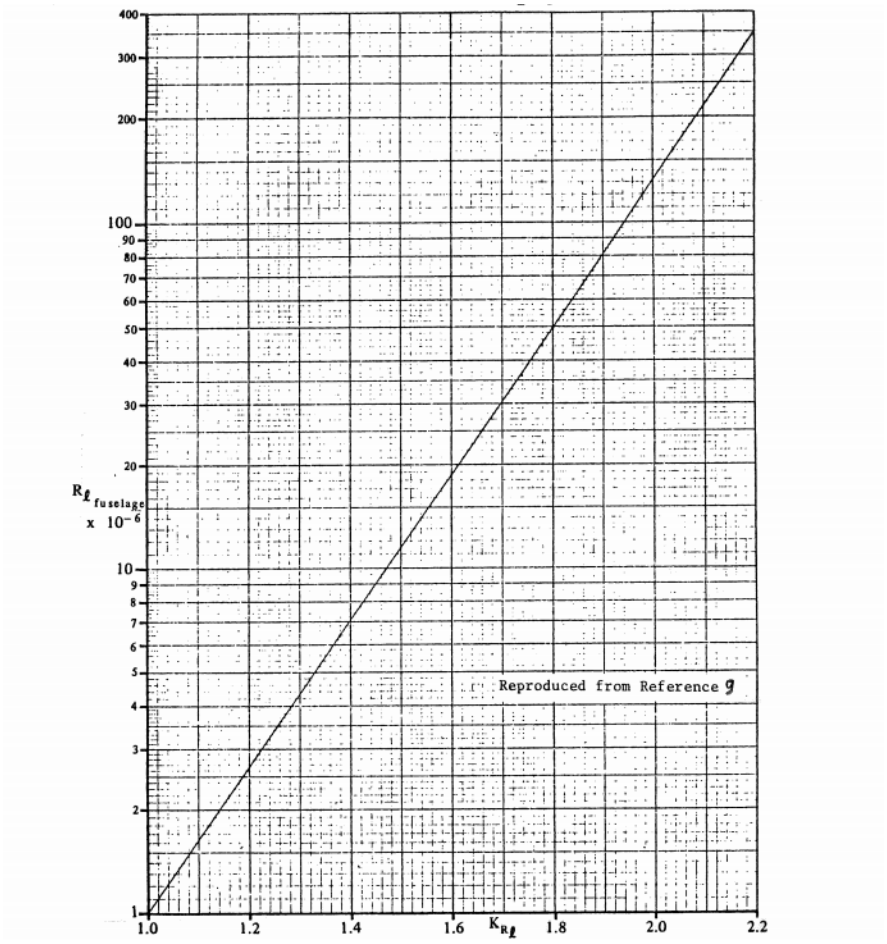

Figure 10.3 Reynolds number correction factor (Roskam, *Airplane Design: Part VI*, 2018)

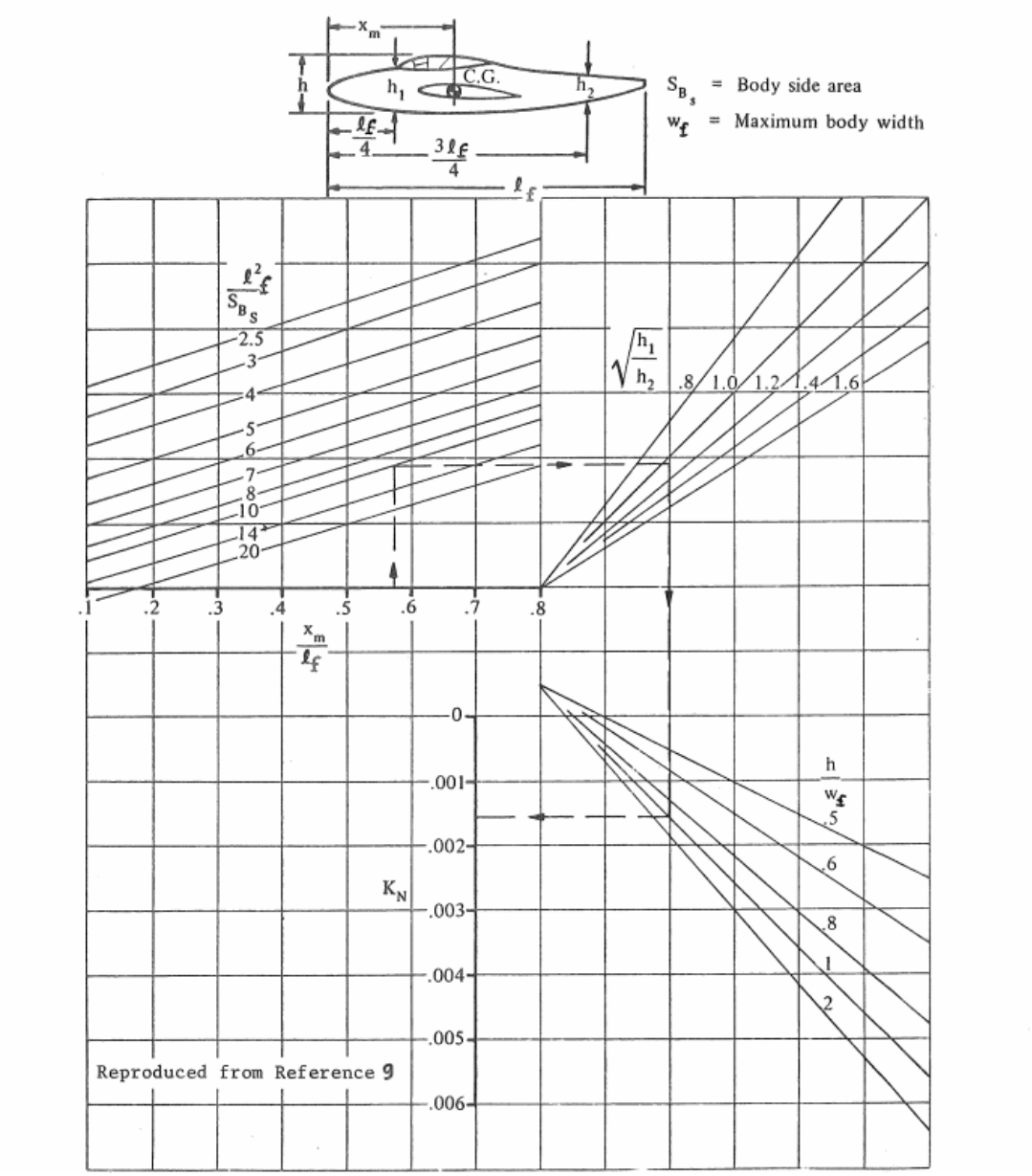

Figure 10.4 Wing-fuselage interference factor (Roskam, *Airplane Design: Part VI*, 2018)

The contribution of vertical tail to the directional stability could be computed in two ways i.e. using the formula below or using the lift curve slope of the vertical tail:

$$C_{n_{\beta_v}} = V_v \eta_v C_{l_{\alpha_v}} (1 + (d\sigma/d\beta)) \tag{10.23}$$

The lift curve slope of the vertical tail is computed using the procedure followed for computing the lift-curve slope for wing and horizontal tail. The values are substituted in the directional stability equation and the yawing moment coefficient is plotted as a function of the vertical tail

surface area. The directional X-plot for the medium range hybrid business jet is shown in the figure below:

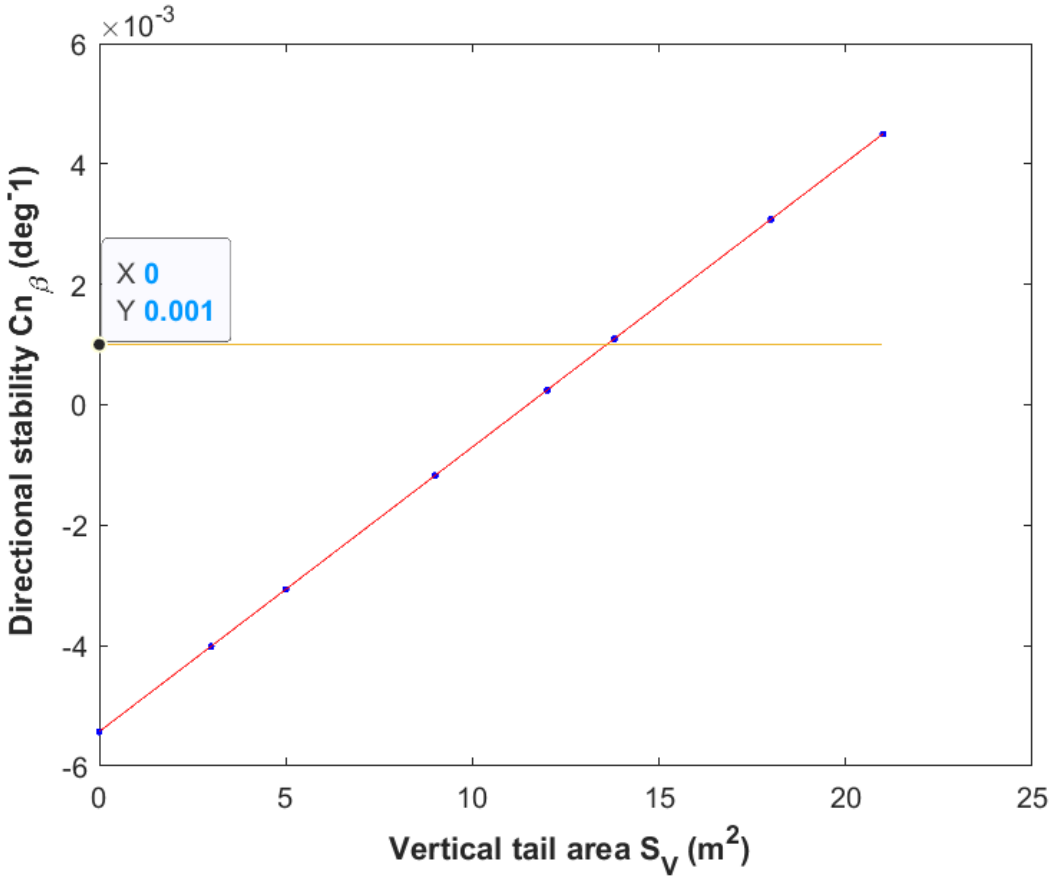

Figure 10.5 Directional X-plot

Since, the aircraft is designed with de-facto stability, the feedback gain for a certain level of yawing moment instability has to be computed. The additional value of yawing moment for an instability of C_{n_β} = -0.0031 is:

$$\Delta C_{n_\beta} = 0.0010 - C_{n_\beta} \tag{10.24}$$

The required sideslip to rudder feedback gain is computed using the equation below. The computed feedback gain should not exceed 5 deg/deg (Roskam, *Airplane Design: Part II*, 2018).

$$k_\beta = \frac{\Delta C_{n_\beta}}{C_{n_{\delta_r}}} \tag{10.25}$$

The yawing moment coefficient due to rudder deflection is the rudder control effectiveness, which is computed using the following relation (Nelson, 1998):

$$C_{n_{\delta_r}} = -\eta_v v_v C_{L_{\alpha_v}} \tau \tag{10.26}$$

The flap effectiveness parameter τ is computed as 0.6 (Nelson, 1998) based on the control surface area to the lifting surface area of the tail which is assumed as 0.4. The tail efficiency factor η_v is the ratio of dynamic pressure at the tail to the dynamic pressure at the wing. The rudder control effectiveness $C_{n_{\delta_r}} = -0.0044$ deg^{-1}. This yields a feedback gain of 0.9370 deg/deg.

10.4 Minimum control speed with one engine inoperative

In the event of an engine failure in a multi-engine aircraft, asymmetric thrust is produced. The rudder must have the ability to counter the yawing moment produced by the asymmetric thrust (Nelson, 1998). In this section, the rudder deflection to counter the yawing moment is determined using Roskam's method (Roskam, *Airplane Design: Part II*, 2018). The critical engine-out yawing moment is computed using the following equation:

$$N_{t_{crit}} = T_{To_e} Y_t \tag{10.27}$$

The moment arm from the fuselage centreline is Y_t = 1.8 m and thrust from single engine is equal to 47.3 kN. This results in $N_{t_{crit}}$ = 8672 kg m.

The next step is to determine the drag induced yawing moment due to inoperative jet engine with a wind milling engine and high by-pass ratio, which is given as:

$$N_D = 0.25 N_{t_{crit}} \tag{10.28}$$

The maximum allowable minimum control speed is 1.2 times the stall speed during landing. In the performance sizing, the stall speed during landing was plotted as a function of the wing loading and coefficient of lift. The lowest landing stall speed is 15.92 m/s which results in a

minimum control speed of 19.1 m/s. The rudder deflection required to hold the engine out condition (one engine inoperative) at the minimum control speed is computed using the equation below:

$$\delta_r = \frac{N_D + N_{crit}}{\overline{q_{mc}}\left(SbC_{n_{\delta_r}}\right)} \tag{10.29}$$

Substituting the value of dynamic pressure for the cruise density and other parameters, the rudder deflection obtained is 24.6 deg which is less than the limit of 25 degrees. Initially, the rudder surface area was chosen as 0.28 times the tail surface area, but to satisfy the rudder deflection requirement, the rudder surface area ratio has been increased to 0.4.

11. Drag Polar estimation

11.1 Introduction

The drag polar plot gives the relationship between the coefficient of lift and the coefficient of drag. Drag on an aerodynamic body comprises of the lift-induced drag and the zero-lift (skin-friction) drag. The zero-lift drag is due to the shear stress exerted on the surface of the body, which is purely based on the wetted surface area (surface area exposed to air) of the vehicle. The lift-induced drag is due to the lift (pressure force) produced by the body. The drag polar for the take-off, landing and cruise are computed using the methodology presented in the performance sizing chapter. In the performance sizing, the wetted surface area was assumed for computing the drag polar. In this chapter, a detailed estimation of the wetted surface area is carried out. The purpose of this chapter is to estimate if the lift-to-drag ratio from the computed drag polar equals the assumed $(L/D)_{max}$ in the weight sizing chapter. If the exposed surface area or other factors result in a low L/D, the aircraft will not be able to meet the range requirement and so, the components will have to be resized. Besides, a low L/D will lead to a weight penalty as the battery and fuel weight necessary for the mission is extremely dependent on the L/D. The computation of the wetted surface area of the components using empirical relations and AAA (Advanced Aircraft Design) software and the drag polar are presented in this chapter.

11.2 Determination of Zero-lift drag

The possibility of achieving a lift-to-drag ratio depends extensively on the zero-lift drag. The zero lift-drag is expressed as a function of the equivalent parasite area (f), and surface area of the wing (as mentioned in the climb sizing). The equivalent parasite area is dependent on the wetted surface of the primary components. The effect of compressibility due to high speed is taken into consideration for computing the clean (without flaps and landing gear) zero-

lift drag coefficient. The low speed drag increment due to the deployment of flaps and landing gears during take-off and landing are considered for the determination of the take-off and landing drag polar plots. The components contributing to the zero-lift drag are:

- fuselage
- wing
- empennage
- nacelles
- landing gear
- flaps

11.2.1 Wetted surface area of the fuselage

In the fuselage design chapter, the length of nose, fuselage, and fineness ratio were estimated. The wetted surface area for the fuselage is computed by using the following equation from Roskam (Roskam, *Airplane Design: Part II*, 2018):

$$Swet_{fus} = \pi l_f D_f (0.50 + (0.1351\, l_n/l_f))^{2/3}\, (1.015 + (0.3/\lambda_f)^{1.5}) \qquad (11.1)$$

The parameters are tabulated below:

Table 11.1 Fuselage parameter for the determination of wetted surface are

l_n	5.31 m
l_f	23.83 m
λ_f	9.5
D_f	2.5 m

11.2.2 Wetted surface area of the wing and empennage

The wetted surface area of the wing depends on the exposed planform area. The region of fuselage-wing interference is excluded from the exposed planform area. The region of the vertical and horizontal tail interference area will be subtracted while calculating the net wetted surface area.

The expression provided below (Roskam, *Airplane Design: Part II*, 2018) is used for determining the wetted surface area of the wing and empennage. It shows that the wetted surface depends on the thickness to chord ratio of the wing and the taper ratio.

$$S_{wet_{planform}} = 2S_{exp_{planform}}\left(1 + \frac{0.25\left(\frac{t}{c_r}\right)(1+\tau\lambda)}{1+\lambda}\right) \tag{11.2}$$

The wetted surface area is computed using AAA analysis and the result is shown below:

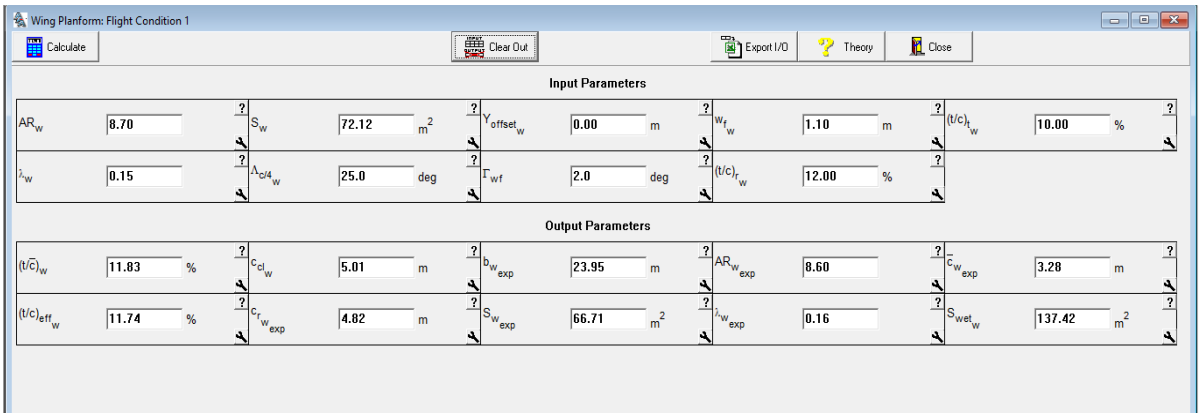

Figure 11.1 Wetted surface area of the wing – AAA analysis

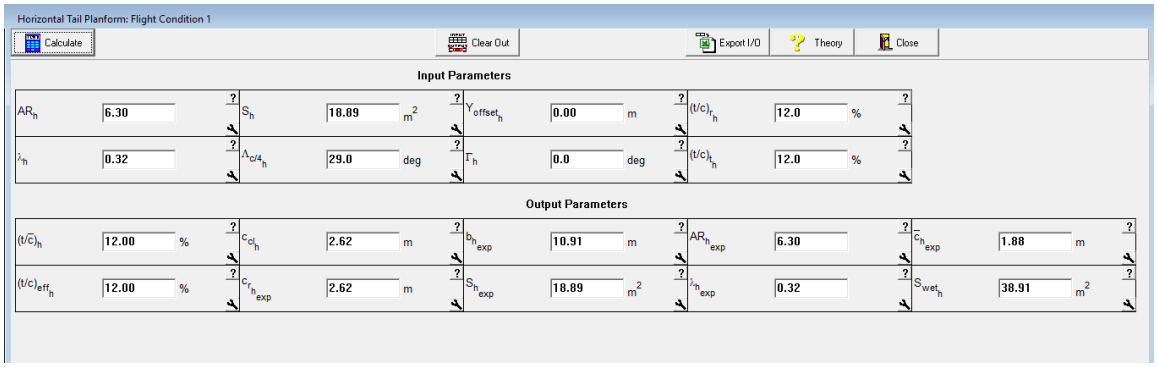

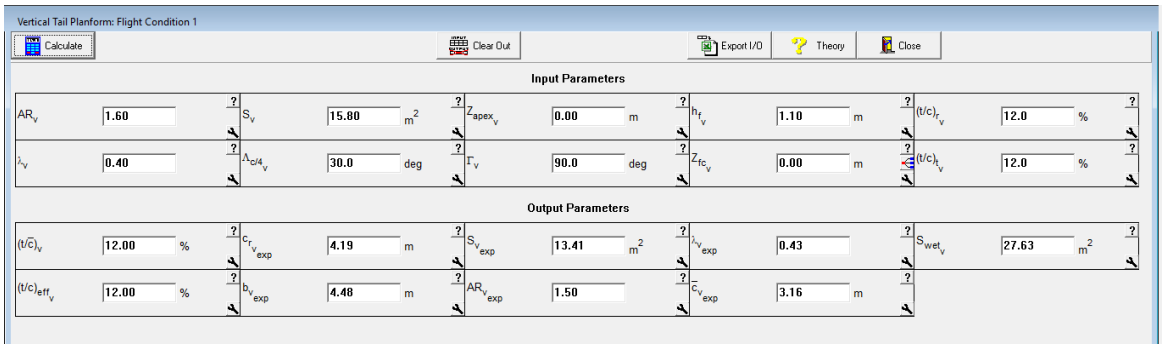

Figure 11.2 Wetted surface area of the empennage – AAA analysis

11.2.3 Wetted surface area of the nacelles

The detailed geometry of the nacelle and the powerplant for the hybrid engine are currently not available. A rough determination of the wetted surface area will be carried out using the perimeter method. The following assumptions are made based on the engine data used for business jet aircraft (GE Aviation, n.d.):

- Length of the engine = 2.8 m
- Diameter of the engine = 1.2 m

The wetted surface area of one nacelle is estimated as 10.75 m^2. So, the total area is 21.5 m^2.

11.3 Total wetted surface area

Table 11.2 Total wetted surface area

Component	**Wetted area (m^2)**
Fuselage	125.2
Wing	137.4
Horizontal tail	38.9
Vertical tail	28.6
Nacelle	21.5
Intersection of Horizontal and vertical	-2
Total wetted surface area	**349.6**

The wetted surface area assumed in the performance sizing was 353 m^2 (3800 ft^2), which is 4m^2 greater than the value obtained from the wetted surface area determination. In addition to this, there are other contributions to the overall drag from high-speed compressibility effects, take-off and landing flaps and landing gears. The drag increment due to high-speed compressibility is found as 0.0003 for M = 0.75. The increment from flap during take-off and landing are 0.015 and 0.016. The drag increment due to the landing gear is 0.017. The new drag polar equations with the calculated wetted surface area is presented below. Using the data,

the maximum lift-to-drag ratio will be estimated. The lift-to-drag ratio of 22 was assumed in the weight sizing. Since, the L/D is crucial in achieving the desired range, it is important to obtain the same value within 5% error margin. The new equivalent skin friction area will 9.24 ft^2 (0.858 m^2).

Cruise: $C_D = 0.0122 + 0.043{C_L}^2$

Take-off + gear-up: $C_D = 0.0272 + 0.0457{C_L}^2$

Take-off + gear-down: $C_D = 0.0457 + 0.0457{C_L}^2$

Landing + gear-up: $C_D = 0.0722 + 0.0488{C_L}^2$

Landing + gear-down: $C_D = 0.0895 + 0.0488{C_L}^2$

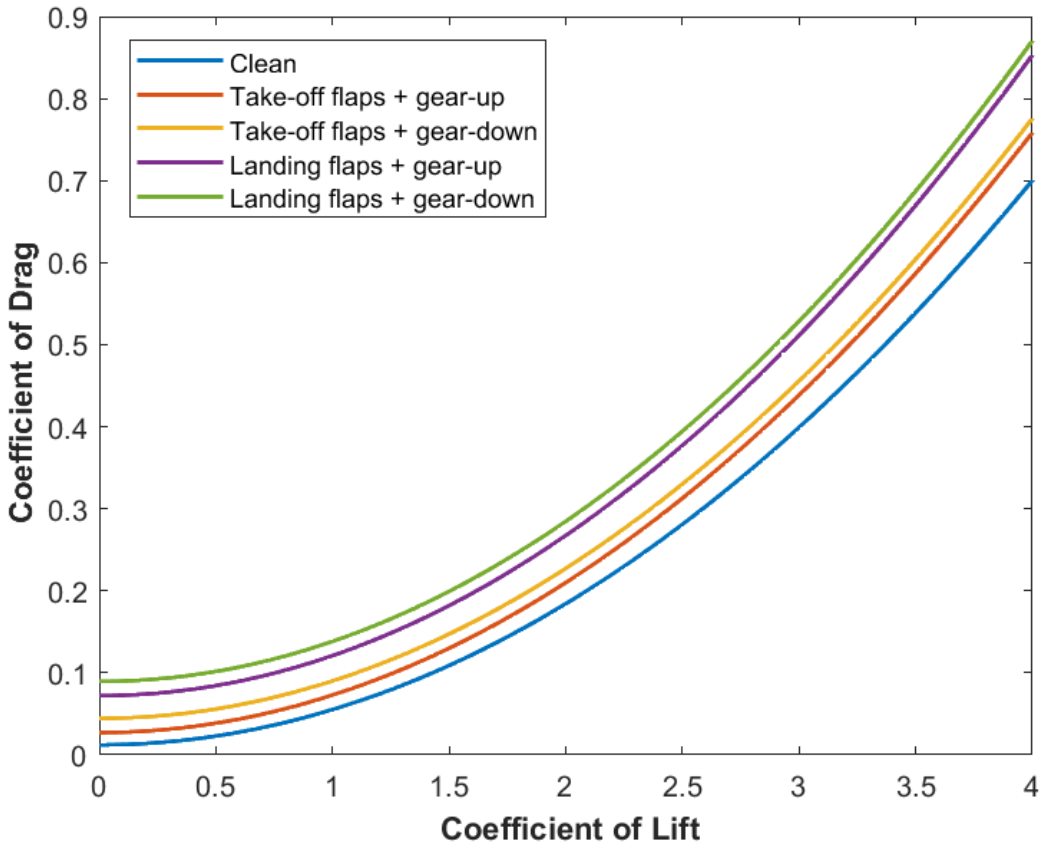

Figure 11.3 Drag polar for the medium-range hybrid business jet

From the drag polar, the maximum lift to drag ratio for the clean configuration is computed using the formula:

$$\left(\frac{L}{D}\right)_{\max} = \frac{1}{2}\sqrt{\frac{1}{kC_{D0}}} \tag{11.3}$$

The calculated lift-to-drag ratio is 21.83 which is 0.7% less than the assumed lift to drag ratio for preliminary sizing. The take-off weight is calculated with the L/D of 21.83 and the value obtained is 30280 kg, which is 4% greater than the take-off weight estimated in the weight sizing. Since, the value change is lesser than 5%, the lift-to-drag ratio will not be changed in this final stage of preliminary sizing.

12. Environmental and safety considerations

12.1 Introduction

While the feasibility study and the preliminary design process were carried out completely showing that the medium-range hybrid business might be feasible in 2030, there are certain environmental and preliminary safety considerations that have to be analysed before proceeding with the detailed design of the aircraft.

12.2 Environmental consideration

The primary purpose of replacing the fuel with the battery for propulsion is to reduce the environmental hazard. While the batteries reduce the amount of fuel consumed, the production of batteries itself requires more energy leading to considerable greenhouse gas emission. The current research on the battery production for electric cars shows a 74% more carbon dioxide emission than fuel-powered cars, if the batteries are produced in a factory powered by fossil fuels (Ramey, 2018). In addition to this the extraction of lithium and production of batteries have a significant impact on the environment. This demands for a change in the battery production, lithium extraction and recycling processes.

12.3 Safety consideration

The non-aqueous lithium-oxygen batteries which are capable of producing high energy have a serious disadvantage in terms of the stability, low round-trip efficiency and air purification. Furthermore, the current challenging issue with the non-aqueous lithium- air battery is the possibility of internal short-circuiting in the cell during lithium dendrite formation, which is a serious issue in terms of safety (Imanishi & Yamamoto, 2019). The aircraft might require frequent replacement of the batteries due to the low life cycle. The disposal of batteries are very crucial as the lithium-based batteries are not very environmentally

friendly and may impose health hazard if not discarded properly. There are numerous ongoing researches in developing lithium-oxygen batteries and resolving its issues and the batteries are expected to become a power source for the electric vehicles in the future.

12.4 Final CAD drawings of the medium-range hybrid business jet

The preliminary sizing of the medium-range hybrid business jet has been completed. The final specification of the hybrid aircraft is tabulated below:

Table 12.1 Specifications of medium-range hybrid business jet

Total take-off weight	29112 kg
No: of passengers + crew	11 + 3
Fuel weight	5084 kg
Battery Weight	8013 kg
Range	7000 km
Maximum Lift-to-drag ratio	22
Take-off wing loading	403 kg/m^2
Take-off Thrust-to-Weight ratio	0.331 (94.5 kN Thrust) at 1524 m altitude
Wingspan	25.05 m
Wing area	72.12 m^2
Fuselage length	23.83 m
Cabin length	11 m
Cabin height	1.88 m
Fuselage height	2.6 m
Fuselage width	2.42 m
Cabin volume	52.8 m^3
Aspect ratio	8.7
Take-off distance	1828 m
Landing distance	1600 m

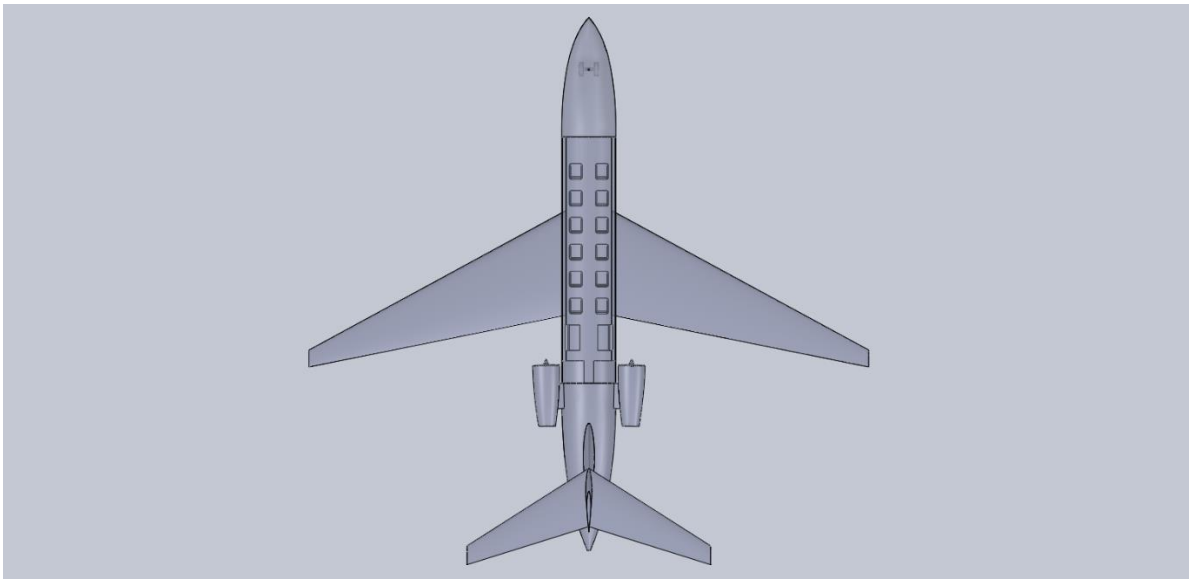

Figure 12.1 Top view of the hybrid business jet

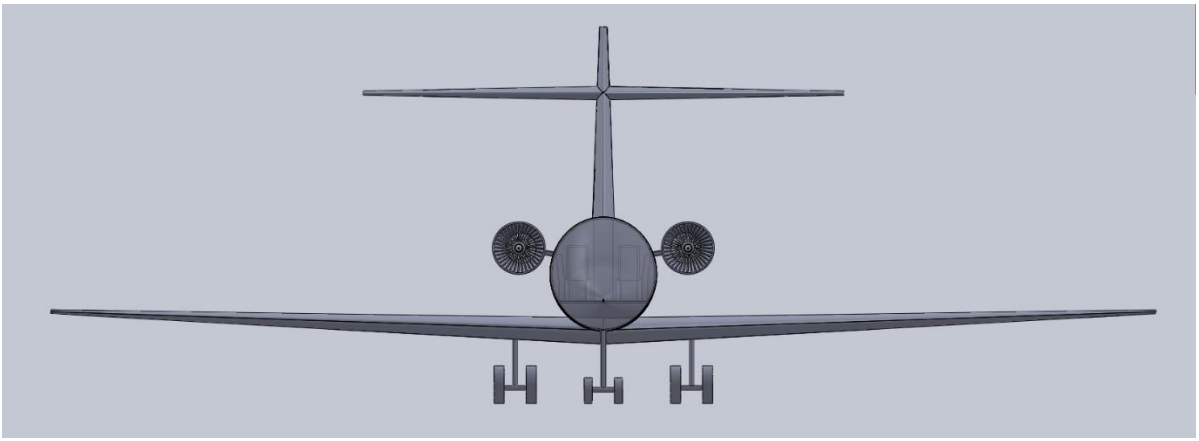

Figure 12.2 Front view of the hybrid business jet

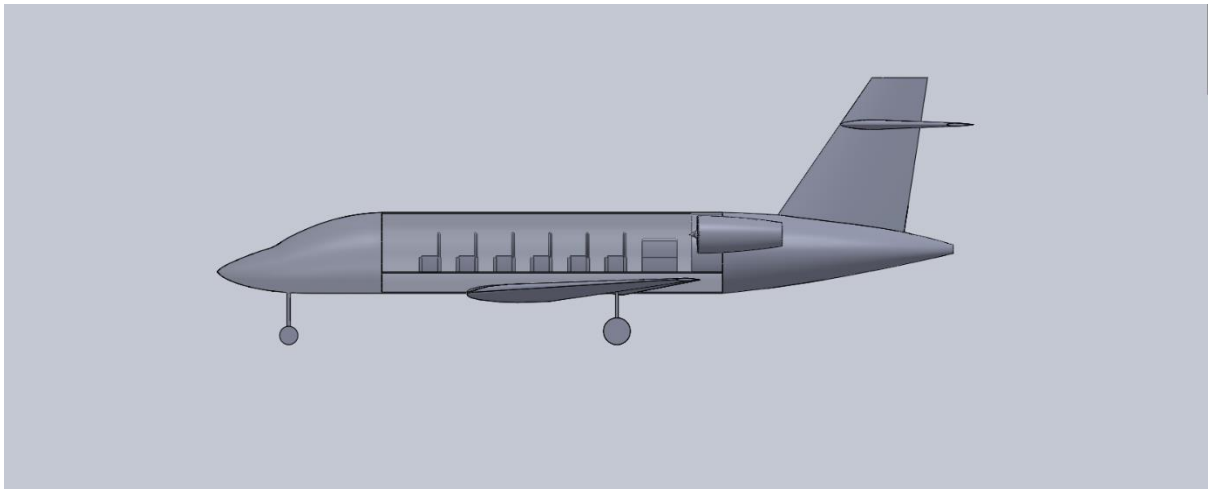

Figure 12.3 Side view of the hybrid business jet

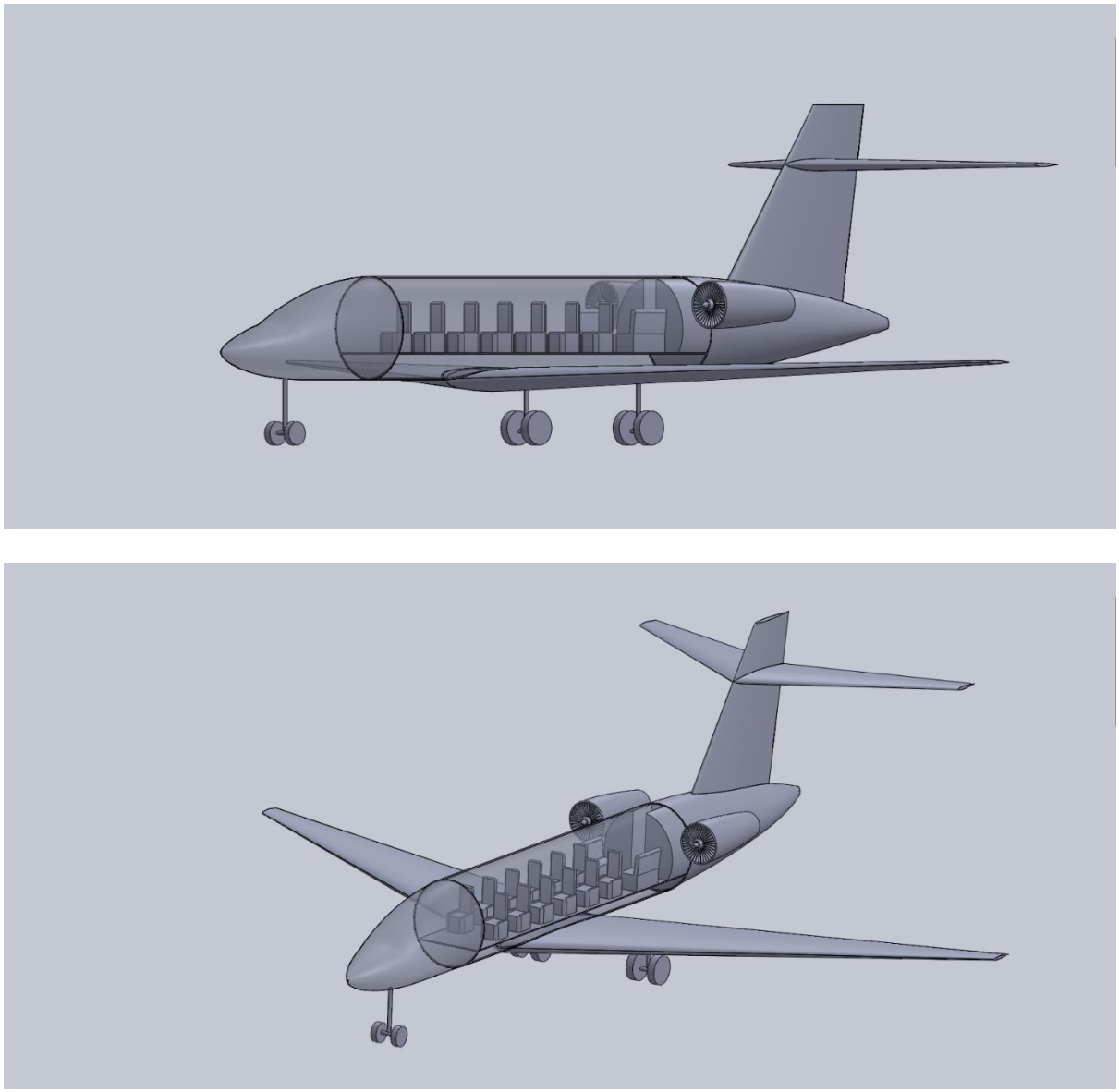

Figure 12.4 Isometric views of the hybrid business jet

References

Aircraft electrification market (2020, February). Retrieved October 06, 2020, from https://www.marketsandmarkets.com/Market-Reports/aircraft-electrification-market-31650461.html

Airfoil NASA SC(2)- 0612 (n.d.). Retrieved July 10, 2020, from http://airfoiltools.com/airfoil/details?airfoil=sc20612-il

Airfoil NASA SC(2)- 0610 (n.d.). Retrieved July 10, 2020, from http://airfoiltools.com/airfoil/details?airfoil=sc20610-il

Bombardier Challenger 650 specification (n.d.) Retrieved May 08, 2020, from https://businessaircraft.bombardier.com/en/aircraft/challenger-650

Bowman, C. L., Marien, T. V., & Felder, J. L. (2018). *Turbo- and Hybrid-Electrified Aircraft Propulsion for Commercial Transport.* https://ntrs.nasa.gov/citations/20180005437

Bradley, M.K., & Droney, C.K. (2011, April). *Subsonic Ultra Green Aircraft Research: Phase I Final Report* (Report No. NASA/CR-2011-216847). https://ntrs.nasa.gov/citations/20110011321

Bradley, M. K., & Droney, C. K. (2015, April). *Subsonic Ultra Green Aircraft Research: Phase II- Volume II-Hybrid Electric Design Exploration* (Report No. NASA/CR-2015-218704/VOL2). https://ntrs.nasa.gov/citations/20150017039

Falcon -900 LX specification (n.d.) Retrieved May 08, 2020, from https://www.dassaultfalcon.com/en/Aircraft/Models/900LX/Pages/overview.aspx

Falcon -2000S specification (n.d.) Retrieved May 08, 2020, from https://www.dassaultfalcon.com/en/Aircraft/Models/2000S/Pages/overview.aspx

Falcon -2000LXS specification (n.d.) Retrieved May 08, 2020, from https://www.dassaultfalcon.com/en/Aircraft/Models/2000LXS/Pages/overview.aspx

Filippone, A. (2000). Data and performances of selected aircraft and rotorcraft. *Progress in Aerospace Sciences, 36(8)*. 629–654. https://doi.org/10.1016/s0376-0421(00)00011-7

GE Aviation, Commercial engine specification (n.d.) Retrieved April 04, 2021, from https://www.geaviation.com/commercial/engines/cf34-engine

Global carbon-dioxide emissions (2020, January). Retrieved June 10, 2020, from https://www.c2es.org/content/international-emissions/

Hepperle, M. (2012, October 22). Electric Flight - Potential and Limitations. Retrieved from https://elib.dlr.de/78726/

Imanishi, N., & Yamamoto, O. (2019). Perspectives and challenges of rechargeable lithium–air batteries. *Materials Today Advances, 4*, 100031. doi:10.1016/j.mtadv.2019.100031

Jet fuel properties (2021, May 03). Retrieved May 12, 2021, from https://en.wikipedia.org/wiki/Jet_fuel

Knapp, M., & Said, W. (2018). *Zunum Aero's Hybrid electric airplane aims to rejuvenate regional travel*. IEEE Spectrum: Technology, Engineering, and Science News. Retrieved June 05, 2020, from https://spectrum.ieee.org/aerospace/aviation/zunum-aeros-hybrid-electric-airplane-aims-to-rejuvenate-regional-travel

Market forecast (2020, May). Retrieved 06 October,2020 from https://www.marketforecast.com/reports/global-electric-and-hybrid-aircraft-market-technology-forecast-to-2028-1153?utm_source=dsj&utm_medium=affiliate

Nelson, R.C.(1998). *Flight stability and automatic control,* 2nd ed. Boston: WCB/ McGraw-Hill

Pipistrel Aircraft, PB345V124E-L battery pack parameters (n.d.). Retrieved April 15, 2021, from https://www.pipistrel-aircraft.com/aircraft/electric-flight/batteries-systems-and-bms/

Ramey, J. (2018, October 23). Are EV battery PLANTS creating more pollution than EVs eliminate? Retrieved May 12, 2021, from https://www.autoweek.com/news/green-cars/a1709966/will-some-gas-and-diesel-cars-still-produce-less-pollution-evs/

Raymer, D. P. (2012). *Aircraft Design: A Conceptual Approach (5th ed.).* American Institute of Aeronautics and Astronautics

Roskam, J. (2018). *Airplane Design: Part 1: Preliminary Sizing of Airplanes*. Lawrence, KS, Design, Analysis and Research Corporation

Roskam, J. (2018). *Airplane design: Part I1: Preliminary Configuration Design and Integration of the Propulsion System*. Lawrence, KS, Design, Analysis and Research Corporation

Roskam, J. (2018). *Airplane design: Part II1: Layout Design of Cockpit, Fuselage, Wing and Empennage: Cutaways and Inboard Profiles*. Lawrence, KS, Design, Analysis and Research Corporation

Roskam, J. (2018). *Airplane design: Part V: Component Weight Estimation*. Lawrence, KS, Design, Analysis and Research Corporation

Roskam, J. (2018). *Airplane design: Part VI: Preliminary Calculation of Aerodynamic, Thrust and Power Characteristics.* Lawrence, KS, Design, Analysis and Research Corporation

Sadraey, M.H. (2013). *Aircraft Deisgn: A systems engineering Approach*. John Wiley & Sons, Ltd

UIUC Airfoil Coordinates Database NASA SC(2)- 0612 (n.d.) Retrieved April 30, 2021, from https://m-selig.ae.illinois.edu/ads/afplots/sc20612.gif

UIUC Airfoil Coordinates Database NASA SC(2)- 0610 (n.d.) Retrieved April 30, 2021, from https://m-selig.ae.illinois.edu/ads/afplots/sc20610.gif

Zunum Aero's Hybrid Electric Aircraft (n.d.). Retrieved June 10, 2020, from https://zunum.aero/

Appendix A: Determination of regression constant for weight sizing

Empty Weight fraction

$$\frac{W_E}{W_{TO}} = (0.95)\, a\, W_{TO}^{C} \quad \text{— (1)} \qquad [a = 1.02 \; ; \; C = -0.06]$$

$$\log\left(\frac{W_E}{W_{TO}}\right) = \log(0.95\,a) + C \log W_{TO}$$

$$\log W_E = \log W_{TO} + C \log W_{TO} + \log(0.95\,a)$$

$$\log W_E = \log W_{TO}(1 + C) + \log(0.95\,a)$$

$$\log W_{TO} = \frac{\log W_E}{1 + C} - \frac{\log(0.95\,a)}{1 + C} \quad \text{— (2)}$$

$$[\log W_{TO} = B \log W_E + A \quad \text{— (3)}]$$

Comparing (2) & (3)

$$B = \frac{1}{1 + C} \; ; \qquad A = -\frac{\log(0.95\,a)}{1 + C}$$

Regression constant

$$A = 0.0145 \qquad B = 1.0638$$

Appendix B: Weight sizing – MATLAB script

```
% MS Project AE 295 A & B: Design of a Medium-range hybrid business jet

% By: Karpagam Suryanarayanan

% Chapter: Weight sizing
```

Mission requirement

```
No_of_passengers = 11;

No_of_cockpitcrew = 2;

No_of_cabin_attendant = 1;

w_baggage = 17; %Baggage weight per person kg

Rfuel =3500; %Range (Fuel powered) km

Rbattery = 3500; %Range (battery powered) km

E_star =1750; %Specific energy density of (Li + O2) in Wh/kg

Vc = 222; %Cruise speed in m/s (500 knots)

Mc = 0.75; %Cruise Mach number

Hc = 12192; %Cruise altitude in m (40000ft)

TOFD = 1828; %Take-off field distance in m (Altitude: 5000 ft)

LFD = 1600; %Landing field distance in m (Altitude: 5000 ft)

Noise = 89; %Less than 89 EPNdB

n_total = 0.9; % Total efficiency
```

Initial weight estimation

```
%Input

l_d = 22; %Lift-to-drag ratio

g = 9.81; %Acceleration due to gravity in m/s^2

c_cruise = 0.5; %SFC (cruise)
```

```
c_loiter = 0.4; %SFC(loiter)

E = 45; %Loiter (Endurance in minutes)

%Weight estimation

W_baggage = w_baggage * 11; %Total weight of the baggage kg

m_person = 79.5; %Approx weight of passenger/crew in kg

Wpl = m_person*11 + W_baggage; %Payload weight in kg

Wcrew = m_person*3 + w_baggage*3; %Crew weight in kg

Wbattery_Wto = (Rbattery*1000*9.81)/(E_star*3600*l_d*n_total); %Battery weight
ratio

%Fuel weight estimation

W1_W0 = 0.990; %Engine start, warmup

W2_W1 = 0.99; %Taxi

W3_W2 = 0.995; %Take-off

W4_W3 =0.98; %climb

W5_W4 = exp(-((Rfuel*1000*c_cruise)/3600)/(Vc*l_d*0.866)); %Cruise segment

W6_W5 = exp(-(E*c_loiter)/(l_d*60)); %Loiter segment

W7_W6 = 0.99; %Descent

W8_W7 = 0.992; %Land, taxi and shut-down

mff = W1_W0*W2_W1*W3_W2*W4_W3*W5_W4*W6_W5*W7_W6*W8_W7; %Mission fuel fraction

Wf_Wto = (1-mff); %Fuel weight ratio
```

Take-off weight estimation

```
A = -(log10(0.969)) /0.94; % Regression constant (Appendix A)

B = 1/(1-0.06); % Regression constant (Appendix A)

Wto_guess = 5000:5:100000; %Take-off weight (guessed) in lb

We = ((log10(Wto_guess)-A)./B);
```

```
WE = (10.^We); %Opearating weight obtained

WOE_tent = Wto_guess - (Wf_Wto.*Wto_guess) - (Wpl*2.20462)-
Wbattery_Wto.*Wto_guess);

WE_tent = WOE_tent - (0.005.*Wto_guess) - (Wcrew*2.20462);

WEc = find(abs(WE_tent-WE)<= 5);
```

Design point for medium range hybrid business jet

```
figure(1)

w1= plot(Wto_guess/2.20462,WE/2.20462,'b','linewidth',1);

hold on;

w2 = plot(Wto_guess/2.20462,WE_tent/2.20462,'r','linewidth',1);

dp =
plot(29112,14519,'OR','MarkerEdgeColor','k','MarkerFaceColor',[0.2,0.2,0.3],'Marker
Size',5);

lgdw = legend([w1,w2],'W_{E_{allowable}} Vs W_{TO}','W_{E_{Tentative}} Vs W_{TO}');

xlabel('\bf Take-off weight W_{TO} (kg)');

ylabel('\bf Empty weight W_{E} (kg)');

Wto = (Wto_guess(WEc(1)))./2.20462; %Take-off weight in kg

Wtol = Wto*2.20462; % Take-off weight in lb

We_Wto = WE(WEc(1))/(Wto_guess(WEc(1))); %Empty weight fraction

Wempty = We_Wto*Wto; %Empty weight in kg

Wbattery = Wto *Wbattery_Wto ;%Battery weight in kg

Wf = Wf_Wto * Wto; %Fuel weight in kg
```

Sensitivity

```
C = 1-(1-mff)-0.005;

D = (Wpl+Wcrew+Wbattery)*2.20462;

F = (-(B*Wtol*Wtol))*(1/(((C*Wtol)*(1-B))-D)); % Breguet partial
```

```
% Take-off Weight sensitivity

dwto_dwe = B* Wtol*(10^(log10(Wtol)-A)/B)^(-1); % Empty weight

dwto_dwpl = (B*Wtol)/(D-(C*(1-B)*Wtol)); % Payload weight

dwto_dE = (F*c_loiter*(1/l_d))*0.453592; % Endurance (loiter) kg/hr

dwto_dRfuel = F*c_cruise*(1/(Vc*3.6*0.866*l_d)); % Range (kg/km)

dwto_dvc = -(F* Rfuel*c_cruise*0.453592)/(Vc^2*3.6*3.6*0.866*l_d); % cruise speed
(Fuel powered segment)(kg/kph)

dwto_dcjc = (F* Rfuel*0.453592)/(Vc*3.6*0.866*l_d); % SFC cruise (kg/hr)

dwto_dcjl = (F*0.453592*E)/(l_d*60); % SFC loiter (kg/hr)

dwto_dldcruise = -(F* Rfuel*c_cruise*0.453592)/(Vc*3.6*(0.866*l_d)^2); % Cruise
lift-to-drag ratio (kg)

dwto_dldloiter = -(F* E*c_loiter*0.453592)/(60*l_d^2); % Loiter lift-to-drag ratio
(kg)

dwto_dRbattery = ((Wpl+Wcrew)*9.81*1000) /((1-We_Wto-Wf_Wto-
Wbattery_Wto)*(E_star*3600*n_total*l_d)); % Range (battery powered) kg/km

% Range sensitivity (Electric)

dR_dwto = -((E_star*3600*n_total*l_d*Wbattery)/(g*Wto^2))/1000; % Take-off weight
km/kg

dR_dl_d = ((1-We_Wto)-((Wpl+Wcrew)/(Wto))-(Wf_Wto))*E_star*3600*n_total/(g*1000);
%lift-to-drag ratio (km)

dR_dEstar = (((1-We_Wto-((Wpl+Wcrew)/(Wto))-(Wf_Wto))*l_d*n_total)/g); %Specific
energy density (s^2/m)
```

Published with MATLAB® R2020a

Appendix C: Performance sizing (MATLAB SCRIPT)

```
clc

clear all

close all



% MS Project: Design of Medium-range hybrid business jet

% By: Karpagam Suryanarayanan

% Chapter: Performance sizing
```

Mission requirement

```
No_of_passengers = 11;

No_of_cockpitcrew = 2;

No_of_cabin_attendant = 1;

w_baggage = 17; %Baggage weight per person kg

Rfuel =3500; %Range (Fuel powered) km

Rbattery = 3500; %Range (battery powered) km

E_star =1750; %Specific energy density of (Li + O2) in Wh/kg

Vc = 222; %Cruise speed in m/s (500 knots)

Mc = 0.75; %Cruise Mach number

Hc = 12192; %Cruise altitude in m (40000ft)

TOFD = 1828; %Take-off field distance in m

LFD = 1600; %Landing field distance in m

Noise = 89; %Less than 89 EPNdB

n_total = 0.9; % Total efficiency
```

Take-off and landing distance sizing
Take-off

```
Wto = 29112;

TW_TO_5000ft = zeros(1,8,4);
```

```
S_TOFL = TOFD*3.28084;  % Field length in ft

TOP25 = S_TOFL/37.5;  % Take-off parameter lb/ft^2

sigma_5000ft = 0.8614; % Density ratio

for i =1:8

    W_S = [40 50 60 70 80 90 100 110];

for j = 1:4

    Cl_max_TO =  [1.6;1.8;1.93;2.2]; %Max. Coefficient of lift take-off

    TW_TO_5000ft(:,i,:) = ((37.5*(W_S(i)))./(sigma_5000ft.*Cl_max_TO.*S_TOFL));

end

end



figure(2);

ft1=plot(W_S*4.88243,TW_TO_5000ft(:,:,1),'LineWidth',1);

hold on

ft2=plot(W_S*4.88243,TW_TO_5000ft(:,:,2),'LineWidth',1);

ft3=plot(W_S*4.88243,TW_TO_5000ft(:,:,3),'LineWidth',1);

ft4=plot(W_S*4.88243,TW_TO_5000ft(:,:,4),'LineWidth',1);



%Land

Va = sqrt((LFD*3.28084)/0.3); %Approach speed in knots

Vsl = Va/1.3; %Landing stall speed in knots

rho_l = 0.002048; %Density at slug/cu.ft

for i =1:4

    Cl_max_L =  [1.6;2.0;2.4;2.6]; %Max. Coefficient of lift land

    W_S_Land = (0.5*rho_l*(Vsl*1.688)^2).*Cl_max_L;

    W_S_land = W_S_Land./0.95;

end
```

Climb sizing drag polar

```
W_S_assumed = 82.7; %Wing loading in lb/ft^2

S = (Wto*2.20462)/ W_S_assumed ; % Surface area in sq.ft

Swet = 3800; % Wetted surafce area in sq.ft

f = 9.3; % Skin friction coefficient

Cdo = f/S;

clmax_clean = 1.4; %assumed

clmax_to = 2.2; %assumed

clmax_l = 2.6; %assumed

AR = 8.7; %Aspect ratio assumed


% ostwald efficiency

e_clean = 0.85;

e_to = 0.8; %take-off gear up and down

e_l = 0.75; %Land gear up and down

e = [e_clean e_to e_l];

k = 1./(pi.*e.*AR);

% skin friction drag (increment from flap and gear)

d_cdo_to = 0.015; %flap

d_cdo_l = 0.06; %flap

d_cdo_gear = 0.017; %gear


% Skin friction drag from segments

cdo_clean = Cdo; %clean

cdo_to_gu = Cdo + d_cdo_to; %take-off flaps and gear up

cdo_to_gd = cdo_to_gu + d_cdo_gear; %take-off flaps and gear down

cdo_l_gu = Cdo + d_cdo_l; %landing flaps and gear up
```

```
cdo_l_gd = cdo_l_gu + d_cdo_gear; %landing flaps and gear down


% FAR 25.111 OEI initial segment

Cl_initial = clmax_to/1.44;

cd_initial = cdo_to_gu + k(2)* Cl_initial^2;

L_D_initial = Cl_initial/cd_initial;

T_W_i = 2*((1/L_D_initial)+0.012); %At 1.2 Vs_to

T_W_OEI = T_W_i/0.8; %corrected


% FAR 25.121 OEI transition at VLOF = 1.1 Vs_to

Cl_vlof = clmax_to/1.21;

cd_vlof = cdo_to_gd + k(2)* Cl_vlof^2;

L_D_vlof = Cl_vlof/cd_vlof;

T_W_vlof = 2*((1/L_D_vlof)); %At 1.2 Vs_to

T_W_1_1_vsto = T_W_vlof/0.8; %corrected

%at V2

cd_v2 = cdo_to_gd + k(2)* Cl_initial^2;

L_D_v2 = Cl_initial/cd_v2;

T_W_v2 = 2*((1/L_D_v2)); %At 1.2 Vs_to

T_W_1_1_vsto_v2 = T_W_v2/0.8; %corrected


% FAR 25.121 OEI second segment

T_W_s = 2*((1/L_D_initial)+0.024); %At 1.2 Vs_to

T_W_1_2_vsto_flap_down = T_W_s/0.8; %corrected


% FAR 25.121 enroute

clc = clmax_clean/(1.25*1.25);

cdc = cdo_clean + k(1)*clc^2;
```

```
L_D_c = clc/cdc;

T_W_c = 2*((1/L_D_c)+0.012);

T_W_clean = T_W_c/0.8;



% FAR 25.119 AEO

cl_l = clmax_l/ (1.3*1.3);

cd_l = cdo_l_gd + k(3)*cl_l^2;

L_D_l = cl_l/cd_l;

T_W_l = ((1/L_D_l)+0.032);

T_W_balkedlanding_AEO = (T_W_l*0.95)/0.8;



% FAR 25.121 OEI

clmax_a = 2.4;

cdo_a = 0.0709;

cl_bl = clmax_a / (1.5*1.5);

cd_bl = cdo_a + k(3)*cl_bl^2;

L_D_bl = cl_bl/cd_bl;

T_W_bl = 2*((1/L_D_bl)+0.021);

T_W_balkedlanding_OEI = (T_W_bl*0.95)/0.8;



%cruise speed sizing

dcdo = 0.0003;

q_bar = 156; %dynamic pressure 0.75 Mach

for i =1:8

    W_S = [40 50 60 70 80 90 100 110];

    %S_w = (Wto*2.20462)./W_S

    %f = 11.2;

    cdoc = Cdo +dcdo;
```

```
    T_W_cr = (cdoc*q_bar)./W_S  + W_S./(q_bar*pi*AR*e_clean);

    T_Wto = T_W_cr./0.25;

end
```

figure

```
figure(2);

ft1=plot(W_S*4.88243,TW_TO_5000ft(:,:,1),'LineWidth',1);

hold on

ft2=plot(W_S*4.88243,TW_TO_5000ft(:,:,2),'LineWidth',1);

ft3=plot(W_S*4.88243,TW_TO_5000ft(:,:,3),'LineWidth',1);

ft4=plot(W_S*4.88243,TW_TO_5000ft(:,:,4),'LineWidth',1);

fl1=line([W_S_land(1)*4.88243,W_S_land(1)*4.88243],[0,0.5],'color','g');

fl2=line([W_S_land(2)*4.88243,W_S_land(2)*4.88243],[0,0.5],'color','b');

fl3=line([W_S_land(3)*4.88243,W_S_land(3)*4.88243],[0,0.5],'color','r');

fl4=line([W_S_land(4)*4.88243,W_S_land(4)*4.88243],[0,0.5],'color','k');

ll3=line([0,550],[T_W_OEI,T_W_OEI]);

set([ll3(1)],'Linestyle','-.','color','y','LineWidth',1);

ll4=line([0,550],[T_W_1_1_vsto,T_W_1_1_vsto]);

set([ll4(1)],'Linestyle','-.','color','r','LineWidth',1);

ll5=line([0,550],[T_W_1_1_vsto_v2,T_W_1_1_vsto_v2]);

set([ll5(1)],'Linestyle','-.','color','k','LineWidth',1);

ll6=line([0,550],[T_W_1_2_vsto_flap_down,T_W_1_2_vsto_flap_down]);

set([ll6(1)],'Linestyle','-.','color','g','LineWidth',1);

ll7=line([0,550],[T_W_clean,T_W_clean]);

set([ll7(1)],'Linestyle','-.','color','c','LineWidth',1);

ll8=line([0,550],[T_W_balkedlanding_AEO,T_W_balkedlanding_AEO]);

set([ll8(1)],'Linestyle','-.','color','m','LineWidth',1);

ll9=line([0,550],[T_W_balkedlanding_OEI,T_W_balkedlanding_OEI]);
```

```
fs5 = fit((W_S*4.88243)',T_Wto','cubicinterp');

hl5 = plot(fs5,(W_S*4.88243)',T_Wto');

set([hl5(2)],'color','r');

dp =
plot(W_S_land(4)*4.88243,T_W_balkedlanding_OEI,'OR','MarkerEdgeColor','r','MarkerFa
ceColor',[0.2,0.2,0.3],'MarkerSize',5);

lgd = legend([ft1 ft2 ft3 ft4 fl1 fl2 fl3 fl4 ll3(1) ll4(1) ll5(1) ll6(1) ll7(1)
ll8(1) ll9(1) hl5(2) dp],'CLmax_{TO} = 1.6','CLmax_{TO} = 1.8','CLmax_{TO} =
1.93','CLmax_{TO} = 2.2','CLmax_{L} = 1.6','CLmax_{L} = 2.0','CLmax_{L} =
2.4','CLmax_{L} = 2.6','FAR 25.111(OEI)','FAR 25.121(OEI)-Transition at
V_{LOF}','FAR 25.121(OEI)-Transition at V_{2}','FAR 25.121(OEI)-Second
segment','FAR 25.121(OEI)-En-route','FAR 25.119(AEO)-Balked landing','FAR
25.121(OEI)-Balked landing','cruise speed','Design point');

title('Performance sizing (Matching graph)');

xlabel('\bf Wing loading (W/S)_{TO} (kg/m^2)');

ylabel('\bf Take-off Thrust-to-weight ratio (T/W)_{TO}');

xlim([0,550]);
```

Published with MATLAB® R2020a